Carnegie Mellon University
MELLON COLLEGE OF SCIENCE

THESIS

SUBMITTED IN PARTIAL FULFILLMENT OF THE REQUIREMENTS
FOR THE DEGREE OF

DOCTOR OF PHILOSOPHY IN THE FIELD OF PHYSICS

TITLE: "Capillary and transport phenomena of liquid drops spreading on miscible liquid subphases."

PRESENTED BY: Amy Stetten

ACCEPTED BY THE DEPARTMENT OF PHYSICS

Stephen Garoff	9/28/17
STEPHEN GAROFF, CO-CHAIR PROFESSOR	DATE
Todd Przybycien	9/25/17
TODD PRZYBYCIEN, CO-CHAIR PROFESSOR	DATE
Robert Tilton	9/25/17
ROBERT TILTON, CO-CHAIR PROFESSOR	DATE
Scott Dodelson	9/28/17
SCOTT DODELSON, DEPT HEAD	DATE

APPROVED BY THE COLLEGE COUNCIL

Rebecca Doerge	9/28/17
REBECCA DOERGE, DEAN	DATE

Capillary and transport phenomena of liquid drops spreading on miscible liquid subphases

by

Amy Zufall Stetten

Submitted in partial fulfillment of the
requirements for the degree of
Doctor of Philosophy
at
Carnegie Mellon University
Department of Physics
Pittsburgh, Pennsylvania

Advised by Professors
Stephen Garoff
Todd Przybycien
and Robert Tilton

September 22, 2017

"Bazingstoke, my dear."

– W. S. Gilbert

Abstract

It has long been known that drops of soluble surfactant solution induce Marangoni flows at air-liquid interfaces. These surfactant drops create a surface tension gradient, which causes an outward convective flow at the fluid interface. In this thesis, we show that aqueous phospholipid dispersions may be used for this same purpose. In aqueous dispersions, phospholipids aggregate into vesicles that are not surface-active, so these dispersions do not initiate Marangoni flow. However, aerosolization of these dispersions causes the vesicles to shear open, allowing access to the surface-active lipid monomer within. Deposition of lipid via aerosolization leads to surface tensions as low as 1 mN/m on water and can induce spreading on entangled polymer subphases even in the presence of pre-deposited phospholipid layers.

Most methods for introducing a surfactant solution to a liquid subphase involve dropwise deposition, either by pipette or by aerosol. In order to better understand the behavior of these miscible drop/subphase systems, we study drops of solvent as they slowly diffuse into their polymer solution subphase. Previous work has shown that, even when two fluids are completely miscible, they can maintain a detectable "effective interface" for long times. Effective interfacial tension has been probed using a number of methods, but that work has not extended to the three-phase system of a fluid drop on top of a miscible pool. By observing drop shapes, we show that these drops obey immiscible wetting conditions, that their shapes obey the augmented Young-Laplace equation, and that the low density difference of these systems provides a unique ability to probe very small pressures across the drops.

The ability to use phospholipids naturally found in the lung as spreading agents on low surface tension surfaces of macromolecular solutions, in tandem with an understanding of the effective interfaces controlling drop shape, yields a deeper understanding of how we might improve surfactant-driven delivery of therapeutic agents along the complex airway surfaces in the lung.

Acknowledgments

The work in this thesis was supported in part by the National Science Foundation under grants CBET-1510293 and 1264552 and in part by the National Heart, Lung and Blood Institute of the National Institutes of Health under grant R01 HL105470. The content is solely the responsibility of the authors and does not necessarily represent the official views of the National Science Foundation or the National Institutes of Health.

For assistance conducting experiments, I would like to thank Dr. John Riley and Emily Wallitsch for their ellipsometry expertise, Joseph Nero for his aid in aerosol sizing, and visiting undergraduate students Kassidy Meck (Barnard College, NYC) and Telda Wang (University of Science and Technology of China) for drop-shape photography.

Over the past 6 years, I have had the honor of being part of a large, lively, collaborative group. First, I would like to thank my advising trio. Thank you for your hours, your dedication, and your encouragement. Steve, I know I can be obstinate. Thank you for not only being willing to bend, but for actively working to change the dynamic and be an advocate in the lab and in the department. Todd, no matter what the critique, you always know how to deliver it with kindness and clarity. Thank you for being more sure of my success than I was. Bob, your thoroughness and depth of understanding of the literature are an inspiration. Thank you for your tireless, calm support. I would also like to thank my honorary fourth advisor, Tim Corcoran. Your kindness and your subtle, straight-faced humor always make me smile. Thank your for your support, and for advising me that I have the ability to study and understand my own illness; I had been too scared to before we met. The four of you taught me the incredible power of collaborative research – of bringing together different minds with different perspectives to solve problems synergistically (that word's for you, Bob). I hope that the next time one of your students finds a contaminated sample, you'll allow me to join you at Church Brew Works.

Next, I would like to thank the two other members of my committee. Dr. T-Nagle, thank you for your crucial collaboration, for your support of women in science, and for your intense

and enthusiastic dedication to the work. Mathias, you don't let me get away with anything, and it makes me a better scientist. Thank you for pushing me to be my best. Also, thank you to Markus for always having time for my questions, to Manfred for helping me grow within the department, to Diane for always including me in your exciting adventures, and to Hael for getting me addicted to fountain pens (my wallet doesn't thank you).

Finally, I would like to thank the incredible group of colleagues, friends, and family who have supported me throughout my time here at CMU and beyond. Grandma and Grandpa, thank you for being forces of nature and teaching me that people can do amazing things. Dad, thanks for the playroom filled with pliers and oscillascopes and for never once doubting that I could be a scientist. Mom, you always know just what to say. Thanks for helping me learn how to see situations from all sides and to attack even the most difficult situations with deep thought and kindness. Wendy, you work so hard and you are so amazing. You make me want to be a better person. Winslow, thank you for sitting through more tearful rants than you deserved. You kept me sane and healthy. I'm sorry that thesis writing broke our NYT crossword puzzle streak. Jaymie, thanks for being the best bestie a girl could hope for. Sometimes I forget how amazing your positivity makes me feel, and then you remind me. Anthony, thanks for the trips to Deep Creek to sail and swim and clear my head. Brad Treece, thanks for being a constant friend, moral support, and math genius. Here's to many more years of crafting plans and sometimes following through with them. Steve Iasella, thanks for asking me to explain my experiment on your first day in lab, rather than asking me when I'd be done with the equipment. You helped me re-learn that lab friendships can be wonderful. Bhagyashree, Larisa, Krista, Ellen, Tabitha, and Maddy, thank you for the teatime talks, lulus laughs, and coffee (coffee coffee with extra sugar!) rants. And thank you to all the members of physics and chemical engineering community for being so lovely, welcoming, and supportive.

Contents

1 Introduction **2**

1.1 Medical motivation . . . 3
1.2 Marangoni transport and capillary statics . . . 5
1.3 Marangoni transport using phospholipids . . . 6
1.4 Behavior of liquid drops delivered to a miscible liquid subphase . . . 7

2 Enabling Marangoni Transport through Aerosolization of Lipid Dispersions **9**

2.1 Introduction to Lipid Transport . . . 11
2.1.1 Background on Marangoni transport using phospholipid dispersions . . . 11
2.1.2 Background on Marangoni transport for drug delivery in the lung . . . 14
2.1.3 Summary of our results . . . 16
2.2 Experimental Materials and Methods . . . 19
2.2.1 Materials . . . 19
2.2.2 Methods . . . 22
2.3 Lipid Isotherms . . . 35
2.3.1 Isotherms for DMPC on water, PA, and PGM . . . 35
2.3.2 Isotherms for DPPC on water and PGM . . . 37
2.4 Deposition of Microliter Drops of Lipid Dispersion . . . 41
2.5 Deposition of Aerosolized Lipid Dispersions . . . 43
2.5.1 DMPC transport on water . . . 43
2.5.2 Phospholipid transport in other systems . . . 45
2.5.3 Inversion of bead and pin placement . . . 51
2.5.4 Transport with multiple tracer particles . . . 53
2.6 Structure and Dynamics of the Surface Lipid Layer . . . 54
2.6.1 Ellipsometry showing lipid monolayer deposition . . . 54
2.6.2 Subsurface transport . . . 56
2.6.3 Model for how lipid aerosolization enables Marangoni transport . . . 58
2.7 Observations of Ultra Low Surface Tensions . . . 61
2.7.1 Low surface tension results from DMPC and DPPC . . . 61
2.7.2 Low surface tension results from other, soluble surfactants . . . 64
2.8 Phospholipid-induced transport of drugs on lung-mimic surfaces . . . 68

2.8.1 Transport of tobramycin with and without a pre-deposited lipid layer 68
2.8.2 Detection of transported tobyramycin 71
2.8.3 Surface tension recovery 74
2.8.4 Effect of isotherm shape on transport lag time 75
2.9 Transport using Natural Lung Surfactant 76
2.9.1 Microliter drop deposition 76
2.9.2 Aerosol deposition 78
2.10 Conclusions 80

3 Evolution and Disappearance of Solvent Drops on Miscible Polymer Subphases 83
3.1 Introduction 84
3.2 Experimental Materials and Methods 88
3.2.1 Materials 88
3.2.2 Methods 89
3.3 Observed Drop Shape Evolution 97
3.3.1 Interface shape recovery 98
3.3.2 Wetting condition 99
3.4 Pressures Governing Drop Shape 103
3.5 Fourier Analysis to Examine Drop Curvature 107
3.5.1 Determining a drop outline 107
3.5.2 Interpolating the drop outline using Fourier analysis 108
3.5.3 Calculating the mean curvature along the drop surface 112
3.6 Numerical Solutions to the Augmented Young-Laplace Equation 118
3.7 Analysis of Drop Curvature and Pressures 130
3.8 Drop Spreading and Dissolution 133
3.8.1 Power law growth of drop diameter 133
3.8.2 Relationship between disappearance and interfacial tension 134
3.9 Conclusions 140

4 Conclusions 141
4.1 Future Work 144
4.1.1 Phospholipid-induced Marangoni transport 144
4.1.2 Miscible drop shape evolution 147

A Further examples of spreading experiments 150
A.1 Spreading of indicator beads versus talc 151
A.2 Subsurface transport on PA solution 154

B Further drop shape examples 156
B.1 Time series of drop shape evolution 157

C Mathematical and Computational Methods **160**
C.1 Calculating the Sum of the Principal Curvatures of a Drop 161
C.2 Necessity of additional pressure for closing of drops 163
C.3 Role of the z^3 term in drop shape 165

List of Tables

2.1 Average dose, deposition time, and volumetric deposition flux in aerosol deposition experiments. Standard error is given in the table (n = 3). 72

3.1 Densities of various concentrations of 5MMW aqueous poly(acrylamide) solution and aqueous fluorescein solution. Standard deviations were less than 50 μg/mL over 10 trials. 96

3.2 Residuals for three cases. 1) residual distances between three independent hand-drawn outlines of a water drop placed on 1.0% PA (a round drop), 2) residual distances between three independent hand-drawn outlines of a water drop placed on 0.4% PA (a flat drop), and 3) residual distances between round and flat drop outlines and their respective inversions about the horizontal midline. This data corresponds to the outlines shown in Figure 3.8. 109

3.3 This table shows the polynomial pressure expansion fitting parameters for $\kappa(z)$ from our Fourier curvature calculation to a 6th order polynomial in z. The three "outline" columns show fits to three separate outlines of the same flat or round drop. The data in these columns represents the raw fit parameter multiplied by z^O where z is the height of the drop (0.1 and 0.25 mm respectively) and O is the order of the term in the polynomial. Multiplying by this z^O allows us to examine the approximate magnitude of the full n^{th} order term rather than simply the coefficient. The quadratic and quartic fitting parameters are shown in bold. Outline 3 for the thin drop was fit only to 4th order because the 6th order fit severely overfit the data, resulting in residuals that were larger than the data itself. 116

3.4 This table shows power law growth coefficients and R^2 values for the drop trials shown in Figure 3.21. Power law fits were of the form Diameter = At^B. The data shown here is for five individual trials taken from the top. The difference in the value of the power for two trials on the same subphase is approximately the same as the difference between subphases. 135

List of Figures

1.1 Schematic of aerosol deposition in the airways of the lung. Arrows show air flow in from the trachea and towards outer airway branches. Aerosol particles are likely to follow the higher airflow through clearer airways and avoid obstructions such as mucus plaques. 4

2.1 Molecular structure of dimyristoylphosphotidylcholine (DMPC). Image from product manufacturer, Avanti Polar Lipids. 19
2.2 Molecular structure of dipalmitoylphosphotidylcholine (DPPC). Image from product manufacturer, Avanti Polar Lipids. Note the only difference between this and the structure of DMPC is the longer carbon tail. 19
2.3 Molecular structure of poly(acrylamide) (PA). Image from Wikipedia. 21
2.4 Molecular structure of tobramycin. Image from PubChem. 23
2.5 Size distribution of aerosols from AeroNeb Solo micropump nebulizer. 10 mg/mL DPPC (circles), 60 mg/mL tobramycin (squares), 10 mg/mL DPPC and 60 mg/mL tobramycin (triangles). Errors on all points are 0.1 μm (n = 3). For aerosols containing tobramycin at a concentration of 60 mg/mL, the volume-weighted median droplet diameter was 5.0 μm, with volume-weighted 10th and 90th percentile values of 2.0 μm and 10.7 $\pm$ 0.2 μm. The volume-weighted median droplet diameter for a tobramycin and DPPC dispersion was 5.3 μm (with volume-weighted 10th and 90th percentile values of 2.2 μm and 11.7 μm). The volume-weighted median droplet diameter for a DPPC dispersion was 5.5 $\pm$ 0.2 μm (with volume-weighted 10th and 90th percentile values of 2.1 μm and 14.2 $\pm$ 1.3 μm). 24
2.6 Diagram of trough setup. Dimensions of the trough are 20 cm long by 2 cm wide by 2 cm deep. The aerosol deposition is perpendicular to the long axis of the trough at a declination of approximately 45°. 26
2.7 Diagram of trough setup. Dimensions of the trough are 20 cm long by 2 cm wide by 2 cm deep. The aerosol deposition is perpendicular to the long axis of the trough at a declination of approximately 45°. This setup differs from the previous version in Figure 2.6 in that it contains a bias flow and is enclosed in a glove box. This means that tobramycin transport data was taken independently (via the array of pipettes) from surface tension data (taken with the trough outside the glove box). 29

2.8 Cumulative liquid mass delivered by the nebulizer and lipid concentration in the DMPC aerosol taken simultaneously (data for two trials plotted). Error bars on experimental mass measurement are ± 0.0001 g, which is within plotted points. These are measurements made over two minute intervals, which average over unsteady output of the nebulizer. The lines are guides to the eye. 32
2.9 Surface pressure versus area for DMPC on water. Data are shown for three separate trials. For each trial, surface pressures were calculated using the reference surface tension of the clean interface before deposition. 36
2.10 Surface pressure versus area for DMPC on 1% 5 MDa PA solution. Data are shown for three separate trials. For each trial, surface pressures were calculated using the reference surface tension of the clean interface before deposition. 37
2.11 Surface pressure versus area for DMPC on 5% PGM solution. Data are shown for two separate trials. For each trial, surface pressures were calculated using the reference surface tension of the clean interface before deposition. 38
2.12 Surface pressure vs area for DPPC on water (black circles) and on a 5 wt% PGM solution (gray squares). Surface pressures were calculated using the surface tension of 72 mN/m for water and the surface tension of 40 mN/m for the mucin solution as reference surface tensions. Each of these sets of data is an individual trial. 39
2.13 Surface tension vs area for DPPC on water (black circles) and on a 5 wt% PGM solution (gray squares). At low area per DPPC molecule the surface tension for both subphases converges to $\sim$ 29 mN/m. Note that these data are from the same trials as that in Figure 2.12. 40
2.14 Simultaneous measurements of surface tension and indicator bead position for dropwise lipid dispersion deposition. Deposition of microliter drops of 10 mg/mL DMPC dispersion onto a DI water subphase. Ten μL droplets of 10 mg/mL DMPC was deposited every 10 seconds for the duration of the experiment. 41
2.15 A representative plot of surface tension and position versus time during aerosolized DMPC dispersion deposition. In this trial, 4 mL of 10 mg/mL DMPC dispersion were aerosolized via an AeroNeb Solo vibrating mesh nebulizer onto a clean DI water surface. Aerosol deposition begins at 0 seconds and ends at 450 seconds. The Wilhelmy pin is located at approximately 9 cm. 43
2.16 10mg/mL DMPC dispersion aerosolized via AeroNeb vibrating mesh nebulizer to a PA subphase. The point at which the nebulizer turned off is marked "off". 46
2.17 10mg/mL DMPC dispersion aerosolized via AeroNeb vibrating mesh nebulizer to a 5% PGM subphase. The point at which the nebulizer turned off is marked "off". 47
2.18 10mg/mL DMPC dispersion aerosolized via jet nebulizer to a DI water subphase. 47
2.19 10mg/mL DMPC dispersion aerosolized via jet nebulizer to a PA subphase. 48

2.20 10mg/mL DMPC dispersion aerosolized via jet nebulizer to a 5% PGM subphase. 48

2.21 4 mL of 1 mg/mL DMPC dispersion aerosolized via an AeroNeb Solo vibrating mesh nebulizer onto a clean DI water surface. Note that the decrease in surface tension begins to decrease at around 1000 s, where as the decrease began at around 200 s for the 10 mg/mL dispersion. 49

2.22 10mg/mL DPPC dispersion aerosolized via jet nebulizer to a DI water subphase. 50

2.23 10mg/mL DPPC dispersion aerosolized via jet nebulizer to a 5% PGM subphase. 50

2.24 10mg/mL DMPC dispersion aerosolized via AeroNeb vibrating mesh nebulizer onto a DI water subphase. In this experiment, the Wilhelmy pin and polystyrene indicator bead are inverted with the pin just outside the mouth of the deposition box and the bead just past the pin. 51

2.25 10mg/mL DMPC dispersion aerosolized via AeroNeb vibrating mesh nebulizer onto a water subphase. In this experiment, two beads were placed on the surface. The closer bead to the nebulizer starts moving first (dark gray) and then picks up the second (light gray) as they move across the trough together. 53

2.26 Ellipsometric parameters of A) a monolayer deposited out of chloroform (units of molecules per area) shown as filled circles, and B) a surface layer deposited via aerosolization (units of minutes) shown as open squares. The dashed line marks the saturation of the chloroform-deposited monolayer. 55

2.27 Dark field microscopy images of lipid clusters beneath the surface in the area of aerosol deposition. All panels are 430 by 343 μm. A is focused on small chromium dioxide needles that were placed on the water surface in order to be able to focus at the air-liquid interface. B is focused $\sim$ 60 μm beneath the surface. The small ($\sim$ 10 μm), sharply focused bright spots are clusters of lipid. The arrow in panel B points to one such small cluster. The larger, less focused features are the out-of-focus chromium dioxide needles on the surface or other out-of-focus lipid clusters. C is focused $\sim$ 420 μm below the surface and shows very few lipid clusters have been transported this deep into the subphase. 56

2.28 Dark field microscopy images of lipid cluster transport outside of the area of deposition. All panels are 430 by 343 μm and focused $\sim$ 60 μm beneath the surface. A shows out-of-focus chromium dioxide needles before the nebulizer is turned on. B occurs during deposition and shows lipid clusters (as well as chromium dioxide needles) moving across the field of view beneath the surface at $\sim$ 0.05 cm/s. By 7 min: 20 sec, shown in C, subsurface lipid clusters are still evident, but lateral flow has ceased. 57

2.29 Schematic of aerosol delivery. Nebulization disrupts vesicles and stores monomeric lipid as an adsorbed layer on droplets. These droplets deliver monomeric lipid to the subphase surface and re-aggregated lipid to the subphase bulk. The lipid monomer on the subphase surface induces Marangoni transport. 60

2.30 Representative low surface tension results for 10 mg/mL DPPC and DMPC MLV dispersions aerosolized via AeroNeb vibrating mesh nebulizer onto DI water. Both lipids are able to reach very low surface tensions (< 10 mN/m). In these trials, the vibrating mesh nebulizer was turned on at 60 seconds and turned off at the label "off". The DPPC monolayer is relatively stable after the nebulizer is turned off, while the DMPC monolayer destabilizes and the surface tension increases to ~ 20 mN/m. 61

2.31 Representative low surface tension result for 10 mg/mL DPPC MLV dispersion aerosolized via jet nebulizer onto DI water. The subphase reaches very low surface tensions (< 10 mN/m). In these trials, the jet nebulizer was turned on at 60 seconds and turned off at the slight blip at ~ 2800 s. The DPPC monolayer is relatively stable after the nebulizer is turned off, remaining below 10 mN/m overnight. 62

2.32 Example trial showing surface tensions for 4 mg/mL tyloxapol deposited onto water dropwise (black) and via vibrating mesh nebulizer (gray). The black data shows the surface tension as 1μL per minute of tyloxapol solution is deposited for 20 minutes. The gray data shows the surface tension as the tyloxapol solution is aerosolized onto the surface. Deposition begins at 60 seconds and the nebulizer runs out around 620 seconds. The gray dashed line represents the surface tension of the 4 mg/mL tyloxapol solution, 37 mN/m. 65

2.33 Example trial showing surface tensions for 5 mM CTAB aerosolized onto DI water via vibrating mesh nebulizer. Aerosolization begins at 60 seconds and the nebulizer runs out at 1000 seconds. The gray dashed line represents the surface tension of the 5 mM CTAB solution, 32 mN/m. This result was repeated three times. 66

2.34 Surface tension and movement of a tracer bead during representative DPPC spreading experiments, (A) without pre-deposited lipid on PGM solution, (B) with pre-deposited lipid on PGM solution, and (C) without pre-deposited lipid on water. The grey line is the surface tension and the black line is the bead position with 0 cm being at the edge of the aerosolization chamber. Nebulization begins at zero seconds. In (A) the abrupt surface tension dip at about 500 s is a reproducible but as yet unexplained phenomenon. Negative times in (B) represent times before aerosolization begins, when the DPPC is being deposited onto the subphase. 70

2.35 The tobramycin concentration on the subphase surface in the region outside the aerosolization chamber determined after complete nebulization of the contents of the reservoir. When no DPPC is present in the aerosol (black circles), no tobramycin escapes the aerosolization chamber. When DPPC is added to the aerosol, spreading occurs and tobramycin can be detected all the way across the trough (light gray squares). Spreading is similar when a DPPC monolayer is deposited on the subphase prior to delivery of the DPPC/tobramycin aerosol (dark gray diamonds). The error bars show the standard error of three trials (n = 3). The concentration is normalized by the total deposited dose for a given run. A scaled concentration of 1 corresponds to a tobramycin concentration of approximately 7 μg/mL, though it varies slightly for each trial. Average scaled tobramycin concentrations sampled inside the region of deposition were $\pm$ 5 for all trials. 73

2.36 Aerosolization (black) and dropwise deposition (gray) of Infasurf onto a 5% PGM subphase at 25°C. The nebulizer is turned on at 25 seconds and runs out at 320 seconds. The first 2 μL drop is placed at 25 s and then three more 2 μL drops were placed, each one minute apart. 77

3.1 Still images from side-view experiments. A 2μL droplet of water was placed atop a 1% or 0.4% 5 MDa PA solution and a wetting layer of PA can be seen to come over top of the drop. The drop gradually changes shape with time as the EIT between the miscible phases decreases. On the higher concentration subphase, the water drops remain rounder and disappear more slowly, giving evidence for a higher EIT. 90

3.2 Still images from side-view experiments with deposition from beneath the interface. A droplet of water was deposited beneath the surface of a 1% 5 MDa PA solution using a curved syringe. The volume in this method was inexact. The drop rises, but maintains a thin wetting layer of PA between it at the air interface. The drop gradually changes shape with time as the EIT between the miscible phases decreases. 91

3.3 Still images from top-view experiments. A 2μL droplet of water is placed atop a 1% 5 MDa PA solution and is visualized using our Ronchi ruling technique. 93

3.4 Measured kinematic viscosities for aqueous poly(acrylamide) of two different molecular weights at multiple concentrations. 5 MDa PA is shown in circles (black for one trial, gray for a second). 1 MDa PA is shown in squares (black for one trial, gray for a second). The connecting curves are guides for the eye. 96

3.5 Film thickness (measured from the center top of the drop to the closest point in the dark meniscus band) plotted versus time for two drops at different concentrations. Black circles show data for water atop a 1% 5 MDa PA solution subphase, gray squares show data for water atop a 0.4% 5 MDa PA solution subphase. Error bars represent the standard deviation on the mean for three measurements at each point. 98

3.6 Confocal microscopy images of a phase separated 1:1 mixture of butanol and D_2O. The plot shows the roughness of the surface of the butanol poor subphase with butanol rich drops atop it. The drops are measured to have a very low contact angle of $3.0 \pm 0.5°$. Data taken by collaborator Franziska Henrich at the Max Planck Institute for Polymer Physics in Mainz, Germany. 101

3.7 Confocal microscopy images of a water drop atop a PA subphase. The plot shows the roughness of the surface. No contact line is detected. Data taken by collaborator Franziska Henrich at the Max Planck Institute for Polymer Physics in Mainz, Germany. 102

3.8 A1 and B1 show a sample flat and a sample round drop flipped about their horizontal axes (about our $z = 0$ line). The flat drop is on a 0.4% 5 MDa subphase at 150 s and the round drop is on a 1.0% 5 MDa subphase at 38 s. They are the same drops seen in Figure 3.1 and will continue to be used as examples throughout this chapter. Residual distances between the top of the drop and the flipped lower half are typically less than or equal to 0.01 mm. A2 and B2 show the same flat and round drops outlined three independent times by eye. Residual distances between these three outlines are typically on the order of 0.01 mm. 108

3.9 Drop outline and curvature attained via our Fourier method for a single drop calculated with three different numbers of Fourier modes. The top panel shows 14 modes, which underfits the drop (as can be seen by the drop outline not matching the drop well). The middle shows 22 modes, which is our calculated ideal based on residuals to the drop. The bottom shows 30 modes, which overfits the drop (as can be seen by ringing in the curvature). 111

3.10 Residual distances between the raw drop outline and the optimized Fourier interpolation for two drops. A shows residuals for a round drop (on 1% PA at 38 s) and B shows the residuals for a flat drop (on 0.4% PA at 150 s). Note that the axes have different y maxima. 112

3.11 Curvature attained via our Fourier method (in gray) and a 4th order polynomial fit to the curvature versus z (in dashed black) for two drops with different shapes (a rounder drop shape in the top panel: A and B, and a flatter drop shape in the lower panel: C and D). The curvature is plotted versus arclength on the left (A and C) and versus z on the right (B and D). In the curvatures plotted versus z (B and D), the two gray curves represent the two ends of the drop; the black dashed curve is the fit, which averages over the two ends. . 114

3.12 Schematic of coordinate system used in anaysis. 118

3.13 Numerical drop fits. A) shows a round, early time (38 s) water drop in 1.0% 5 MDa PA. B) shows a flat, late time (150 s) water drop in 0.4% 5 MDa PA. The original drop outlines are in solid black. The numerical solutions are overlaid in dashed gray. 122

3.14 Residuals to numerical drop fits. A) shows residuals for the round, early time water drop in 1.0% 5 MDa PA shown in Figure 3.13A. B) shows residuals for the flat, late time water drop in 0.4% 5 MDa PA shown in Figure 3.13B. The dashed gray lines show the $z = 0$ endpoint of the drops. The mean residual distance between the drops and their outlines is ~ 0.005 mm. 123

3.15 Numerical drop fits for a 2μL drop of water placed atop 0.4% 5 MDa PA traced over the course of 150 seconds. True drop outline in black, numeric fit in dashed gray. 125

3.16 Numerical drop fit curvatures for a 2μL drop of water placed atop 0.4% 5 MDa PA traced over the course of 150 seconds. 126

3.17 Numerical drop fits for a 2μL drop of water placed atop 1.0% 5 MDa PA traced over the course of 300 seconds. True drop outline in black, numeric fit in dashed gray. 127

3.18 Numerical drop fit curvatures for a 2μL drop of water placed atop 1.0% 5 MDa PA traced over the course of 300 seconds. 128

3.19 Curvature calculated from the Fourier representation (in solid black) and from the numerical AYLE solution (in dashed gray) plotted versus arc length (left) and versus height (right). The top panel shows results for a round drop (water on 1% PA at 38 seconds) and the bottom panel shows results for a flat drop (water on 0.4% PA at 150 seconds). 129

3.20 Schematic diagram of pressure components acting on buoyant, wetted drops. The air-liquid interface is located at the top of each plot. The dotted lines show the buoyancy pressure, which goes linearly with height. The dashed lines show an illustrative functional form for $P(z)$ (a decreasing exponential in z), which is largest near the interface and then decreases to zero far away. The solid black line shows the sum of these two pressures, which, but for scaling factors, is the curvature of the drop. Panel A shows the case of a highly symmetric drop spanning a highly symmetric piece of the curvature. Panel B is zoomed out to show both the highly symmetric drop and a highly asymmetric drop that spans a greater height and, therefore, a more asymmetric portion of the curvature. Note that the pressures have been shifted slightly along the vertical axis to allow for better visualization. This does not affect the form of the resulting curvature. 131

3.21 Diameter versus time for a 2μL water drop atop multiple concentrations of 5 MDa aqueous poly(acrylamide) solution subphases. The data shown here are for five individual trials taken in the top view setup. The same power law trend is seen when taking diameter data in the side view setup. 133

3.22 Diameter versus time for a 2μL water drop atop 1% 5 MDa aqueous poly(acrylamide) solution from the side and from the top. Two different trials are shown from our top-view setup (gray and unfilled squares) to show variation trial to trial. The third set of data shown is the same system viewed from the side (black circles) to show that side and top view setups give similar results. Exponents for the power law fits are 0.20, 0.26 for the two top-view trials and 0.19 for the side-view trial. 134
3.23 Disappearance time versus concentration squared for 2 μL water drops in 5 MDa aqueous poly(acrylamide) solution. The line is a linear fit to the data, which reveals the quadratic behavior of concentration with disappearance time. 137
3.24 Disappearance time versus concentration for 2 μL water drops in 5 MDa (black circles) and 1 MDa (gray squares) aqueous poly(acrylamide) solution. The lines are quadratic fits to the data, which reveal the quadratic behavior of concentration with disappearance time. 138
3.25 Disappearance time versus viscosity for 5 MDa (black circles) and 1 MDa (gray squares) aqueous poly(acrylamide) solution. 139

A.1 Stills taken from spreading experiments with polystyrene particles and talc powder on the same 75% glycerine in water subphase. Talc forms a ring on the lower half of the dish (the "smile") and polystyrene beads are placed on the upper half (the "eyes") A 2 μL drop of 5 mg/mL tyloxapol was placed at 0 seconds. Times are marked as minutes:seconds on the images. The dish measures 7 cm in radius. 152
A.2 Radius versus time for spreading experiments with polystyrene particles (gray squares) and talc powder (black circles) on the same 75% glycerine in water subphase. A 2 μL drop of 5 mg/mL tyloxapol was placed at 0 seconds. The dish measures 7 cm in radius. This data is from the experiment shown in Figure A.1. 153
A.3 Stills from subsurface transport microscopy images of 10 mg/mL DMPC dispersion aerosolized via vibrating mesh nebulizer onto a 1% 5 MDa PA solution subphase. A shows pure PA, which contains small particulates. This particulate matter is homogeneous and independent of depth. B and C show PA during deposition of aerosolized DMPC dispersion. B is focused $\sim$ 40 μm below the air-liquid interface, which is in the middle of the layer containing lipid clusters. C is focused $\sim$ 100 μm beneath the air-liquid interface, which is just beneath the layer containing lipid clusters. Lipid clusters can be seen out of focus, while PA particulates are in focus and approximately the same density as in the pure PA. 155

B.1 Stills from side-view trials of a 2 μL drop of water placed on 1.0% 5 MDa PA. Times are shown on each image in the format minute:second. Each frame is 1.8 mm tall by 4.5 mm wide. 158

B.2 Stills from side-view trials of a 2 μL drop of water placed on 0.4% 5 MDa PA. Times are shown on each image in the format minute:second. Each frame is 1.8 mm tall by 4.5 mm wide. 159

C.1 A) In dashed gray, we show the spherical drop shape in the absence of external pressures. In black, we show a numerically solved drop shape with only buoyancy pressure, $R_0^2/a^2 = 0.1$. B) The value of the radial coordinate of the solution at the top of the drop, $\psi = \pi$, is plotted as a function of the Bond number, R_0^2/a^2. Only at zero gravity does the drop close at the top where the tangent to the curve becomes horizontal. 163

C.2 Drop shapes are shown for a curvature profile that is quadratic in z (center) and for curvature profiles containing the same quadratic term plus additional cubic terms (top and bottom). The solution bulges upward with the addition of positive cubic terms (top) and downward with the addition of negative cubic terms (bottom). 166

Nomenclature

CF – Cystic Fibrosis
ASL – Airway Surface Liquid
EIT – Effective Interfacial Tension
AYLE – Augmented Young-Laplace Equation
IRDS – Infant Respiratory Distress Syndrome
SRT – Surfactant Replacement Therapy
DPPC – dipalmitoylphosphotidylcholine
DMPC – dimyristoylphosphotidylcholine
MLV – Multilamellar Vesicle
SUV – Small Unilamellar Vesicle
PA – aqueous poly(acrylamide) solution
PGM – aqueous porcine gastric mucin solution
TM – Bilayer Melting Temperature
ρ – Density
g – gravitational acceleration
H – Subphase depth
S – Spreading Coefficient
γ – Interfacial Tension
μ – Dynamic Viscosity
D – Drop
B – Bulk
A – Air
κ – Twice the mean curvature
P_L – Laplace Pressure
$P(z)$ – Additional pressure from the air-liquid interface
δ – Breadth of diffuse interface
ϕ – concentration

Chapter 1

Introduction

This thesis explores a number of experimental topics related to the delivery of small aqueous droplets to miscible, complex polymer subphases. The work is divided into two primary categories. First, we will explore the use of phospholipid surfactants as initiators of surface-tension driven flows when delivered as an aerosol mist to an aqueous interface. Second, we will examine the wetting and shape evolution of water drops without surfactant delivered to a similar aqueous interface. We believe that this work has broad relevance and applicability in the fields of drug delivery and non-equilibrium capillarity.

1.1 Medical motivation

Cystic Fibrosis (CF) is a genetically inherited, autosomal recessive disease that affects 70,000 patients worldwide, with more than 1,000 cases being reported each year (according to the Cystic Fibrosis Foundation, 2017). CF affects the airway surface liquid (ASL) of the lung. The ASL is composed of two layers: a watery pericilary liquid (PCL), which resides close to the lung epithelial cells and contains active cilia, and a viscoelastic mucus layer residing atop the PCL, which is composed of 95% water, 2% glycoprotiens, 1% lipids and 1% inorganic salts [7, 94]. In CF, airway mucus becomes dehydrated and viscous and, as a result, cannot be cleared effectively [45]. Accumulated mucus becomes a harbor for bacterial infection and mucus plaques that may limit local ventilation [12, 29]. Despite prevalent use of inhaled antibiotics, the leading cause of mortality in CF is bacterial infection. [29]. With current inhaled therapies, drug distribution is determined entirely by aerodynamics. Inhaled aerosols follow the airflow – the path of least resistance – through the airways (see Figure 1.1). Additionally, the larger aerosol particles may impact in the upper airways because the air flows are not strong enough to overcome particle inertia. This leads to increased deposition in more proximal airways the lung and at airway branch points, often leaving the most severely obstructed and infected regions of the lung untreated. With these infected areas

not receiving adequate treatment, the bacterial infections may sustain and possibly become antibiotic resistant.

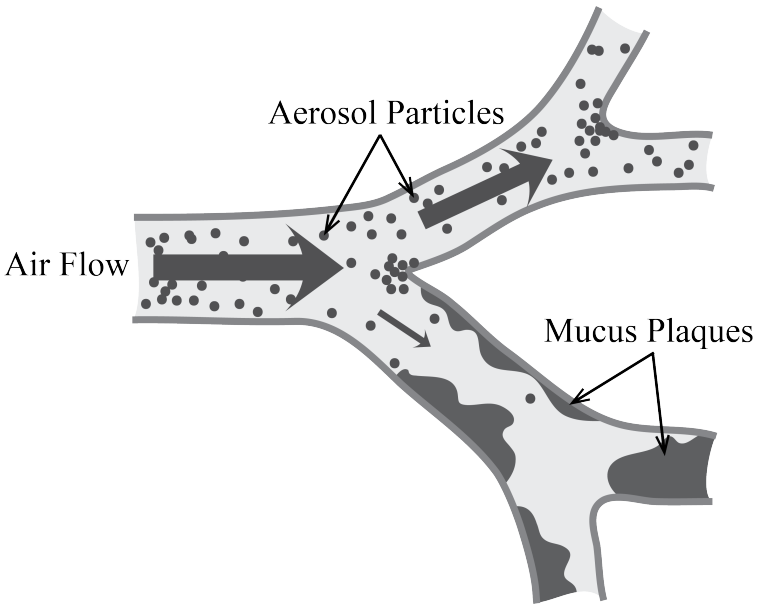

Figure 1.1: Schematic of aerosol deposition in the airways of the lung. Arrows show air flow in from the trachea and towards outer airway branches. Aerosol particles are likely to follow the higher airflow through clearer airways and avoid obstructions such as mucus plaques.

The collaborative "Lung Group" at Carnegie Mellon University and the University of Pittsburgh (lead by professors Garoff, Tilton, Przybycien, and Corcoran) has been working to develop alternate and enhanced methods of transporting medication deep into the lung to treat these bacterial infections. The work presented in this thesis outlines the development of self-dispersing aerosol formulations to drive drug away from regions of high aerosol deposition towards regions that are insufficiently dosed by that deposition. The spreading agents used are already native to the lung and likely safe for use in human patients. This work also studies the fundamental forces governing these spreading agents and their delivery. Ultimately, we hope that this work will aid in treatment of pernicious lung infections.

1.2 Marangoni transport and capillary statics

In order to induce transport of medications deep into the lung, the collaborative Lung Group proposes to use surface-tension-lowering agents such as surfactants to cause surface gradient flows (Marangoni flows), which will carry medication along the lung airway interface. In this way, induced Marangoni flow has the potential to improve drug delivery in patients with conditions that limit or alter aerosol delivery in the lung (for examples, see references [9, 39, 44]).

Marangoni flows most commonly occur when localized deposition of a surfactant causes a surface tension gradient (for examples, see references [1, 33, 34, 40, 56, 78]). This gradient induces a convective surface flow outward from the region of deposition. Delivery of surfactant-containing aerosols to the ASL would locally lower the ASL surface tension and generate flows along the surface and within the ASL that could transport medication over the mucus plaques to reach infection sites deeper in the lung.

Previous work from our group has shown that a variety of surfactants cause surface tension gradients and Marangoni flow when delivered to air-liquid interfaces, as long as the surface tension of the solution is lower than that of the subphase. Various soluble surfactants have been shown to be good spreaders on various model subphases [58, 65, 97, 99, 100]. Depending on the aerosol delivery fluxes, they may move laterally as individual droplets (low flux) or as a coalesced mass of aerosol droplets (high flux).

In general, surfactants are added to an aqueous interface in the form of drops of aqueous solution (either by pipette or by aerosol.) When small drops of a liquid are delivered to a liquid subphase, the way in which their shapes behave (and whether they will spread) will depend not only on their respective surface tensions with air, but also on their mutual, liquid-liquid interfacial tension. Traditionally, when one measures interfacial tension between fluids, these fluids are immiscible. However, even in the case of two miscible fluids, such as

aqueous drops on an aqueous subphase, the two fluids will maintain a detectible interface for some time. This interface will evolve as the two miscible fluids diffuse. This phenomenon is described in the literature as an "effective interface" with an "effective interfacial tension (EIT)" (first proposed in [67], with many references since). The full shape of the drop will be represented by the augmented Young-Laplace equation (AYLE), which relates the curvature at any point along the drop interface to the pressures acting on that point scaled by the EIT.

1.3 Marangoni transport using phospholipids

The lungs naturally produce pulmonary surfactant, which is necessary for normal expansion and gas exchange. Phospholipids are a natural component of this pulmonary surfactant and, as such, would make an ideal candidate for Marangoni-driven drug delivery in the lung. However, when these phospholipids are dispersed in water, they form stable vesicles that are unable to induce Marangoni flow when delivered to an aqueous subphase. The work in this thesis uses aerosolization of these dispersions to break open lipid vesicles and access the surface-active monomer within in order to promote phospholipid-driven transport. This phospholipid-driven Marangoni transport has the potential to enhance pulmonary drug delivery in patients with obstructive lung diseases, while potentially being a medically safer option than synthetic surfactants.

We will show that aerosolized phospholipid dispersions can locally lower the surface tension of various aqueous solutions and that this surface tension reduction induces surface transport. This, in turn, induces sub-surface transport, which is ideal for carrying non-surface-active components such as antibiotics or other medications. We show that aerosolized phospholipid can transport a medically relevant antibiotic across a mucin subphase similar to that of the lung ASL. This transport occurs over many centimeters, even when a layer

of phospholipid is pre-deposited onto the mucin subphase to mimic the endogenous surfactant found in the lung. Although the surface tension in the lung airways is not decisively known, phospholipid deposition can reduce the surface tension of mucin to ultra-low values (as low as 1 mN/m) and, therefore, will likely be able to induce transport on almost any aqueous subphase. This is promising evidence for the potential use of phospholipid-induced Marangoni transport in drug delivery.

1.4 Behavior of liquid drops delivered to a miscible liquid subphase

In our early work depositing millimeter scale drops of lipid dispersion, it was noticed that the aqueous drops remained visible for long times. Thus we came to study the miscible interfaces of solvent drops slowly dissolving in a polymer solution subphase. In order to better understand the behavior of these miscible drop/subphase systems, we performed a series of experiments where a solvent drop was placed at the air-solution interface and its evolution was observed. Using this system allows us to relate these results to the problem of delivering aqueous surfactant solutions to the aqueous polymer solutions found in the lung. Our setup allows us to examine the capillary forces on the drop through its wetting condition on the surface. It also allows us to examine the pressures on the drop via the drop curvature.

In our system, we see clear evidence of an EIT between a polymer solution and its solvent. Drops of solvent atop a polymer subphase recover from perturbation, follow proper wetting conditions, and maintain rounded, capillary shapes for long times. Additionally, our system involves very small gravitational driving forces (a small density difference between drop and subphase), so we have a very sensitive probe of the pressures acting on the drop. Disjoining pressures can be measured acting on our solvent drops large distances away from

the interface, and they can span the full height of those drops, which suggests that we may probe the tail end of the disjoining pressure far from the interface. We also observe the power-law radial growth, slow evolution, and eventual disappearance of solvent drops as their interfaces diffuse. This in-depth study of the behavior of systems with miscible drops is not only interesting physics in itself, but it also applicable to many systems including that of pulmonary drug delivery.

Chapter 2

Enabling Marangoni Transport through Aerosolization of Lipid Dispersions

Much of the work in this chapter is published in the following manuscripts:

Enabling Marangoni flow at air-liquid interfaces through deposition of aerosolized lipid dispersions. **A.Z. Stetten**, G. Moraca, T.E. Corcoran, S. Tristram-Nagle, S. Garoff, T.M. Przybycien, and R.D. Tilton. *Journal of Colloid and Interface Science*, 2016.

Aerosolizing Lipid Dispersions Enables Antibiotic Transport across Mimics of the Lung Airway Surface Even in the Presence of Pre-existing Lipid Monolayers. S.V. Iasella, **A.Z. Stetten**, T.E. Corcoran, S. Garoff, T.M. Przybycien, and R.D. Tilton. *Journal of Aerosol Medicine and Pulmonary Drug Delivery*, 2017.

2.1 Introduction to Lipid Transport

2.1.1 Background on Marangoni transport using phospholipid dispersions

For years, researchers have studied the ability of Marangoni flows to induce surface transport. Previous work from our group has shown that a variety of surfactants can be used to induce surface tension gradients and Marangoni flows when delivered to air-liquid interfaces, as long as the surface tension of the delivered solution is lower than that of the subphase. Various soluble surfactants such as sodium dodecylsulfate (SDS) – an anionic surfactant, Capstone FS-3100 – a nonionic fluorosurfactant, hexadecyltrimethylammonium bromide – a cationic surfactant, and Tyloxapol – a nonionic, oligomeric surfactant have been shown to be good spreaders on various model subphases [58, 65, 97, 99, 100]. Due to their potential use in pulmonary drug delivery applications, we are now examining the ability of phospholipids, natural components of pulmonary surfactant, to induce Marangoni flow.

Phospholipids have not been studied extensively as spreading agents at aqueous interfaces, but they are already being used in the lung as components of drug formulations to treat infant respiratory distress syndrome (IRDS). In this context, their role is surface tension reduction in the pulmonary respiratory zone. Most currently marketed surfactant replacement therapies (SRTs) used in IRDS treatment are multi-component dispersions of purified lung surfactant from animals. These contain lipid as well as peptide components. Previous work from our group has shown that these multicomponent SRTs can do more than just lower surface tension; when aerosolized, they can initiate Marangoni flow [77]. In this thesis we show that even single-component phospholipid vesicle dispersions induce Marangoni flow, provided that they are aerosolized en route to deposition. Thus, aerosolization may enable phospholipids to serve as spreading agents without the need for other excipients.

There has been a significant amount of previous work to study the surface activity of phospholipids such as dipalmitoylphosphatidylcholine (DPPC), comprising investigations of lipid monolayers deposited out of organic solution, and investigations of aqueous dispersions of DPPC. The former are the familiar Langmuir trough studies of lipid monolayer surface pressure/molecular area behavior, which examine the different types of structures that lipid monolayers can form on the surface and how such layers behave at their collapse pressures (for a thorough review, see [72]). The latter involve preparing lipid vesicle dispersions and monitoring their surface tensions as some vesicles break open and release surface-active lipid molecules. Both types of investigations focus on the ability of phospholipids (or phospholipids in combination with other components such as lung peptides) to lower surface tension; they do not directly probe phospholipids' ability to initiate Marangoni flow on a liquid surface (for examples, see [24, 60–62, 70, 74]).

By examining the surface pressure/area per molecule isotherms for various phospholipids, it is clear that these monolayers have the potential to reach surface tensions much lower than that of the clean subphase onto which they are deposited. Here, surface pressure is defined to be the difference in surface tension between that of the clean subphase and that of the subphase with added surfactant. This suggests that there is the possibility of creating surface tension driven flows. References for dimyristoylphosphotidylcholine (DMPC) and DPPC surface pressure/area per molecule plots created using a Langmuir trough give collapse pressures (the maximum surface pressure achieved before monolayer collapse) between 37 and 71 mN/m [30,31,43,69,73]. This wide variability is due to differences in the experimental conditions used to collect the data. The rate of compression of the monolayer will strongly affect collapse as well as the fact that many Langmuir troughs will lose some lipid to leaks or adsorption to the trough walls. More recent trough studies with more advanced experimental setups tend to give higher collapse pressures and may be closer to the true thermodynamic isotherms of the monolayers [25, 73].

Franses and his coworkers have extensively studied the surface-active properties of DPPC [60–62,117]. In their work, they see that freshly prepared aqueous dispersions of pure DPPC have surface tensions near that of water, and then decrease in surface tension at rates depending on lipid processing. In the absence of surface compression/expansion cycles, the long-time surface tensions of these dispersions range from 63 mN/m achieved over about an hour and a half for larger vesicles down to 48 mN/m achieved over an hour for the smallest prepared vesicles in their experiments. When other components, such as bovine serum albumin, are added to these dispersions, the same gradual decrease in surface tension is observed, however the minimum surface tension achieved is lower. The minimum surface tensions achieved by any of these dispersions, without any compression or expansion of the interface, is around 26 mN/m. If the surface area is pulsated, the minimum surface tensions achieved decreases to around 1 mN/m. This indicates that static interfaces of aqueous dispersions containing DPPC, as would likely be the case in the lung airways, could have surface tensions of order 20 mN/m, whereas dynamic interfaces, as would likely be found in the alveoli, could be as low as 1 mN/m.

The vesicles contained in phospholipid dispersions are not surface active at the air/water interface in their intact form. The hydrophobic tails of the lipid molecules are sequestered within bilayers, and the head groups lack an attraction to the air/water interface. Furthermore, the vesicles are stable and exist in equilibrium with an extremely low concentration of free lipid monomer (the dominant surface tension lowering species) in solution, on the order of 10^{-8} M [14]. At these small concentrations of free monomers, the surface-active material to be found in these dispersions is insufficient to rapidly and locally lower the surface tension, a condition necessary to induce Marangoni flow. The mechanism behind any significant surface tension reduction of these dispersions is understood as two processes in series, one diffusional and one kinetic [70]. To create an adsorbed layer, vesicles must first diffuse to the surface and then those at the surface must break open to release surface-active

lipid monomers. Over short times and for low concentrations of lipid, this system is regulated by diffusion and no measurable surface pressure is created. Over longer times and for higher lipid concentrations, a surface layer is created that lowers the surface tension of the dispersion. There is evidence that the resulting surface layer may not be simply a monolayer; it is most likely made up of multilayer mesophases [60, 62, 70] . Although all of the DPPC dispersions that were studied in the aforementioned references did, eventually, achieve lower surface tensions than that of water, the authors did not attempt to use the dispersions as transport agents to initiate Marangoni flow across a liquid surface.

2.1.2 Background on Marangoni transport for drug delivery in the lung

Cystic Fibrosis (CF) causes airway mucus to become dehydrated and viscous, leading to bacterial infections and obstructed airways. Disease-associated obstructions may limit drug penetration or cause local aerosol deposition upstream of diseased areas [12, 22, 90, 107]. In cases of CF, aerosols tend to deposit preferentially onto the upper branches or obstructions in the lungs, but infections can occur beyond these areas, deeper in the lung [12]. Delivery of surfactant-containing aerosols to the ASL would locally lower the ASL surface tension and generate flows on the surface and within the ASL that could transport medication over the mucus plaques to reach infection sites deeper in the lung. Because the phospholipid DPPC is endogenous to the lung it is a prime candidate for addition to aerosols as an exogenous surfactant to enhance their spreading.

Prior work from our group has examined how aerosol deposition flux affects the post-deposition flow behavior of the aerosol contents [58, 100]. Two different deposition flux regimes were studied. In the high flux regime, which occurs in the larger airways, aerosol droplets deposit so quickly that they coalesce into a single, large drop before spreading [58].

This large drop's spread area depends on the amount of surfactant deposited rather than on the rate of deposition or the surfactant concentration of the aerosol formulation, provided it exceeds a threshold value sufficient to produce a surface tension lower than that of the subphase. In the low flux regime, occurring in the smaller airways of the lung, each individual aerosol droplet spreads out before the next droplet deposits [100]. This creates a spreading field of droplets that do not coalesce after deposition. The transition between these two regimes occurs at deposition fluxes of ~ 0.01 μL/cm^2 /s [58].

A significant question concerning the possible use of aerosols formulated with surfactants for pulmonary delivery is the uncertain impact of endogenous surfactants on the intended spreading behavior. In order for surface transport to occur, the local surface tension induced by newly deposited surfactant must be lower than that of the pre-existing, potentially phospholipid-covered ASL. Phospholipids exist at high concentrations in the lung's alveoli, where a low surface tension is necessary to prevent the collapse of the alveoli by capillary forces, increase alveolar volume, and promote oxygen exchange. As the alveoli expand and contract, their surface tensions cycle between $\sim$ 30mN/m and $\sim$ 5mN/m [11, 21, 87, 96]. Phospholipids also exist in the airways further up from the respiratory zone at lower concentrations than in the alveoli; the distribution of phospholipids among the airway generations is, as yet, unknown [115]. The ASL surface tension also depends on the presence of mucus. The surface tension of the mucus plaques must reflect the adsorption of the hydrophobic groups of the mucins to the air/water interface, which will lower the mucus surface tension below that of water. Measurements of entangled porcine gastric mucin (PGM) solutions have shown surface tensions between 30 and 40 mN/m. Endogenous lipid on the ASL could lower the mucus layer's surface tension even further [27, 41], but with the exceptions of the alveolar surface where airway surface areas cycle significantly, ASL surface tensions are unlikely to reach a value lower than $\sim$ 20 mN/m [11,51,63,96]. Nonetheless, an important step in developing an aerosol capable of reaching obstructed areas throughout the lung will be to

show that aerosols can transport antibiotics despite the presence of endogenous surfactant. We do so in this thesis.

2.1.3 Summary of our results

We prepared similar, single component phospholipid dispersions to those prepared by Franses and collaborators (described above and in references [60–62, 117]) and deposited them as microliter drops onto a water subphase. These dispersions did have lower surface tensions than water, however they showed no evidence of the ability to induce Marangoni transport. Typically if one deposits a drop of fluid onto a subphase that has higher surface tension than that of the drop, the gradient in surface tension will induce flow towards the higher surface tension region. However, we are depositing very small volume (microliter) drops onto a much larger volume (20 mL) subphase. These small deposited volumes produce dilute dispersions upon mixing into the subphase. According to Launois-Surpas and coworkers, dilute dispersions have slow rates of surface-induced vesicle break-up, and thus the process of surface tension reduction is diffusion-limited and negligible surface pressure will be created [70].

In this thesis, we show that aerosolization is one simple method by which we may induce aqueous phospholipid dispersions to create the surface tension gradient required for Marangoni spreading. Prior work has shown that aerosolization can break liposomes down into smaller aggregates [35, 108] and can break open the aggregates contained in SRT formulations [81]. We postulate that aerosolization can do the same to the stable multilamellar vesicles of pure DPPC and DMPC dispersions; it can actively release monomer from vesicles, store this monomer by adsorption on the surfaces of individual microscopic aerosol droplets, and allow this monomer to be transferred onto a fluid subphase after droplet deposition. This will result in the creation of a lipid monolayer generated by fusion of the lipid layers

from the many depositing aerosol droplets, which will locally lower the surface tension of the subphase. When aerosol deposition is confined to a limited region of the subphase, the surface tension gradient induced by this local surface tension reduction induces Marangoni transport across the surface.

We use three subphases in this work: water, aqueous poly(acrylamide) (PA) solution, and aqueous porcine gastric mucin (PGM) solution. The latter two are used to mimic the ASL of the lung. PA and PGM both contain long polymer chains that are of a similar molecular weight to those found in the ASL. PGM has a fairly low surface tension, which is likely close to that found in the lung. PA has a higher surface tension near that of water and, therefore, acts as a bridge between experiments on water and experiments on PGM.

In addition to inducing spreading, the deposition of aerosolized phospholipid allows the surface to reach ultra-low surface tensions, < 5 mN/m, which are generally only obtainable under extremely slow compression of a lipid monolayer or on area cycling in a Langmuir trough [60, 73]. Attaining these ultra-low surface tensions in the deposition region means that a surface tension gradient will be generated by the aerosol deposition and flow will occur even on subphases with initial surface tensions below that of water, such as PGM. This Marangoni flow is also associated with subsurface flows that provide an additional possible transport path for non-surface-active drugs included in the aerosol formulation.

The behavior of DPPC on the surface of mucin solutions has not been studied and is crucial to the understanding of how Marangoni spreading might be achieved in the lungs. This thesis will show that when DPPC is deposited onto a mucin solution surface, the surface tension at high areas per DPPC molecule (a dilute monolayer) is significantly smaller than it is on a simple water subphase. At small areas per DPPC molecule (a dense monolayer), the surface tension isotherm converges with the isotherm on a simple water subphase. This is strong evidence that at high densities DPPC is forming a monolayer and excluding most if not all mucin hydrophobic groups that might have been adsorbed to the air/water interface

before DPPC deposition. This high-density layer has an extremely low surface tension (< 5 mN/m) meaning that, if we create such a layer through aerosolization, it will likely induce outward Marangoni transport against the higher-surface-tension preexisting layer in the lung.

In order to mimic this drug transport in the lung, we measured the extent of phospholipid-induced transport of the antibiotic tobramycin across a surface of a PGM solution subphase. We used DPPC as the surfactant spreading agent in this aerosol formulation. As this surfactant is endogenous to the lungs, we pre-deposited DPPC on the mucin solution surface in order to determine if endogenous lipid would prevent enhanced transport of the tobramycin. We found that the lipid aerosol formulation causes surface flow outward from the region of deposition and transports the tobramycin over biologically relevant distances across the surface. In addition, the presence of pre-deposited lipid does not significantly affect the spreading of the tobramycin across the surface.

2.2 Experimental Materials and Methods

2.2.1 Materials

Preparation of Lipid Vesicle Dispersions

DMPC and DPPC were purchased from Avanti Polar Lipids in the lyophilized form (>99% purity) and were used without further purification (for molecular structures, see Figures 2.1 and 2.2). These two phospholipids were chosen for our experiments because DPPC is the most abundant lipid in natural pulmonary surfactant and DMPC is similar, but has a main bilayer phase transition temperature (TM) of 24°C [16], whereas DPPC's is 41.4°C [83]. Conducting experiments at room temperature thus allowed us to examine the dependence of spreading on the phase of the lipid. All experiments were performed between 24 and 26°C.

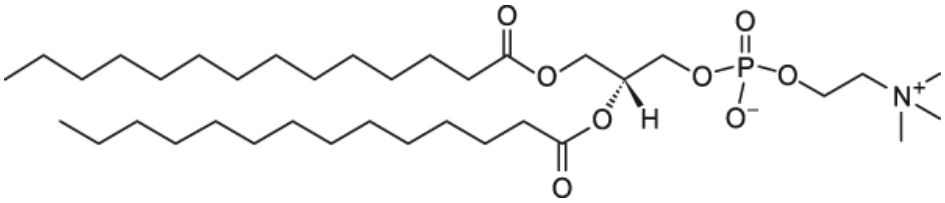

Figure 2.1: Molecular structure of dimyristoylphosphotidylcholine (DMPC). Image from product manufacturer, Avanti Polar Lipids.

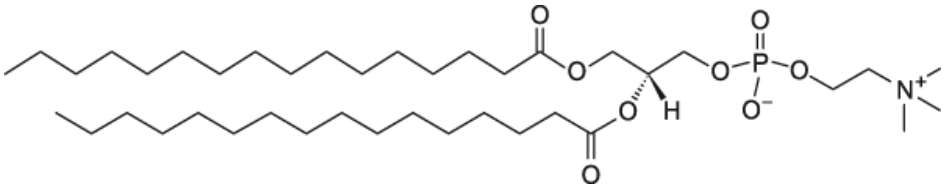

Figure 2.2: Molecular structure of dipalmitoylphosphotidylcholine (DPPC). Image from product manufacturer, Avanti Polar Lipids. Note the only difference between this and the structure of DMPC is the longer carbon tail.

The majority of our experiments were conducted using dispersions of multilamellar lipid vesicles (MLVs) prepared using a standard temperature-cycling process [111]. We prepared

a 20 mL vial of 10 mg/mL DMPC or DPPC in deionized (DI) water. The deionized water was purified using a Millipore, Milli-Q Academic unit and had a resistivity of 18 MΩ·cm and a surface tension of 72.7 ± 0.7 mN/m; the quoted uncertainty here and elsewhere is the standard error of the mean for the stated number of trials, three in this case. The lyophilized lipids and water were first mixed for 30 seconds using a vortex mixer (Fisher Scientific Analog Vortex Mixer, CAT# 02215365.) The dispersion was then warmed ∼ 20°C above TM, into its fluid phase, for 10 minutes, mixed on the vortex mixer for 30 seconds, and then chilled ∼ 20°C below TM for an additional 10 minutes. This process was repeated three times in order to achieve a dispersion of approximately 10 μm diameter MLVs [42].

Secondary experiments were conducted using dispersions of small unilamellar vesicles (SUVs) prepared using ultrasonication. Again, we prepared a 20 mL vial of 10 mg/mL phospholipid in DI water. The lyophilized lipids and water were then sonicated at least 20°C above TM using a probe ultrasonicator (Branson Sonifier Cell Disruptor 185, Emerson Electric Co.) in 3-minute bursts, allowing the dispersion to cool for 5 minutes in between bursts. This process was continued until the dispersions were optically clear yielding approximately 250-450 Å SUVs [38, 89].

In order to compare transport induced by pure phospholipids to that induced by natural lung surfactant, further trials were conducted using Infasurf (calfactant) and Curosurf (poractant alfa). Infasurf was donated for experimental work by ONY Inc, Amherst NY. Curosurf (Chiesi USA, Cary, NC) was obtained from collaborator Dr. Timothy Corcoran at the University of Pittsburgh School of Medicine.

Preparation of Subphases

Three subphases were used in this work: DI water, aqueous porcine gastric mucin (PGM) solutions, and aqueous poly(acrylamide) solutions (PA).

Poly(acrylamide) of molecular mass 5 – 6 MDa (CAS# 9003-05-08) was purchased in

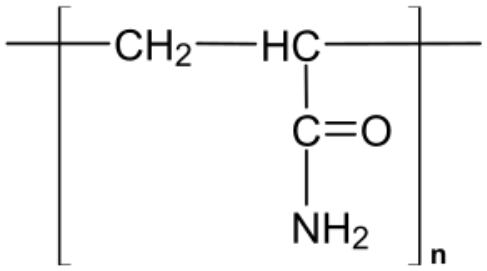

Figure 2.3: Molecular structure of poly(acrylamide) (PA). Image from Wikipedia.

powder form from Polysciences (Warrington, PA) and used as received (for structure, see Figure 2.3). Aqueous solutions of 1% w/w PA were prepared in DI water by adding the PA powder in increments of 2 g every 2 – 3 days in a 3/4 full 1 L bottle under nitrogen with continuous gentle mixing on a gyratory shaker (New Brunswick Scientific, Edison, NJ, model G79, speed "4"). The gyratory shaker was used in place of magnetic stirring so as not to damage the very long chains of the polymer in solution. After adding the final 2 g of powder, water was added to bring the total volume up to 1 L, and stirring continued for 2 – 3 more days or until the solution was homogeneous, whichever took longer. PA solution concentrations were above the previously reported 0.45% w/w entanglement concentration [97]. The surface tension of the PA solution after pouring a fresh sample was 70.8 ± 0.5 mN/m, which typically decreased by approximately 1 – 2 mN/m over 5 minutes and then stabilized.

Porcine gastric mucin (PGM; Type II, bound sialic acid 1% CAS# 84082-64-4) was purchased from Sigma Aldrich. PGM's structure is not well defined, but contains a mixture of gel-forming mucins or mucus glycoproteins. The PGM was stored between 2°and 8°C while not in use and was rehydrated with DI water. A 5% w/w solution of PGM was prepared in DI water and stirred magnetically for approximately 14 hours, at which point the solution was visually homogeneous. The 5% w/w concentration is above the entanglement concentration of PGM in water [6,65]. The prepared PGM solutions were stored between 2°– 8°C and used

within 4 – 5 days of preparation. The surface tension of the 5% w/w PGM solution was 38.3 ± 3.5 mN/m, and typically decreased by 2 – 3 mN/m over 5 minutes after pouring a fresh sample.

Preparation of Tobramycin

Tobramycin (> 94.0%, TCI America, Portland, OR, CAS# 32986-56-4) was purchased and used at a concentration of 60 mg/mL in the aerosol formulations (for structure, see Figure 2.4). Tobramycin is commonly used to treat CF-associated infections [101,106]. Tobramycin is also highly water soluble, allowing it to be incorporated into the aqueous solution of aerosol formulations. It is not dispersed in the MLV bilayers as would be required of a hydrophobic drug. It is added to the lipid dispersions after they are prepared. Control experiments determine if tobramycin alone can drive spreading. For these experiments, the aerosol formulation consisted of only tobramycin and DI water.

2.2.2 Methods

Aerosolization Methods

Most aerosolization experiments were performed with an AeroNeb Solo micropump nebulizer (Aerogen, Galway, Ireland) with an Aerogen Pro-X controller. Each nebulizer consists of a fluid chamber, at the bottom of which is a 5 mm wide mesh plate containing approximately 1000 tapered, 4.8 ± 0.3 μm holes. When this mesh is vibrated at 120 kHz, the holes act as micro pumps, each pumping out uniform droplets of dispersion. Aerosol droplet size was measured by laser diffraction using a Malvern Mastersizer (Malvern Instruments, Worcestershire, UK). For aerosolized DMPC dispersions, the average volume median droplet diameter was 5.7 ± 0.1 μm (with volume median 10th and 90th percentile values of 2.5 ± 0.1 μm and 11.1 ± 0.4 μm). As a reference, the average droplet diameter for a 0.9% saline

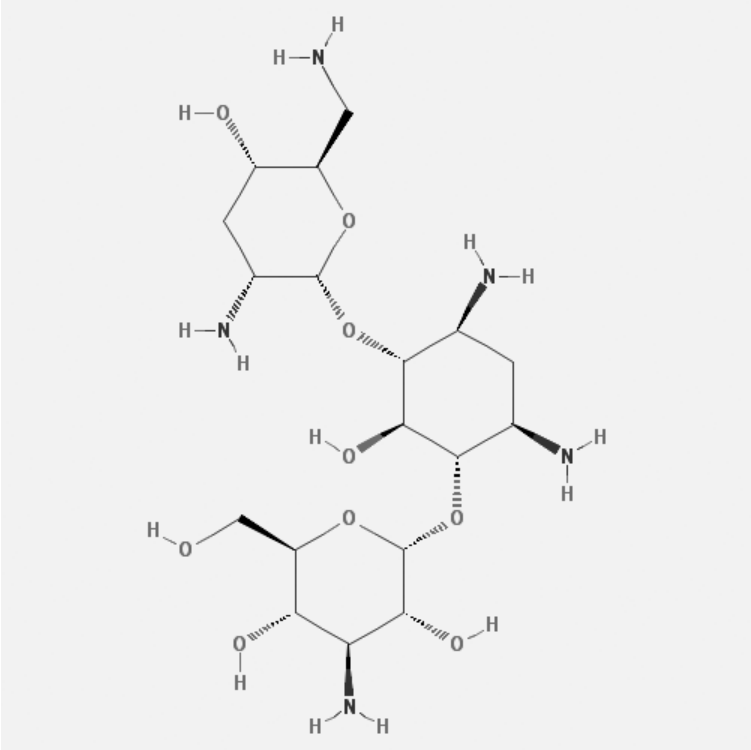

Figure 2.4: Molecular structure of tobramycin. Image from PubChem.

solution was 4.3 ± 0.1 μm (with volume median 10th and 90th percentile values of 2.0 ± 0.1 μm and 8.4 ± 0.3 μm).

For experiments conducted with DPPC and tobramycin, the size distribution was determined for each aerosol produced. They are compared in Figure 2.5. The size distributions are close enough in all cases that we do not expect significant variation in our spreading results based on aerosol size.

In a second set of experiments designed to determine whether the mechanism of aerosol generation would affect the ability of lipid dispersions to drive Marangoni flows, we used an AeroEclipse® II Breath Actuated Nebulizer purchased from the Monaghan Medical Corporation in Plattsburgh, NY. In this nebulizer, fluid is drawn up through narrow tubing, driven by a dry nitrogen flow of between 3 and 8 liters per minute, forming a jet that breaks up

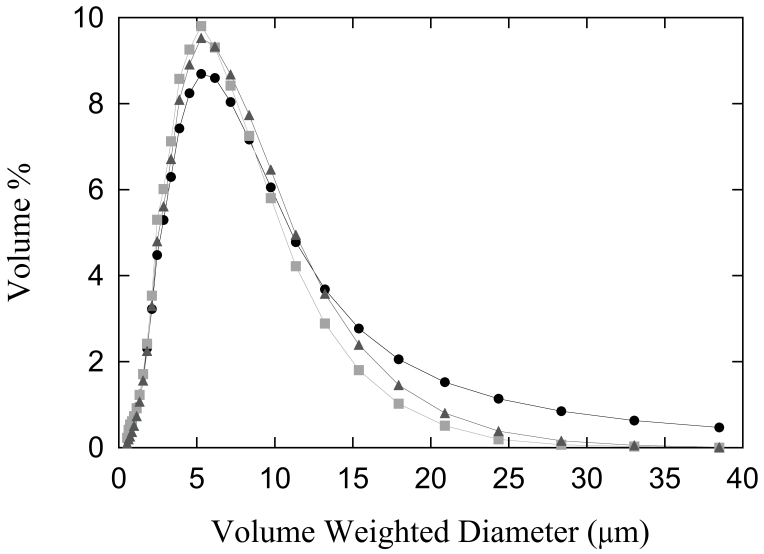

Figure 2.5: Size distribution of aerosols from AeroNeb Solo micropump nebulizer. 10 mg/mL DPPC (circles), 60 mg/mL tobramycin (squares), 10 mg/mL DPPC and 60 mg/mL tobramycin (triangles). Errors on all points are 0.1 μm (n = 3). For aerosols containing tobramycin at a concentration of 60 mg/mL, the volume-weighted median droplet diameter was 5.0 μm, with volume-weighted 10th and 90th percentile values of 2.0 μm and 10.7 $\pm$ 0.2 μm. The volume-weighted median droplet diameter for a tobramycin and DPPC dispersion was 5.3 μm (with volume-weighted 10th and 90th percentile values of 2.2 μm and 11.7 μm). The volume-weighted median droplet diameter for a DPPC dispersion was 5.5 $\pm$ 0.2 μm (with volume-weighted 10th and 90th percentile values of 2.1 μm and 14.2 $\pm$ 1.3 μm).

into small aerosol droplets due to capillary instabilities and an impaction surface.

Both of these medical nebulizers were designed to deliver a consistent total dose of medication when the full reservoir is emptied. The rate of nebulization can vary during the emptying of the reservoir, as discussed below. In addition, the total time to empty the reservoir can vary from nebulizer to nebulizer and trial to trial. Despite this variability in nebulization rates, consistent experimental trends yielded robust conclusions.

Because the nebulization rate of these nebulizers varies from trial to trial and within trials, it is important to make note of the nebulizer's behavior during any given trial. If a

nebulizer is old or is trying to nebulize while empty or clogged, it will tend to nebulize poorly (low rate) or in spurts. When this happened in our experiments, we would thoroughly clean the nebulizer with ethanol and water and then nebulize a mixture of ethanol and water (in a fume hood, as nebulized ethanol would be dangerous to breathe). If this did not fix the problem, or if any physical damage was seen within the nebulizer, we would replace it. Due to the difficulty in cleaning, separate nebulizers were used for every type of solution to be nebulized. The nebulizers were numbered and a record was kept of which nebulizer was used in each trial.

Creation of Lipid Isotherms

DMPC surface pressure/area per molecule isotherms on water were measured in a 14 cm glass Petri dish using the Wilhelmy pin apparatus. The phospholipid was dissolved in chloroform and deposited drop-wise onto a water surface using a glass syringe. The chloroform was allowed to evaporate and the surface tension was allowed to equilibrate after each drop was deposited. The area per molecule was calculated using the known concentration of the solution, the volume of the drops deposited, and the size of the Petri dish.

Trough Setup

We built an experimental trough setup designed to permit simultaneous measurement of surface tension and observation of Marangoni flow outside of the region of aerosol deposition (see Figure 2.6). The setup consisted of a poly(vinyl chloride) trough 2 cm wide by 2 cm deep by 20 cm long. This trough was filled with 20 mL of deionized water, or other subphases as specified, giving a depth of 0.5 cm. At this depth, the gravitational parameter associated with Marangoni spreading, G, is greater than 3. $G = (\rho g H^2) \,/\, S$ where ρ is the subphase density, g is acceleration due to gravity, H is subphase depth, and S is the spreading coefficient (surface tension of the clean surface minus that of the deposited dispersion), which is at most

72 mN/m [34]. When this parameter is greater than 0.5, as it is in our case, recirculation beneath the advancing capillary ridge can occur within the subphase and dewetting of the underlying solid surface should not, and does not, occur [34].

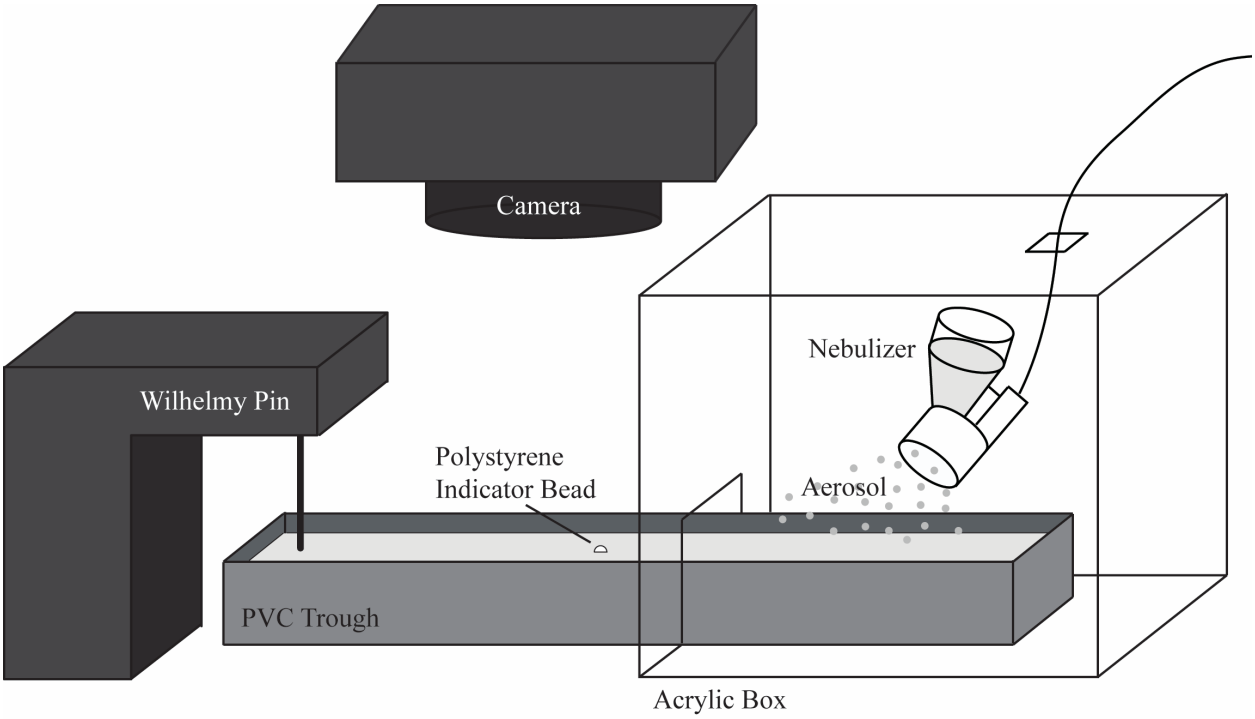

Figure 2.6: Diagram of trough setup. Dimensions of the trough are 20 cm long by 2 cm wide by 2 cm deep. The aerosol deposition is perpendicular to the long axis of the trough at a declination of approximately 45°.

This subphase-filled trough extended through a small opening half way into a clear acrylic box (approximately 12 cm deep in the direction of the trough by 20 cm wide by 18 cm tall). The acrylic box housed the nebulizer and served to contain the depositing aerosol. In this way, direct aerosol deposition was confined to the half of the trough within the acrylic box. A plastic shield (not shown) was then lowered to cover as much as possible of the remaining opening where the trough protruded. Little aerosol escaped the box as indicated by laser scattering near the exit. Within 20 seconds of turning on the nebulizer (for a 10 minute experiment), the containment box reached 90% relative humidity, as read by a Sensirion

humidity gauge (Sensirion Sensor Company, Stafa, Switzerland). Within 30 seconds, the relative humidity reached 95% and continued to increase slowly with time. We, therefore, believe that drying of the aerosol en route to deposition is not a significant effect. This high-humidity, aerosol-filled box was generally quite opaque and one could barely see the nebulizer within.

Note that great care was taken to make sure the nebulizer did not drip onto the subphase. Because the aerosol being produced by the nebulizer is very low surface tension, accumulated excess liquid falls easily and would cause unwanted Marangoni spreading if it fell directly from the nebulizer onto the subphase surface. The nebulizer lip was never directly over the trough and the nebulizer was positioned at an angle to the surface to ensure that no drips landed on the subphase.

The surface tension approximately 9 cm away from the area of deposition was monitored with a Wilhelmy pin apparatus (Nima Technology Limited, Coventry, England). A platinum Wilhelmy pin was used for all experiments. Fluid flow at the surface was observed using a small polystyrene indicator bead, approximately 1 mm in diameter, placed on the fluid surface just outside of the acrylic box and observed with a Nikon 3600 digital camera. The Wilhelmy pin has a positive meniscus, as does the wall of the trough, meaning that the two will attract one another if they are placed too close together. In order to keep this from happening, the pin was placed at the center of the trough at least half a centimeter, or approximately twice the capillary length of water, away from the end of the trough (capillary lengths for water, PA, and PGM are 0.27 cm, 0.26 cm, and 0.20 cm respectively). The trough must also be wider than twice the capillary length so that there is a relatively flat region in the center in which to place the pin, which is why our trough is two centimeters wide.

Images were analyzed using NIS-Elements Advanced Research software (Nikon Instruments Inc, Melville, NY) to track the particle trajectory. The indicator bead centered itself in the trough due to capillary forces, thus only the position along the length of the trough varied

with time. This position was marked using the "particle tracking" option in NIS-Elements. If the contrast between bead and subphase was high enough, automatic particle tracking could be used. This was not always the case with our white bead against a PVC-gray or mucin-yellow background, so we, instead, used manual particle tracking.

Placement of the bead was somewhat difficult in these experiments. The bead would often move on the surface before spreading could occur (from random vibrational or Brownian motion as well as air currents in the room). This was compounded by the fact that it took a few minutes after turning on the nebulizer until transport was seen. If this random motion carried the bead inside the box, the bead could not be tracked due to the opacity of the aerosol mist. This is the reason why many of our trials begin with the bead not being tracked.

Modified Trough Setup for Tobramycin Detection

Further spreading experiments were performed with the addition of the antibiotic tobramycin in order to investigate whether aerosolized phospholipid deposition can cause transport of hydrophilic drugs. These spreading experiments were conducted with fellow graduate student Steven Iasella. We designed and performed spreading experiments together and he developed and performed the experiments to assay for tobramycin concentration.

A modified version of our trough setup was designed in order to measure the surface concentration of the tobramycin outside the area of direct aerosol deposition while providing adequate containment of the tobramycin, as shown in Figure 2.7. The setup consisted of a glass trough 2 cm wide by 2 cm deep by 20 cm long. The trough was placed halfway inside an aerosolization chamber, as in the original trough design. Then the trough was filled with 70 mL, $\sim$ 2 mm below the top of the tough, of 5 wt% mucin solution in order to minimize the gap between the liquid surface and the top of the hole in the aerosolization chamber through which the trough extends. This limited the amount of aerosol that could escape

through the air and deposit onto the liquid surface outside the aerosolization chamber. To further prevent any aerosol from leaking through the hole and onto the outside portion of the trough, air was slowly and constantly pulled in through the hole and out the opposite side of the aerosolization chamber through a filter into a containment chamber by a small fan. Results discussed below show that these precautions were sufficient to reduce aerosol flux to the trough surface outside the aerosolization chamber to insignificant levels. This was more necessary in the case of tobramycin deposition than it was in the pure lipid case because of the sensitivity of the tobramycin assay.

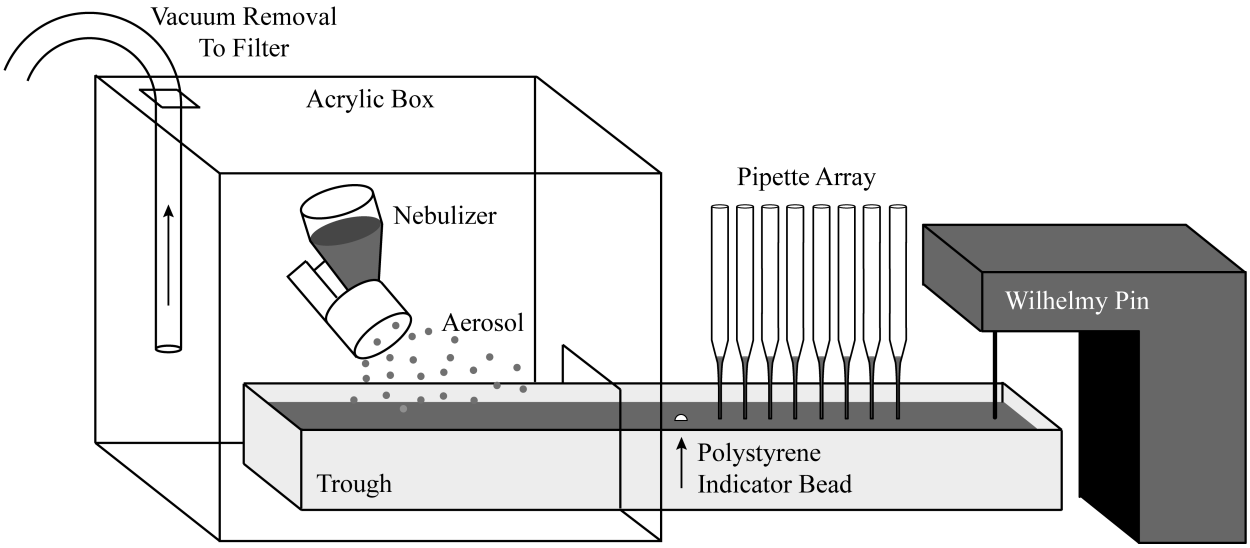

Figure 2.7: Diagram of trough setup. Dimensions of the trough are 20 cm long by 2 cm wide by 2 cm deep. The aerosol deposition is perpendicular to the long axis of the trough at a declination of approximately 45°. This setup differs from the previous version in Figure 2.6 in that it contains a bias flow and is enclosed in a glove box. This means that tobramycin transport data was taken independently (via the array of pipettes) from surface tension data (taken with the trough outside the glove box).

A 1 mm diameter polystyrene tracer bead was placed on the surface of the liquid in the trough to indicate the presence of surface flows. The nebulizer was charged with 4 mL of the aerosol formulation and allowed to operate until empty. This entire apparatus was placed in a glove box to prevent tobramycin from leaking into the laboratory environment. Because

the experiments containing tobramycin occurred within this secondary glove box, we had to wait for a number of minutes after the nebulizer had been turned off to be sure that any aerosol within the glove box had settled out of the air.

In order to determine the spatial distribution of the tobramycin after aerosol deposition had occurred and spreading had been completed, samples of the liquid surface were taken by touching an array of 11 disposable glass Pasteur pipettes (Corning Inc., Corning, NY, Cat# 7095B-5X) to the mucin surface. Capillary action caused a small amount of liquid, $\sim$ 10 μL, to be drawn from the surface region into the pipettes. Independent experiments with fluorescent dye spread across a liquid surface showed that each pipette sampled a region of approximately 0.3 cm diameter. Each sample was deposited into 2 mL polystyrene vials and diluted with 200 μL of DI water. Five surface samples were also taken from inside the region of direct deposition. These samples were assayed for their tobramycin concentration as will be described in Section 2.2.2. To determine the average aerosol flux to the surface during the experiment and normalize for differences between experiments, all the fluid in the trough was thoroughly mixed after surface samples were taken and a 200 μL sample of this mixture was diluted with 200 μL of DI water. The resulting bulk sample was assayed for tobramycin content and used to determine the total tobramycin dose to the subphase. Knowing the tobramycin concentration in the aerosol formulation, we calculated the total volume of solution deposited from which we determined the average volumetric deposition flux.

To mimic the impact of endogenous lipid on tobramycin transport, trials were performed where DPPC was pre-deposited from a 10 mg/mL DPPC solution in chloroform via pipette onto PGM. The chloroform was allowed to evaporate before delivery of the tobramycin aerosol. The pre-deposited lipid layer had an area per molecule of $\sim$ 52 Å^2, determined from the measured surface tension and the surface tension isotherm for DPPC monolayers on mucin solutions to be discussed later. For reference, if the deposition had been on a

pure water subphase, this would have been in the "liquid condensed" phase [73]. This surface concentration produces the lowest subphase surface tension, or equivalently, the largest surface tension barrier to Marangoni spreading possible by chloroform deposition, and is, thus, a strong test of spreading against any endogenous lipid that might be present on the ASL within a given airway generation.

Separate experiments were conducted with a Wilhelmy pin apparatus in place at the far end of the trough to record the surface tension during spreading. These experiments were not conducted with tobramycin present in the solution because the Wilhelmy pin apparatus could not be contained in the secondary glove box. Surface tension measurements were recorded at a point 8 cm away from the region of deposition. In these experiments, surface flow was observed by imaging a 1 mm diameter polystyrene particle on the subphase surface.

Determination of Total Lipid Mass Delivered

We made a series of gravimetric measurements to assess the total aerosolized lipid deposition mass as well as its deposition profile versus time when using the AeroNeb vibrating mesh nebulizer. A thin piece of aluminum foil was weighed and placed over the portion of an unfilled trough within the enclosure to mimic the area and location of aerosol deposition in the experiment. The nebulizer was then allowed to deliver a known volume of DMPC dispersion. The foil was dried in a vacuum oven overnight and then re-weighed to determine the total amount of deposited lipid.

In order to determine the concentration of the nebulizer output with time, we aerosolized lipid for multiple consecutive two-minute periods directly into a series of pre-weighed beakers. We then weighed each liquid-filled beaker, dried each in a vacuum oven overnight, and then re-weighed the dry lipid. The results, shown in Figure 2.8, indicate the concentration of the lipid in the aerosol – as determined by mass balance – increases as the nebulizer reservoir empties.

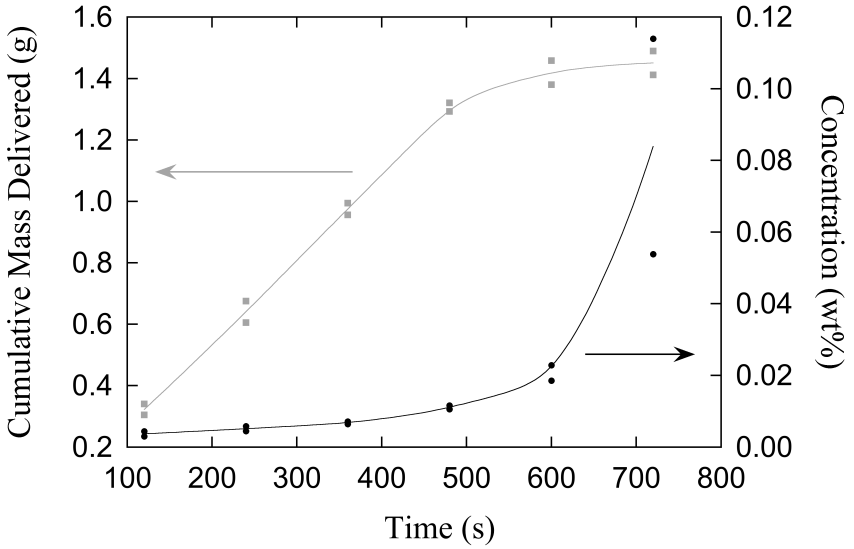

Figure 2.8: Cumulative liquid mass delivered by the nebulizer and lipid concentration in the DMPC aerosol taken simultaneously (data for two trials plotted). Error bars on experimental mass measurement are ± 0.0001 g, which is within plotted points. These are measurements made over two minute intervals, which average over unsteady output of the nebulizer. The lines are guides to the eye.

Before each nebulization experiment, the lipid dispersions were mixed on a vortex mixer in order to re-homogenize the mixture after it had settled in storage. It was observed that the total amount of lipid delivered was dependent on the amount of time between vortexing and nebulization. The nebulizer tended to deliver less lipid when there was a longer period for the dispersion to settle after being vortexed. Because of this finding, we would always vortex lipid dispersions immediately before any nebulization experiment.

Ellipsometry to Characterize Surface Properties

We used ellipsometry to characterize the phospholipid layer deposited from the aerosol onto the water surface. These experiments were conducted with the help of collaborator Dr. John Riley (recent graduate from Dr. Tilton's group). The surface layer was probed using the

632.8 nm laser beam of a phase-modulation picometer ellipsometer (Beaglehole Instruments, Ltd.). Measurements were made near the Brewster angle, 52°, at three spatially separated points on the surface to check for consistency.

Ellipsometry detects adsorbed layers at interfaces by measuring the change in ellipticity, ϵ, of a polarized laser beam upon reflection from a surface. Ellipticity is defined as the ratio of the complex reflection coefficients from the parallel ($r_{\|}$) and perpendicularly ($r_{\perp}$) polarized components of the incident beam. Ellipsometry data is then, generally, represented using ellipsometric angles Ψ and Δ:

$$\epsilon = \frac{r_{\|}}{r_{\perp}} = \tan\Psi \; e^{i\Delta} = \mathrm{Re}(\epsilon) + \mathrm{Im}(\epsilon)$$

$$\mathrm{Re}(\epsilon) = \tan\Psi \;\cos\Delta \quad ; \quad \mathrm{Im}(\epsilon) = \tan\Psi \;\sin\Delta$$

In Beaglehole instruments such as that used for this experiment, data is, instead, represented using parameters x and y, where

$$x = \mathrm{Re}(\epsilon)\frac{2}{1+\mathrm{Re}(\epsilon)^2+\mathrm{Im}(\epsilon)^2} \quad \text{, and} \quad y = \mathrm{Im}(\epsilon)\frac{2}{1+\mathrm{Re}(\epsilon)^2+\mathrm{Im}(\epsilon)^2}$$

yielding the Δ parameter,

$$\Delta = \arctan\frac{y}{x}$$

which is directly proportional to the surface excess polarizability and is, thus, proportional to the thickness of the adsorbed layer.

Because the experimental trough was too narrow to align under the ellipsometer, measurements were performed on a half-covered 14 cm Petri dish with direct deposition in the uncovered region and transport into the covered region. Ellipsometric results were the same both within and outside the region of deposition. The standard ellipsometric parameter Δ

was reported for DMPC monolayers deposited from chloroform solutions and compared with the Δ values for a layer created via aerosolization.

Detection of Subsurface Transport

To analyze the fate of all material being delivered in addition to the monolayer at the surface, we also monitored the sub-surface fluid using dark field microscopy. We used a Nikon AZ100 microscope (Nikon Instruments Inc, Melville, NY) with an AZ-Plan Apo 4 x objective and 8 x zoom. The microscope camera (model DS-QiMc-Nikon) had 0.6 x magnification. This allowed us to detect and track lipid aggregates that appeared in the subphase during aerosol deposition.

Detection of Tobramycin

The tobramycin concentration in samples from the spreading trough was determined by a closed enzyme donor immunoassay (CEDIA, Tobramycin II, Thermo Fisher Scientific, Waltham, MA, Reference number 100018). This method has a detection limit of 0.2 ng/mL and a measurement precision of 0.1 ng/mL) [47]. The samples were compared to a calibration curve comprising assays of tobramycin solutions of known concentrations in water (0.2 ng/L to 6 mg/mL).

2.3 Lipid Isotherms

We used our method of sequential deposition of drops dissolved in chloroform to create DMPC and DPPC surface pressure/area per molecule (Π/A) isotherms on various subphases including water, PA solution, and PGM solution. These plots have proven useful in understanding the spreading behavior of aerosolized lipid. Note that true isotherms are defined thermodynamically and do not depend on experimental conditions. Our Π/A plots approach, but are not identical to these true, thermodynamic isotherms.

2.3.1 Isotherms for DMPC on water, PA, and PGM

Figure 2.9 shows isotherms for DMPC on water at $\sim$ 25 °C. Surface pressure is defined as surface tension of bare subphase minus surface tension of surfactant laden subphase. As can be seen in the figure, there is some variability from trial to trial in our isotherms, especially in regions of rapid surface pressure change. This is likely due to a combination of experimental error in the exact volume of the 0.5 μL drops placed and extreme sensitivity of the isotherm in regions with high slope. Despite this variation, our isotherm is in good agreement with literature isotherms for DMPC at room temperature (see, for example, references [30, 31, 43, 69, 73]).

In the literature for monolayers of DMPC at room temperature, the area per molecule at which isotherms lift off (when a detectable non-zero surface pressure is achieved) is reported between 90 and 130 Å^2 per molecule. The area per molecule at monolayer collapse is reported between 45 and 60 Å^2 per molecule. These lift-off and collapse areas match well with our plots. The actual surface pressure at collapse, which is the result of kinetic processes, varies depending on the method and experimental details used to create and compress the monolayer. There is no liquid-expanded/liquid-condensed coexistence region seen for DMPC on water at this temperature, suggesting that these experiments are above DMPC's monolayer

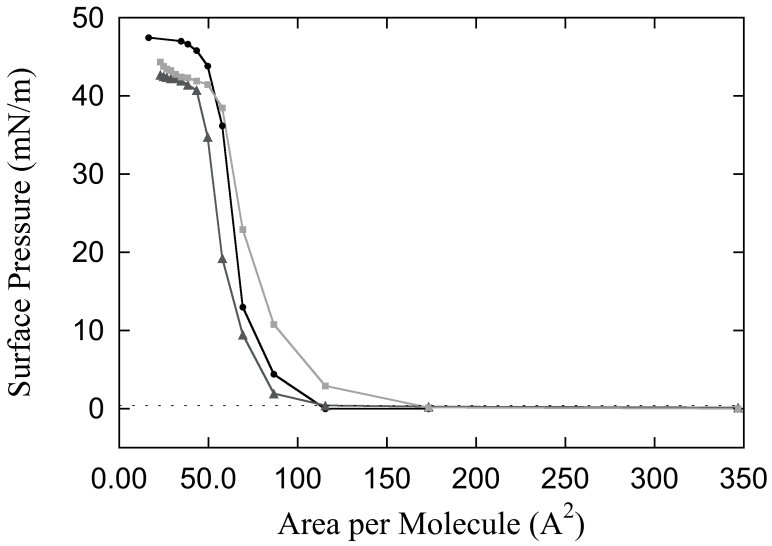

Figure 2.9: Surface pressure versus area for DMPC on water. Data are shown for three separate trials. For each trial, surface pressures were calculated using the reference surface tension of the clean interface before deposition.

critical temperature.

isotherms were created for DMPC on PA and PGM subphases using the same technique of depositing droplets of lipid dissolved in chloroform onto these subphases. The results are shown in Figures 2.10 and 2.11. There are some notable differences between the results on each subphase. On PA, a higher surface concentration of DMPC is required to achieve a detectable surface pressure, and the monolayer approaches collapse in a more linear fashion. This may be due to some interaction between the DMPC and the polymer in the subphase. If the DMPC interacts with the polymer and some lipid is, thus, lost to the subphase, it will not be present at the surface to induce a surface pressure, which will shift the results to smaller areas per molecule.

PGM's isotherm is quite different from the other two. This is, in part, because PGM begins at a far lower surface tension. Additionally, as soon as DMPC is added, there is

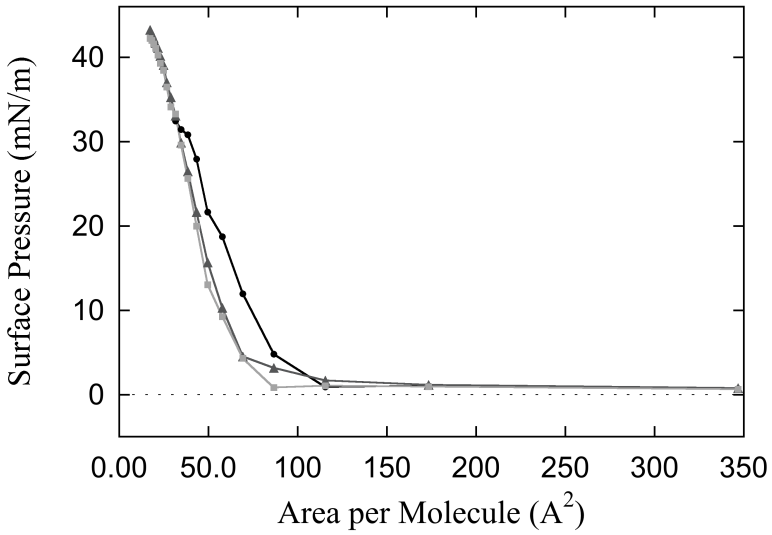

Figure 2.10: Surface pressure versus area for DMPC on 1% 5 MDa PA solution. Data are shown for three separate trials. For each trial, surface pressures were calculated using the reference surface tension of the clean interface before deposition.

immediately a detectable surface pressure. This suggests that there is some interaction between the PGM and the DMPC, which will be discussed in the following section.

2.3.2 Isotherms for DPPC on water and PGM

Figure 2.12 contrasts the isotherms for DPPC on water and on a 5 wt% PGM solution in a similar manner as was done for DMPC in the previous section. The monolayer on water illustrates important features. A low surface pressure gas phase exists at large areas per molecule. A liquid expanded phase appears, followed by a low slope liquid expanded/liquid condensed coexistence region that transitions to a liquid condensed phase at $\sim$ 55 A^2 /molecule. These features all agree well with the literature [71]. At very small areas per molecule the liquid condensed monolayer begins to collapse at a surface pressure of $\sim$ 40 mN/m, or surface tension of $\sim$ 32 mN/m. The collapse surface pressure achieved by this method is the same

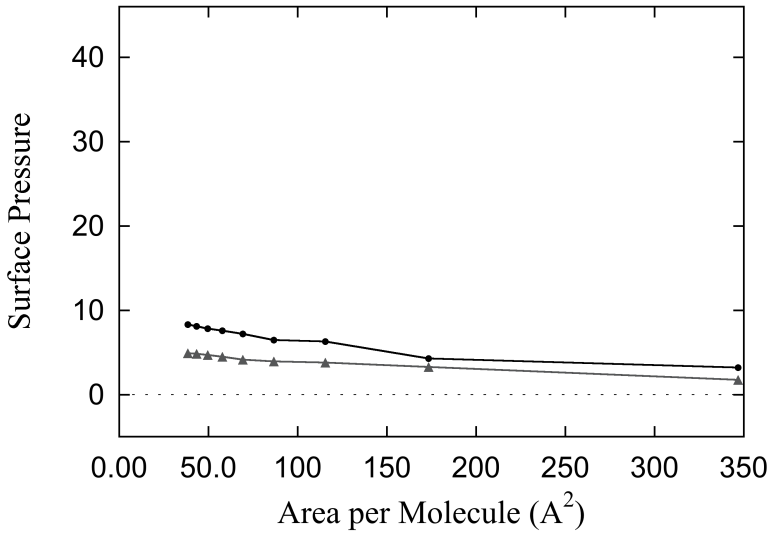

Figure 2.11: Surface pressure versus area for DMPC on 5% PGM solution. Data are shown for two separate trials. For each trial, surface pressures were calculated using the reference surface tension of the clean interface before deposition.

as that achieved by a concentrated dispersion of DPPC vesicles in water equilibrating with the air/water surface [61].

The Π/A isotherm on the 5 wt% PGM solution lacks many of these features. First, it should be borne in mind that a surface pressure of zero on the PGM solution subphase corresponds to a surface tension of $\sim$ 40 mN/m, whereas it would be 72 mN/m on a simple water subphase. Thus the PGM solution surface is occupied by a significant amount of hydrophobic mucin segments before any lipid is deposited. Accordingly, the surface pressure begins to increase at much larger areas per DPPC molecule than on water, an indication that the mucin polymers adsorbed to the air/water interface are interacting with the deposited DPPC. In this range of large areas per molecule, the compressibility of the DPPC layer on PGM solution is significantly less than that on water. At low area per DPPC molecule the surface pressure of the DPPC layer on PGM solution levels off to an apparent collapse at

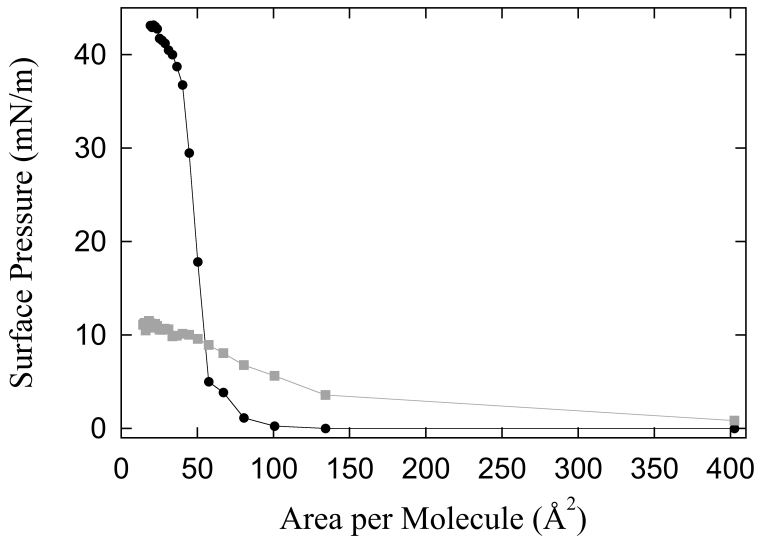

Figure 2.12: Surface pressure vs area for DPPC on water (black circles) and on a 5 wt% PGM solution (gray squares). Surface pressures were calculated using the surface tension of 72 mN/m for water and the surface tension of 40 mN/m for the mucin solution as reference surface tensions. Each of these sets of data is an individual trial.

a value far below the collapse pressure on water. However, the surface tensions on PGM solution and water subphases converge (Figure 2.13). This indicates that the DPPC is able to completely displace the mucins from the surface when DPPC is present at high surface concentrations.

The behavior of DPPC on a mucin solution subphase is significantly different than on water. The Π/A isotherm shows that DPPC on a mucin solution is significantly less compressible (there is a higher slope) at low surface concentrations and significantly more compressible at high surface concentrations than DPPC on water. While it is unclear what is happening at a molecular level on the surface, mucins appear to interact with the DPPC at high areas per molecule in order to lower the surface tension. The simplest explanation is a compression effect: as both polymer segments and lipids share the surface, the area available

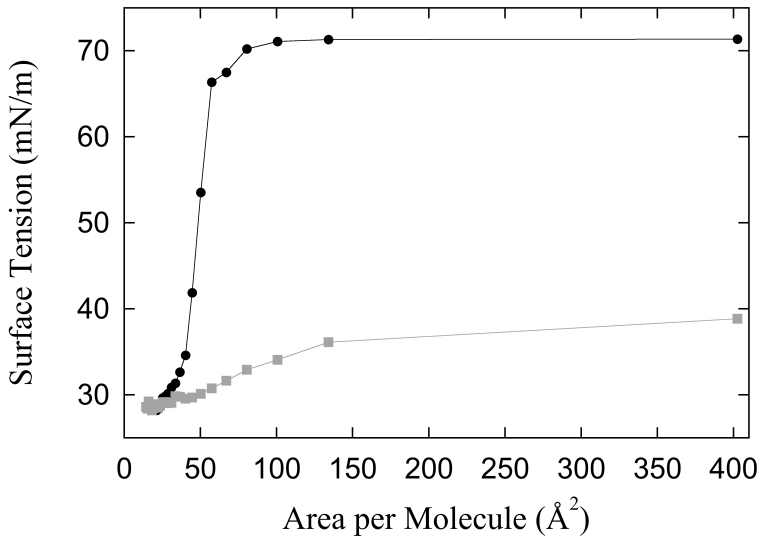

Figure 2.13: Surface tension vs area for DPPC on water (black circles) and on a 5 wt% PGM solution (gray squares). At low area per DPPC molecule the surface tension for both subphases converges to $\sim$ 29 mN/m. Note that these data are from the same trials as that in Figure 2.12.

to each is less and the surface tension decreases [19]. While the behavior of the monolayer on these two surfaces is different, the final, equilibrium surface tension achieved is the same for both subphases ($\sim$ 29 mN/m). This indicates that it is likely that the DPPC is completely displacing mucin chains from the surface at the highest surface concentrations.

2.4 Deposition of Microliter Drops of Lipid Dispersion

As shown in Figure 2.14, microliter drops of DMPC MLV dispersion neither reduce the surface tension outside the drop nor induce Marangoni flow. This figure depicts a typical trial in which a series of 10 μL drops of 10 mg/mL DMPC dispersion were pipetted onto a clean water surface every 10 seconds. Upon deposition of these drops, a very small decrease in surface tension from that of water is discernible, with a fitted slope of approximately -0.001 mN/m/s. The indicator particle on the surface does not move beyond observed baseline average noise arising from extrinsic laboratory conditions including minor vibrations and air currents.

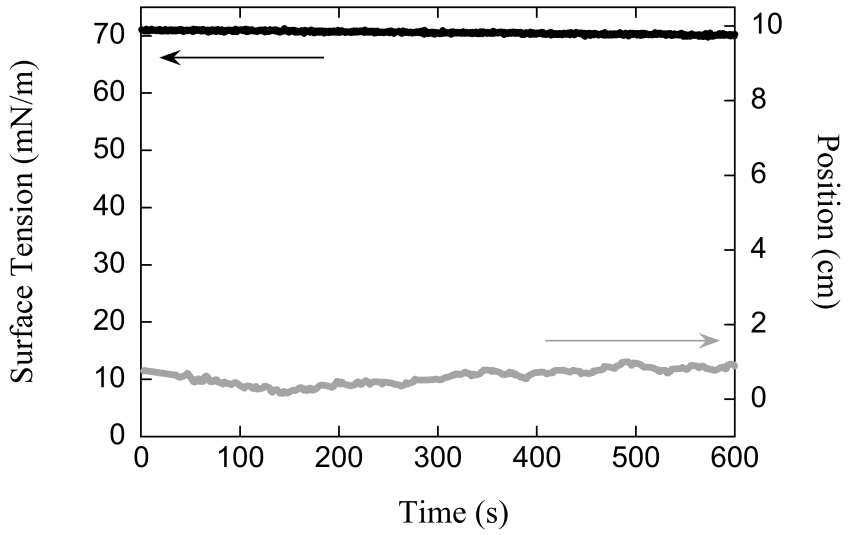

Figure 2.14: Simultaneous measurements of surface tension and indicator bead position for dropwise lipid dispersion deposition. Deposition of microliter drops of 10 mg/mL DMPC dispersion onto a DI water subphase. Ten μL droplets of 10 mg/mL DMPC was deposited every 10 seconds for the duration of the experiment.

During this experiment, enough total lipid monomer was deposited to create over 600 lipid monolayers on the trough surface, yet there was still no indication of surface tension reduction

or indicator bead transport. These results show that drops of DMPC MLV dispersion do not contain enough available surface-active material to create a surface tension gradient sufficient to induce Marangoni flow or to lower the surface tension remote from the deposition location. Similar negative results were seen with drop-wise deposition of fluid-phase SUV dispersions that had been prepared by ultrasonication as well as similar dispersions of DPPC.

As mentioned in the methods section for this chapter, when nebulizing lipid dispersion onto a surface, we had to be careful of drips from the nebulizer. These drips of freshly-nebulized dispersion induced Marangoni transport, which would disrupt aerosolization experiments. In order to determine if the mere process of nebulization would be sufficient to create stable dispersions capable of inducing Marangoni flow, we deposited microliter drops of freshly nebulized dispersion onto our subphases. In these experiments, a 10 mg/mL DMPC dispersion was nebulized directly into a beaker and then 10 μL microliter drops of this freshly collected nebulized dispersion, taken from the bulk fluid below the surface, were successively pipetted onto a clean water surface. The drops were pipetted within a minute of being nebulized, yet they also showed no ability to lower the surface tension of the water remote from the point of drop deposition or to move an indicator particle. Since we will show in the next section that the aerosolization process does deliver surface-active species to the subphase surface, the negative result here must be due to re-aggregation of the surface-active species within a minute of the aerosol droplets being subsumed into a bulk fluid in the beaker. These results are similar to those of Minocchieri and coworkers, who report cryo-TEM evidence that nebulized Curosurf SRT vesicles re-aggregate rapidly after nebulization into bulk fluid [81].

2.5 Deposition of Aerosolized Lipid Dispersions

2.5.1 DMPC transport on water

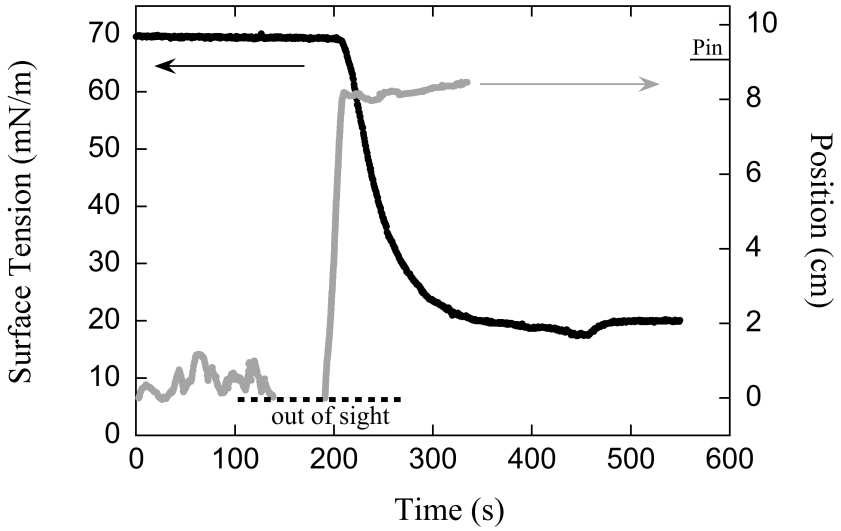

Figure 2.15: A representative plot of surface tension and position versus time during aerosolized DMPC dispersion deposition. In this trial, 4 mL of 10 mg/mL DMPC dispersion were aerosolized via an AeroNeb Solo vibrating mesh nebulizer onto a clean DI water surface. Aerosol deposition begins at 0 seconds and ends at 450 seconds. The Wilhelmy pin is located at approximately 9 cm.

As shown in Figure 2.15, aerosolized lipid dispersions deposited directly from the aerosol phase onto the subphase surface reduce surface tension outside of the deposition region and induce Marangoni flow. Four mL of 10 mg/mL DMPC dispersion are aerosolized via an AeroNeb vibrating mesh nebulizer above a clean DI water surface while the surface tension and bead position outside the region of deposition are monitored as a function of time. For the experiment shown in Figure 2.15, the nebulizer is turned on at 0 seconds. For the first 2 minutes of deposition, the surface tension decreases very slowly, at a rate of approximately -0.002 mN/m/s. During this time, the bead position fluctuates on the surface with a standard

deviation in position of 0.3 cm (likely due to air currents and vibrations), but its average location does not change significantly. In the case shown, at approximately 2 minutes, the bead's fluctuations on the surface carry it into the containment box, out of the field of view of the camera. At approximately 3 minutes, the Marangoni flow overcomes the random motions of the bead, and it begins to move across the surface at a velocity of 0.37 cm/s; the average speed over seven such trials is 0.20 ± 0.1 cm/s with the variation dominated by run-to-run differences. Here we chose to show an experiment with a slightly above-average transport speed due to the clarity with which this experiment showed all common aspects of these trials.

The bead completely traverses the 9 cm of exposed trough within 30 seconds of the initiation of consistent motion. This motion across the surface is coincident with a lowering of the subphase surface tension. The bead's motion is stopped only when it reaches the end of the trough and runs into the meniscus on the Wilhelmy pin. Towards the end of many experiments, the surface tension reduction causes the bead, which is held at the surface by capillary forces, to sink through the surface to the bottom of the trough. Control experiments performed either without the pin or without the indicator bead show that the Wilhelmy pin measurement does not impact bead motion nor does the bead motion impact the Wilhelmy pin measurement.

In all experiments, aerosolized DMPC deposition resulted in a surface tension reduction to values below 18 ± 4 mN/m. When aerosol was deposited continuously and was not limited by exhaustion of the reservoir charge, surface tensions as low as 1 mN/m could be achieved, as will be discussed below.

There is typically a 3 to 6 minute delay between the start of the nebulizer and the convective movement of the bead across the surface. The Marangoni stress across the trough is initially quite small, resulting in a surface flow that is too weak to overcome the noise-level movements of the bead. There are at least two reasons why the gradient is small at

early times. First, the nebulizer delivers an initially low concentration of lipid to the surface as shown in Figure 2.15. Second, the monolayer isotherm shows that the lipid surface concentration must build to between 130 and 90 $Å^2$/molecule before the monolayer leaves the gaseous phase and develops a significant surface pressure. In fact, many of the features within the lipid isotherms seem to be mimicked in the aerosolization experiments.

2.5.2 Phospholipid transport in other systems

We conducted a number of transport experiments with two different phospholipids (DMPC and DPPC), at two different initial concentrations in the nebulizer (10 mg/mL and 1 mg/mL), with two different nebulizers (jet and vibrating mesh), and on three different subphases (DI water at 72 mN/m, PA at 70.8 $\pm$ 0.5 mN/m, and PGM at 38.3 $\pm$ 3.5 mN/m). The results are qualitatively the same in all cases. All experiments showed significant surface tension reduction and transport of the marker particle across the full length of the trough. The extent of surface tension reduction and the rate at which that reduction occurred were system-dependent. Examples of these experiments are shown at the end of this subsection.

In Figures 2.16, 2.17, 2.18, 2.19, and 2.20, we show examples of experiments performed with two different nebulizers (vibrating mesh and jet) on three different subphases (water, PA, and PGM). All experiments shown here were performed with 10 mg/mL DMPC MLV dispersions. Although the experiments performed with the vibrating mesh nebulizer ran out of material before reaching very low (< 10 mN/m) surface tensions, these low surface tensions were achievable through loading the mesh nebulizer multiple times (see Figure 2.30). This difference is likely due to the fact that the jet nebulizer produces a more directed aerosol mist and, therefore, a greater percentage of the jet nebulizer's aerosol lands on the trough. All of these experiments showed consistent results: the surface tension of the subphase was lowered significantly and the indicator particle fully traversed the experimental trough.

A lower concentration dispersion takes longer to exit the gas/liquid-expanded phase than a higher one does (see Figure 2.21). Surface tension reduction also tends to slow where the isotherms have a phase coexistence region (as can be seen where the surface tension approaches its minimum value in any of the lipid transport figures) due to the fact that, in those regions, packing the surface further does not cause further surface tension reduction. These observations are somewhat qualitative due to the high variability of the nebulizer output at any given time, as was discussed in the methods section.

Examples of transport induced by DPPC rather than DMPC are shown in Figures 2.22 and 2.23. Although DMPC and DPPC are in different bilayer phases at 25°C (DMPC in a fluid phase and DPPC in a gel phase), this phase difference does not seem to have an effect on the ability of their aerosolized dispersions to induce Marangoni transport.

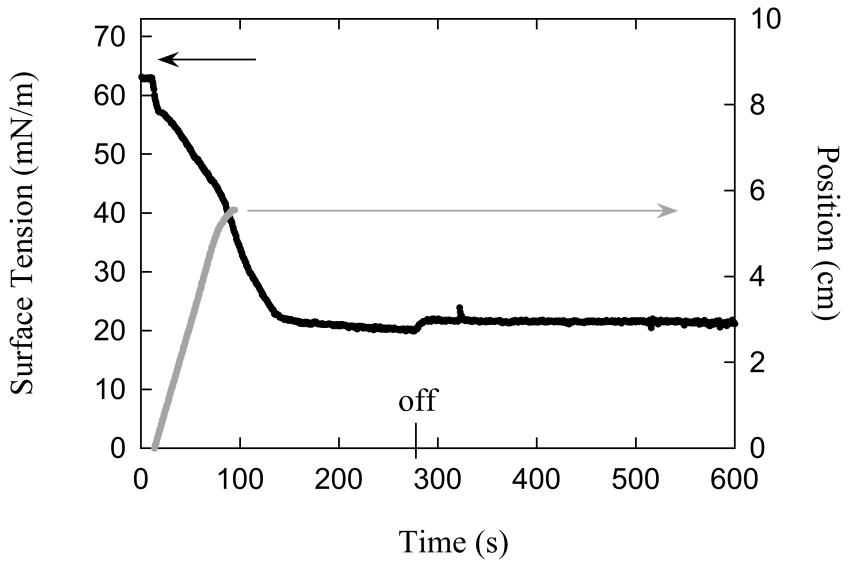

Figure 2.16: 10mg/mL DMPC dispersion aerosolized via AeroNeb vibrating mesh nebulizer to a PA subphase. The point at which the nebulizer turned off is marked "off".

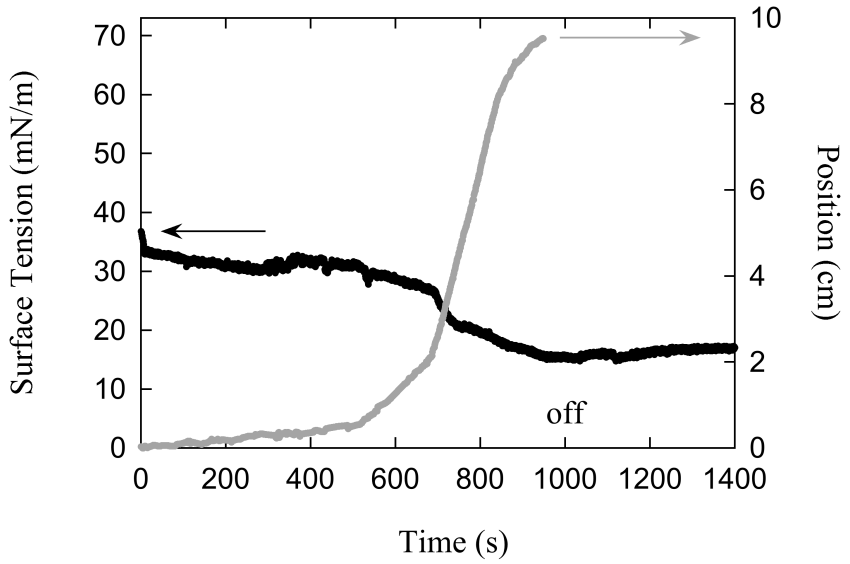

Figure 2.17: 10mg/mL DMPC dispersion aerosolized via AeroNeb vibrating mesh nebulizer to a 5% PGM subphase. The point at which the nebulizer turned off is marked "off".

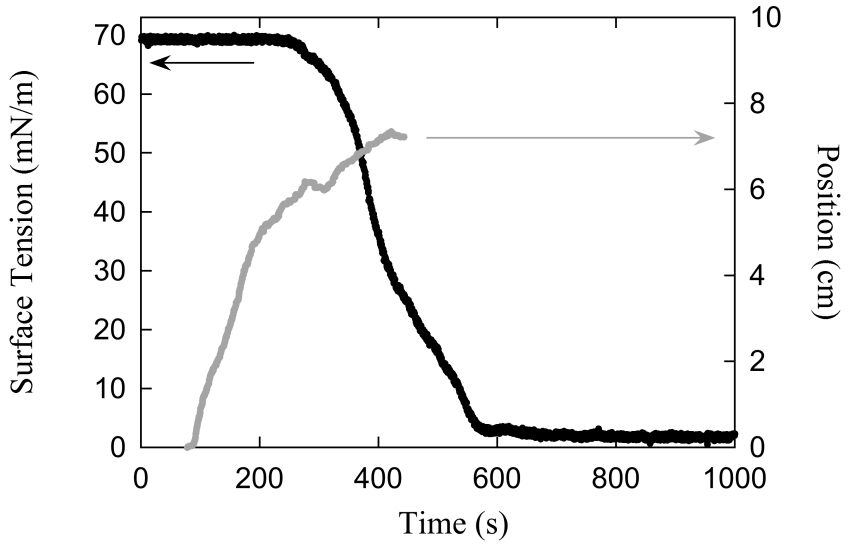

Figure 2.18: 10mg/mL DMPC dispersion aerosolized via jet nebulizer to a DI water subphase.

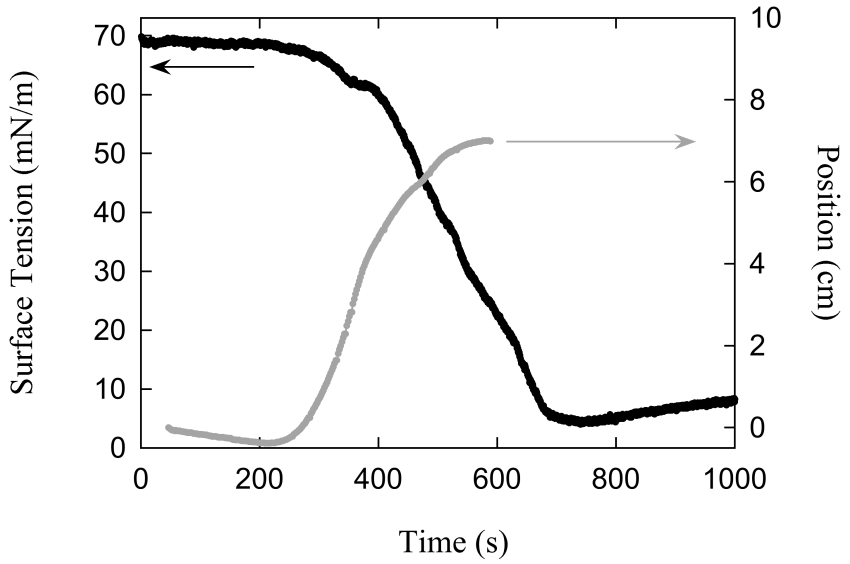

Figure 2.19: 10mg/mL DMPC dispersion aerosolized via jet nebulizer to a PA subphase.

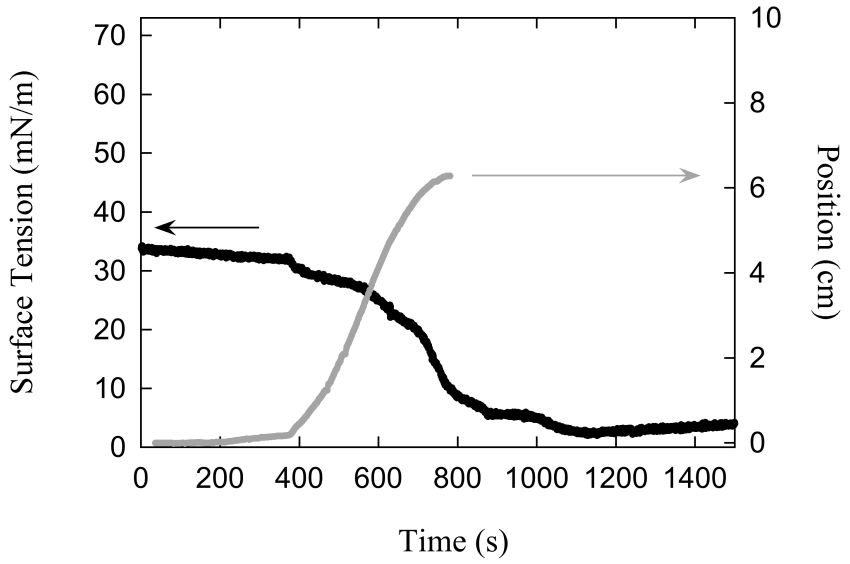

Figure 2.20: 10mg/mL DMPC dispersion aerosolized via jet nebulizer to a 5% PGM subphase.

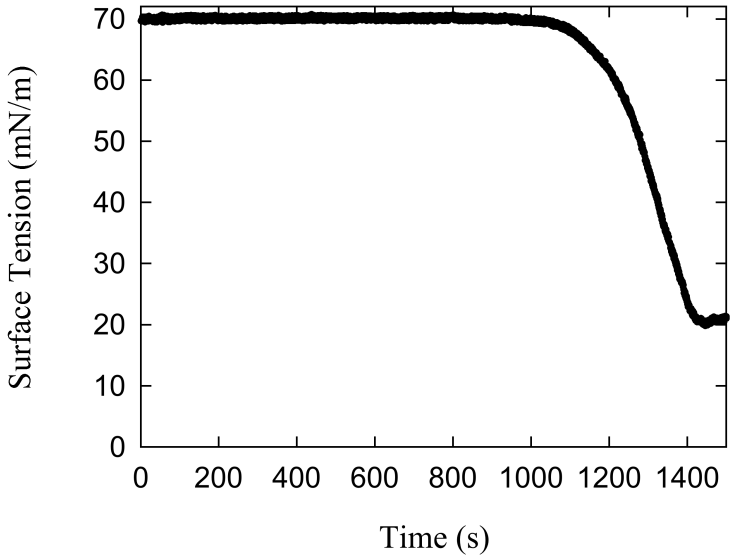

Figure 2.21: 4 mL of 1 mg/mL DMPC dispersion aerosolized via an AeroNeb Solo vibrating mesh nebulizer onto a clean DI water surface. Note that the decrease in surface tension begins to decrease at around 1000 s, where as the decrease began at around 200 s for the 10 mg/mL dispersion.

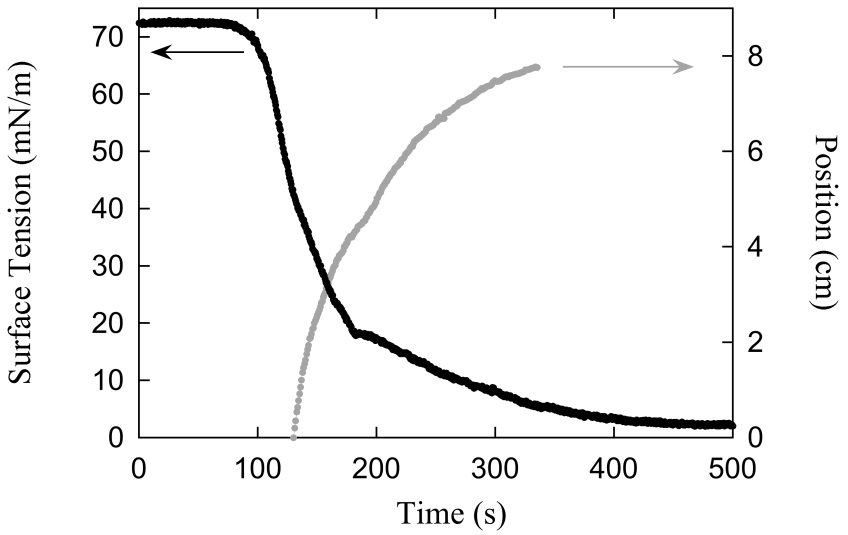

Figure 2.22: 10mg/mL DPPC dispersion aerosolized via jet nebulizer to a DI water subphase.

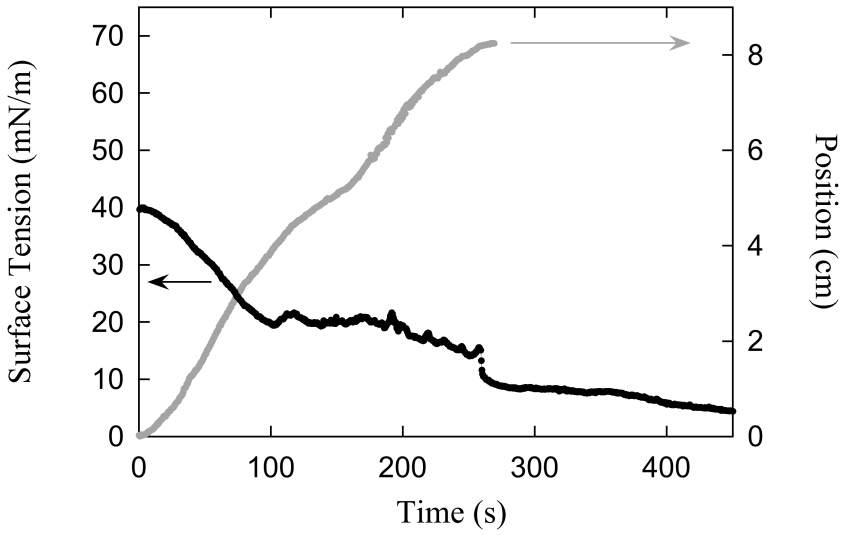

Figure 2.23: 10mg/mL DPPC dispersion aerosolized via jet nebulizer to a 5% PGM subphase.

2.5.3 Inversion of bead and pin placement

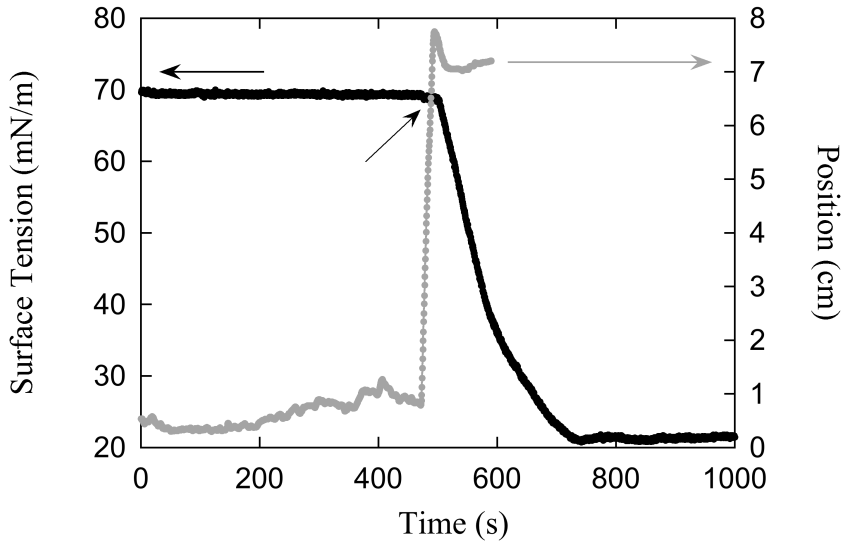

Figure 2.24: 10mg/mL DMPC dispersion aerosolized via AeroNeb vibrating mesh nebulizer onto a DI water subphase. In this experiment, the Wilhelmy pin and polystyrene indicator bead are inverted with the pin just outside the mouth of the deposition box and the bead just past the pin.

In order to be sure that our results were robust and not a function of interaction between the polystyrene indicator bead and the Wilhelmy pin, we switched the placement of the pin to be very close to the entrance of the box. We then placed the polystyrene bead slightly further outside of the box, just past the pin. In these trials, the same bead motion and surface tension reduction was seen as in previous sections. There was one notable difference between these inverted trials and the standard aerosolization experiments. Because the Wilhelmy pin was closer to the aerosol source than the bead was, we expected to see the surface tension dip before the bead moved. What we saw appeared to be the opposite. The bead moved before we saw a significant reduction in surface tension (see Figure 2.24). When we examined the surface tension plot more closely, however, we saw that the surface tension had decreased

very slightly before the bead began to move (see, in Figure 2.24, an arrow pointing out that the bead position increases and crosses the black surface tension data before the surface tension begins its dramatic decrease).

The theory behind Marangoni transport gives insight into this observation. The velocity of Marangoni flow in a 2D trough is given by [26]:

$$v_y = \frac{w^2}{\mu}\left(\frac{d\gamma}{dy}\right)\left(\frac{x}{H} - \left(\frac{x}{H}\right)^2\right)$$

where w is the width of the trough, H is the fluid depth, μ is the viscosity of the fluid, x is the position along the width of the trough, y is the distance along the trough, and γ is the interfacial tension. As can be seen from this equation (or any other form of the Marangoni velocity), the velocity depends directly on the gradient of the interfacial tension along the surface. This means that no matter how small the interfacial gradient, there will be some associated Marangoni driving force. This may not be a large enough force to overcome random noise and be detectable in a given experiment, but it must exist.

In the case of our bead appearing to move prior to a significant dip in surface tension, it is likely simply the case that there is a very small Marangoni velocity associated with a very small difference in surface tension. As the lipid is accumulated on the surface and slowly packs to the point of leaving the gas/liquid-expanded coexistence phase, the rate at which the surface tension is lowered is quite small, and possibly even smaller than the resolution of our Wilhelmy pin apparatus. Thus, the bead is responding to the very first change in surface tension that we cannot necessarily detect. This effect of the bead moving prior to surface tension reduction is not visible in other experiments because, in those cases, the Wilhelmy pin is at the far end of the trough.

2.5.4 Transport with multiple tracer particles

When more than one tracer particle is placed along the surface of the trough, the one closest to the nebulizer moves first, runs into the next, and then the two travel together to the end of the trough (see Figure 2.25). This is significantly different from what is seen when a drop of soluble synthetic surfactant (i.e. SDS) is placed on a dish of water. In the case of the soluble surfactant, there is the same delay in the onset of motion such that the tracers closer to the source move first, but all the particles move outward independently; the inner ones do not catch up to the outer ones and move with them (see [98]). This phenomenon is not yet explained, however, there are similarities in this behavior to that of the difference between the spreading of talc and that of polystyrene beads as seen in Appendix A.1.

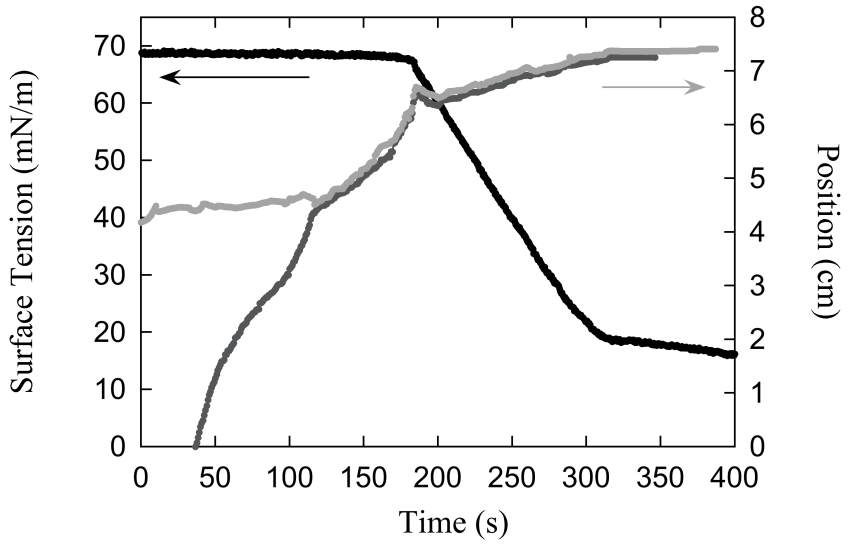

Figure 2.25: 10mg/mL DMPC dispersion aerosolized via AeroNeb vibrating mesh nebulizer onto a water subphase. In this experiment, two beads were placed on the surface. The closer bead to the nebulizer starts moving first (dark gray) and then picks up the second (light gray) as they move across the trough together.

2.6 Structure and Dynamics of the Surface Lipid Layer

2.6.1 Ellipsometry showing lipid monolayer deposition

We used ellipsometry to probe the structure of the surface lipid layer created through aerosol deposition (see Figure 2.26). As a baseline for comparison, a DMPC monolayer was created by sequential deposition of drops of lipid dissolved in chloroform. The chloroform was allowed to evaporate, and then the change in the ellipsometric parameter Δ from the bare subphase was measured. According to the Π/A isotherm for DMPC (Figure 2.9), at surface densities above approximately 0.015 molecules per Å^2, the monolayer begins to collapse. At this point, the molecule per area values no longer represent molecular packing in a monolayer. The change in Δ from the resulting monolayer plateaus at $5.1 \pm 0.1^\circ$.

Ellipsometry was then performed on the lipid layer formed outside of the region of direct DMPC aerosol deposition in a half-covered petri dish. This experiment was done in a stepwise manner by nebulizing for one minute, turning off the nebulizer to take a measurement, and then repeating until the nebulizer was empty. To check that the stopping and starting of the nebulizer had no effect on the layer thickness, this experiment was then repeated without stopping the nebulizer and only the final ellipsometric thickness was taken. The aerosolized DMPC layer thickness plateaus at an ellipsometric parameter of $5.5 \pm 0.4^\circ$ (which, assuming an index of refraction of $n = 1.4$ for DMPC, gives a reasonable monolayer thickness of $\sim$ 17.4 Å). The fact that the ellipsometric thicknesses from these two experiments are so similar strongly suggests that aerosolization causes a monolayer of DMPC to move out of the region of aerosol deposition and across the subphase surface.

Since the ellipsometric data indicate that a monolayer of lipid is forming outside the direct deposition region, we may use the Π/A isotherm to determine the surface density of the lipid in the monolayer on the water surface during our spreading experiments. For the data in Figure 2.15, the surface tension at 280 sec, 27 mN/m, indicates a surface density of

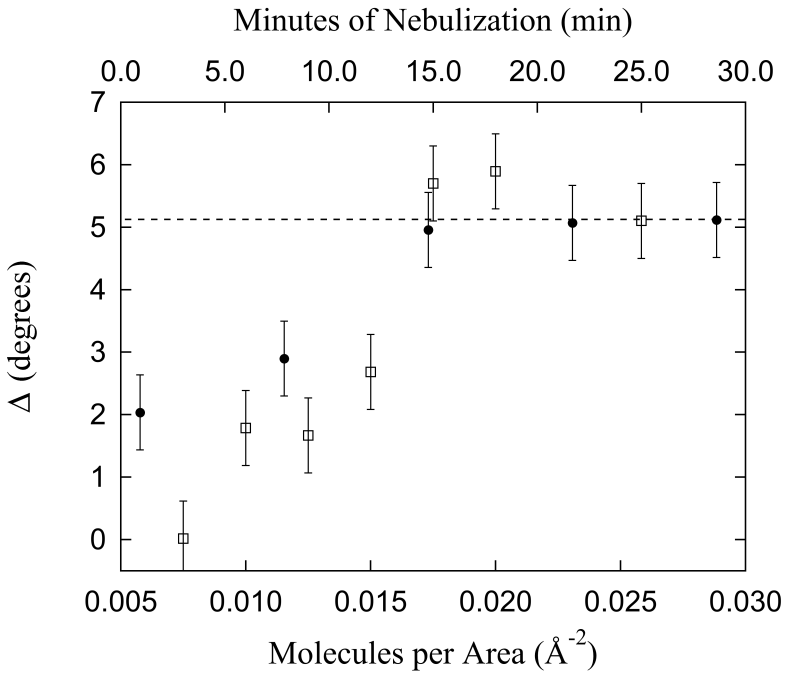

Figure 2.26: Ellipsometric parameters of A) a monolayer deposited out of chloroform (units of molecules per area) shown as filled circles, and B) a surface layer deposited via aerosolization (units of minutes) shown as open squares. The dashed line marks the saturation of the chloroform-deposited monolayer.

59 Å^2/molecule according to the average isotherm from Figure 2.9, and thus a total number of 6.9×10^{15} molecules, or 7.8 μg, in the monolayer on the trough. However, when we weigh the total amount of dry lipid delivered to the surface in a full trial, we get an average total mass of 5.5 $\pm$ 0.2 mg. Adjusting for the fact that these full trial drying experiments run longer than the 280 seconds in the above figure, we can estimate that lipid quantities on the order of a milligram have been delivered by the time in question. Clearly, a significant amount of the total lipid delivered to the trough is not contained in the monolayer.

Note here that ellipsometry was not performed on DMPC or DPPC layers at late times where we see the ultra-low surface tension result. The DMPC monolayers that we did examine would have had time for their surface tensions to recover before the ellipsometry

measurement was taken. This means that we do not have data on whether these ultra-low surface tension surfaces are monolayers or whether they are some more complex surface structure. This would be an interesting topic for future research.

2.6.2 Subsurface transport

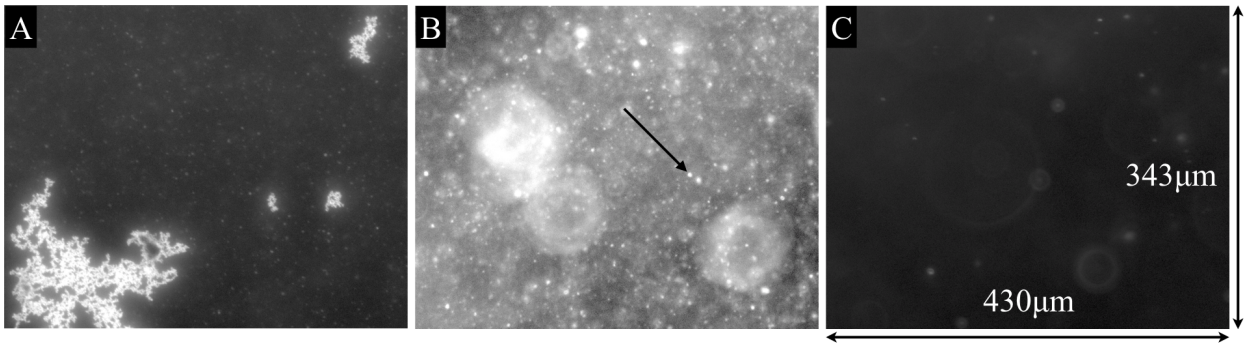

Figure 2.27: Dark field microscopy images of lipid clusters beneath the surface in the area of aerosol deposition. All panels are 430 by 343 μm. A is focused on small chromium dioxide needles that were placed on the water surface in order to be able to focus at the air-liquid interface. B is focused $\sim$ 60 μm beneath the surface. The small ($\sim$ 10 μm), sharply focused bright spots are clusters of lipid. The arrow in panel B points to one such small cluster. The larger, less focused features are the out-of-focus chromium dioxide needles on the surface or other out-of-focus lipid clusters. C is focused $\sim$ 420 μm below the surface and shows very few lipid clusters have been transported this deep into the subphase.

Using dark field microscopy, we were able to visualize the remaining non-monomeric lipid deposited from the aerosol. As shown in Figure 2.27, in the region of direct aerosol deposition immediately post-deposition, we see $\sim$ 10 μm static bright spots that permeate a layer from just below the surface to a depth of $\sim$ 0.5 mm in the water. These bright spots are not present in a control where pure water is aerosolized, leading to the conclusion that the bright spots are lipid aggregates.

These aggregates have unknown structure and are therefore described as "clusters". They are likely composed of re-aggregated lipid MLVs and SUVs. As shown in Figure 2.28, in a

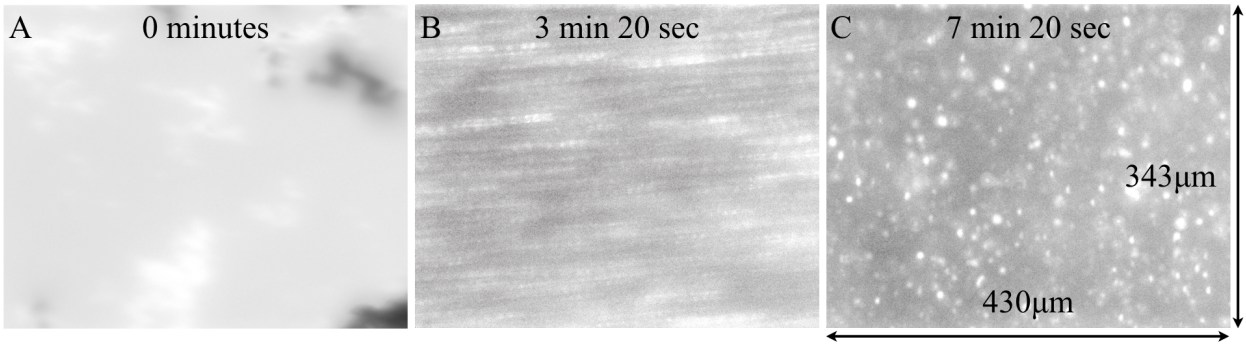

Figure 2.28: Dark field microscopy images of lipid cluster transport outside of the area of deposition. All panels are 430 by 343 μm and focused $\sim$ 60 μm beneath the surface. A shows out-of-focus chromium dioxide needles before the nebulizer is turned on. B occurs during deposition and shows lipid clusters (as well as chromium dioxide needles) moving across the field of view beneath the surface at $\sim$ 0.05 cm/s. By 7 min: 20 sec, shown in C, subsurface lipid clusters are still evident, but lateral flow has ceased.

region outside of the area of direct deposition and just below the surface, we observe that these clusters are transported beneath the surface by the induced Marangoni flow. They travel outward from the area of deposition in the same manner as the indicator bead does at the surface. The bright spots that are in focus are on the order of 10 μm. These bright spots are so close to the size of individual aerosol drops that they most likely result from the deposition of single droplets (where droplet volume-weighted median diameter is 5.7 $\pm$ 0.1 μm).

We note that clusters of lipid can be seen moving beneath the surface soon after the onset of aerosol deposition and typically on the order of a minute before the onset of indicator bead motion. During this interval, subsurface fluid velocity is seen to increase to a value of $\sim$ 0.05 cm/s found by tracking the position of clusters in consecutive video frames. As expected for subsurface flow, this is slightly smaller than the $\sim$ 0.2 cm/s surface bead velocities (assumed to track surface fluid velocity) described above. The delay in onset of surface bead motion relative to the subsurface flow suggests that the indicator beads ($\sim$ 1 mm) have more momentum and take longer to equilibrate to the velocity of the surrounding fluid than do

the small subsurface clusters ($\sim$ 10 μm).

Subsurface transport experiments were also conducted on a PA solution subphase with slightly different results than on water. On water, these clusters are seen to decrease in density smoothly with increasing depth, whereas, on PA, the clusters are seen to be confined within a discrete surface layer. This is likely due to the fact that the liquid aerosol being delivered to the PA surface maintains a miscible interface that keeps the two phases separated at early times. This could prove useful for drug delivery in that we could create a layer on which to spread if spreading conditions were not ideal. For further discussion, see Appendix A.2.

These experiments could not be performed on PGM due to the lack of optical contrast between the opaque PGM and the opaque lipid clusters.

2.6.3 Model for how lipid aerosolization enables Marangoni transport

The combination of these sub-surface images and the ellipsometric data gives a more complete picture of the system. In Figure 2.29, we show a schematic of what we believe to be happening during aerosolized lipid delivery. Lipid dispersions initially contain large, stable MLVs that are not surface active. The nebulization process, being highly energetic and containing high shear flow rates, shears open these MLVs and exposes lipid monomers. These monomers adsorb as a monolayer to the surface of the small, 4 - 6 μm, aerosol droplets produced during nebulization. The aerosol droplets are not large enough to allow re-aggregation of MLVs ($\sim$ 10 μm in diameter), however they are large enough to allow the spontaneous formation of SUVs ($\sim$ 50 - 100 nm) [46]. The formation of SUVs would require significantly less material than contained in the original MLVs, leaving ample excess lipid stored at the aerosol droplet surfaces to form a monolayer. These aerosol droplet surfaces provide energetically favorable

locations for lipid monomer to accumulate, which means that this surface layer is likely densely packed [3].

Deposition of these droplets allows for transfer of the stored monomers to the subphase interface where these monomers then accumulate and locally reduce the subphase surface tension. Ellipsometry indicates a lipid monolayer is at the air-water interface, while subsurface images indicate that the remainder of lipid resides in aggregates beneath the surface.

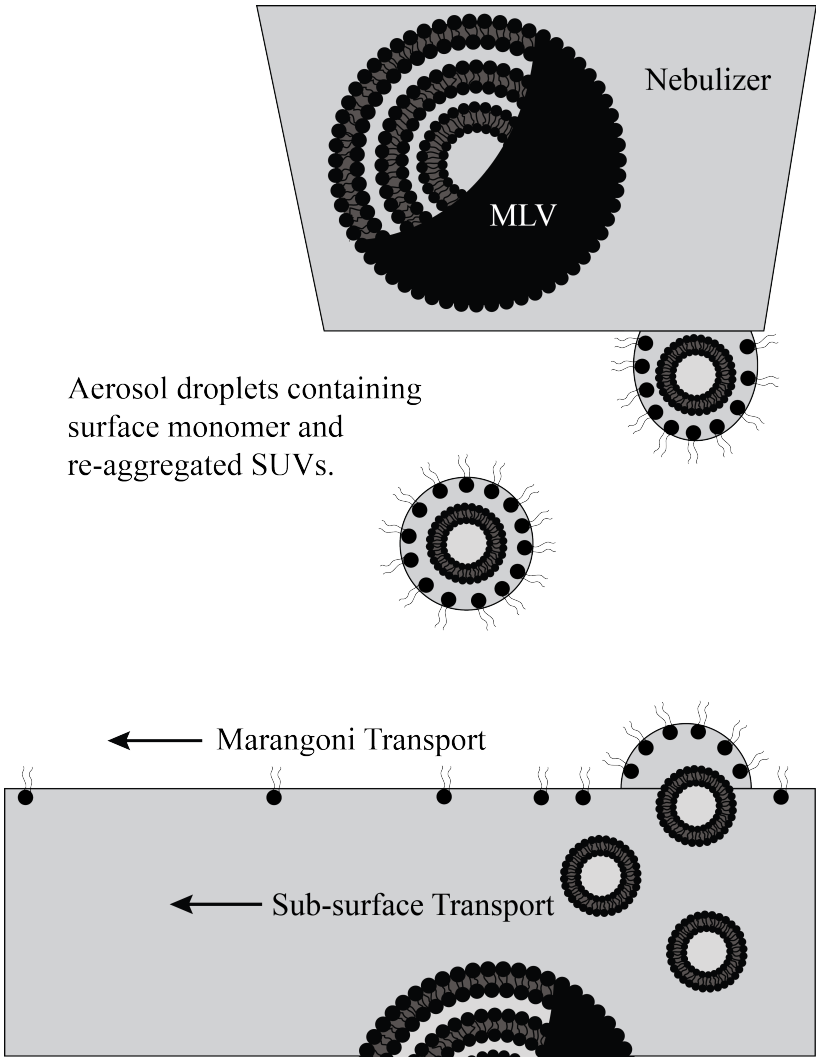

Figure 2.29: Schematic of aerosol delivery. Nebulization disrupts vesicles and stores monomeric lipid as an adsorbed layer on droplets. These droplets deliver monomeric lipid to the subphase surface and re-aggregated lipid to the subphase bulk. The lipid monomer on the subphase surface induces Marangoni transport.

2.7 Observations of Ultra Low Surface Tensions

2.7.1 Low surface tension results from DMPC and DPPC

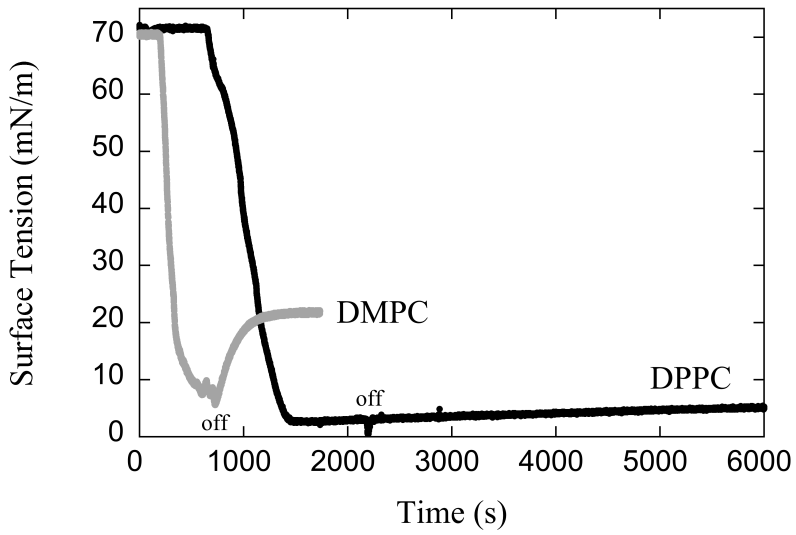

Figure 2.30: Representative low surface tension results for 10 mg/mL DPPC and DMPC MLV dispersions aerosolized via AeroNeb vibrating mesh nebulizer onto DI water. Both lipids are able to reach very low surface tensions (< 10 mN/m). In these trials, the vibrating mesh nebulizer was turned on at 60 seconds and turned off at the label "off". The DPPC monolayer is relatively stable after the nebulizer is turned off, while the DMPC monolayer destabilizes and the surface tension increases to ~ 20 mN/m.

If either the vibrating mesh or jet nebulizer is reloaded multiple times to produce a continuous supply of lipid to dose the surface, rather than delivering a single-reservoir dose, surface tensions as low as 1 mN/m can be achieved (see Figures 2.30 and 2.31). Such low surface tensions have occasionally been measured on Langmuir troughs for pure phospholipids at an air-water interface without monolayer collapse. For example, Lee's work shows DPPC monolayer surface tensions close to 0 mN/m when monolayers are compressed to their tightest possible packing [73]. We made visual observations of the meniscus height on the Wilhelmy

pin in order to be sure that a changing contact angle was not erroneously causing the pin to report a low surface tension. Although the exact contact angle on the pin was not measured, the meniscus was visible and never significantly decreased in height from pre to post lipid deposition during all experiments, including those at low surface tension. Furthermore, to get a sense of the change in contact angle needed for the pin to read 1 mN/m while the actual surface tension was higher, say 10 mN/m, we analyzed the force balance on the pin. In this case, the contact angle would have to be 84°, a nearly flat meniscus. The observed meniscus was much more curved than this.

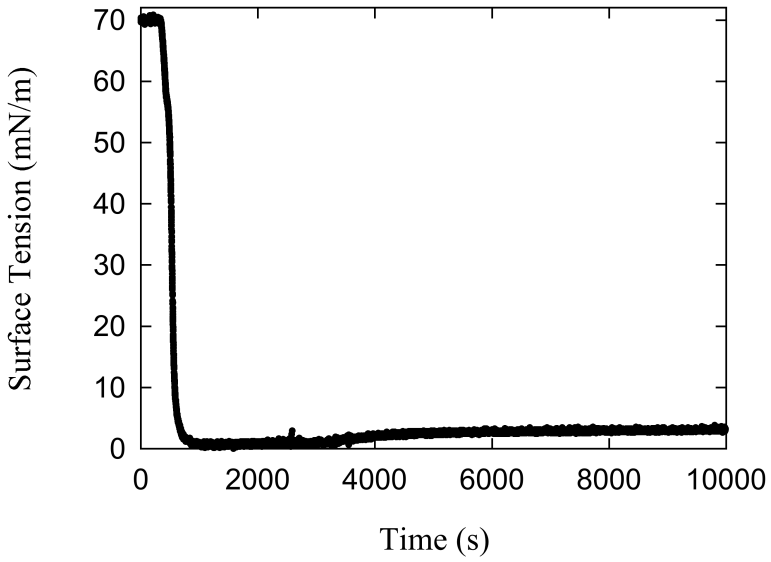

Figure 2.31: Representative low surface tension result for 10 mg/mL DPPC MLV dispersion aerosolized via jet nebulizer onto DI water. The subphase reaches very low surface tensions ($<$ 10 mN/m). In these trials, the jet nebulizer was turned on at 60 seconds and turned off at the slight blip at $\sim$ 2800 s. The DPPC monolayer is relatively stable after the nebulizer is turned off, remaining below 10 mN/m overnight.

In Figure 2.30, we see that both nebulized DMPC and DPPC dispersions are able to reach these low surface tensions when deposited onto water. This is true for both the vibrating

mesh and the jet nebulizers as long as the dispersion supply in the reservoir is sufficiently large.

There are two clear differences between these experiments. First, for these identical experimental conditions, DPPC takes significantly longer to begin to decrease the surface tension of the subphase than does DMPC. This is likely due to the fact that the two bulk lipids are in different phases. At the temperature of these experiments ($\sim 25°C$), bilayer DMPC will be in a fluid phase while bilayer DPPC will be in a more rigid gel phase. It stands to reason that shearing of DPPC MLVs would take more energy to and, thus, longer times (and greater reservoir volumes) for the same amount of lipid monomer to be released. Additionally, the "lift off" area per molecule in the Π/A plot for DPPC is lower than that for DMPC at 25°C. This means a greater amount of total DPPC monomer must be delivered to achieve the same surface tension reduction.

The second difference between these experiments is the fact that the DPPC layer remains at a low surface tension, increasing slowly after the end of aerosolization, but remaining below 10 mN/m even when left overnight. DMPC, on the other hand, recovers to about 20 mN/m within a few minutes after aerosolization is stopped. As we saw in our surface pressure/area per molecule experiments, at room temperature DMPC is above its monolayer critical temperature (it does not have a liquid expanded/liquid condensed phase-coexistence region), while DPPC is below this critical temperature. According to the work of Lee and coworkers, DPPC's greater rigidity and low monomer mobility at a temperature below its critical temperature would allow it to sustain low surface tensions for much longer than it could above the critical temperature [36, 37, 73, 85]. DMPC's more fluid phase in the current experiments conducted slightly above its critical temperature would not allow it to sustain such low surface tensions for as long. It would likely immediately begin losing monomer to the bulk through vesicle nucleation or monolayer folding, which would decrease the monomer density at the surface. Collapse pressures for lipid monolayers depend heavily

on temperature.

However, the temperature dependence of the collapse pressure does not explain why the DMPC layers dip to very low surface tensions but then recover. Langmuir trough studies suggest there is a competition between the rate at which lipid is being compressed on the surface and the rate at which material is being lost to the subphase [73]. This loss can occur in a number of forms, including nucleation of vesicles or shearing or folding of the monolayer. Even if part of the monolayer is being lost to the bulk, by continually feeding the monolayer with monomeric lipids from the aerosol, we are compressing it outside the region of direct aerosol deposition where the surface tension is measured. As it is being continuously fed, we hypothesize that the DMPC monolayer may be able to sustain a higher surface pressure state than it generally would at this temperature. Once the nebulizer is turned off and the layer is no longer being fed new monomer, the rate of monomer loss to the bulk will be dominant and the surface tension will recover.

2.7.2 Low surface tension results from other, soluble surfactants

The ability of aerosolization of surfactant formulations to create surface layers that are lower surface tension than their initial formulations is not limited to insoluble phospholipid surfactants. Similar results have been seen with both aqueous CTAB and aqueous tyloxapol, both soluble surfactants. Both aqueous CTAB and aqueous tyloxapol solutions induce immediate surface transport on water when delivered as either microliter drops or as an aerosol. However, in these experiments, the surface tensions achieved by aerosolizing solutions of these surfactants onto a water subphase are lower than the surface tensions of the prepared aqueous surfactant solutions at concentrations above their CMCs.

Figure 2.32 shows experiments delivering a 4mg/mL (13 mM) aqueous tyloxapol solution to a DI water subphse (this is well above tyloxapol's CMC of 0.018 mM). When the solution

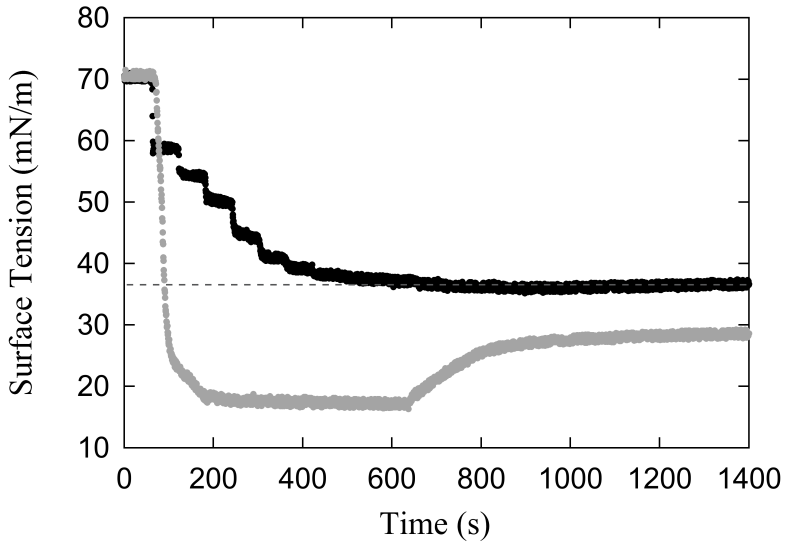

Figure 2.32: Example trial showing surface tensions for 4 mg/mL tyloxapol deposited onto water dropwise (black) and via vibrating mesh nebulizer (gray). The black data shows the surface tension as 1μL per minute of tyloxapol solution is deposited for 20 minutes. The gray data shows the surface tension as the tyloxapol solution is aerosolized onto the surface. Deposition begins at 60 seconds and the nebulizer runs out around 620 seconds. The gray dashed line represents the surface tension of the 4 mg/mL tyloxapol solution, 37 mN/m.

is deposited by pipetting 1μL drops onto a water subphase every minute for 20 minutes, the subphase concentration will be approximately the CMC of tyloxapol at the end of the experiment. The resulting surface tension of the water decreases with each successive drop until it levels off at approximately 37 mN/m, which is the surface tension of the tyloxapol solution. However, when tyloxapol is aerosolized (via an AeroNeb vibrating mesh nebulizer) onto a water subphase, the surface tension quickly drops to $\sim$ 19 mN/m, far below the surface tension of the original solution, and remains there until aerosolization is complete. It then recovers, but only to $\sim$ 29 mN/m, which is still below the surface tension achievable if the surface layer is in equilibrium with the bulk subphase. This behavior is similar to the behavior of aerosolized DMPC or DPPC dispersions onto water. It seems, therefore, that

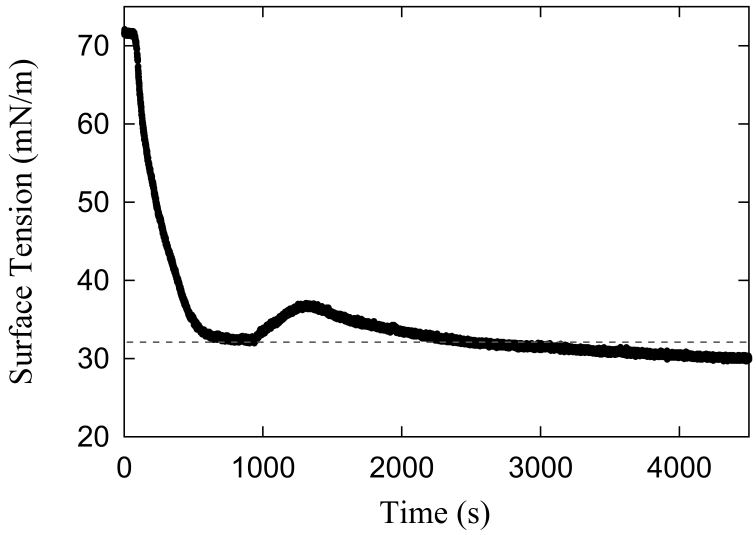

Figure 2.33: Example trial showing surface tensions for 5 mM CTAB aerosolized onto DI water via vibrating mesh nebulizer. Aerosolization begins at 60 seconds and the nebulizer runs out at 1000 seconds. The gray dashed line represents the surface tension of the 5 mM CTAB solution, 32 mN/m. This result was repeated three times.

the surface structures achievable through aerosolization in this case cannot be in equilibrium with the subphase.

When a 5 mM aqueous solution of CTAB (again, above CTAB's $\sim$ 1 mM CMC) is delivered by aerosolization onto a water subphase, even more complicated behavior is observed (see Figure 2.33). When the nebulizer is turned on, the surface tension of the water subphase drops to around 32 mN/m, which is the surface tension of the pure CTAB solution. However, when the nebulizer turns off, the surface tension begins to recover upward, but then turns back downward and ends up dipping below the surface tension of the 5 mM CTAB solution.

We have not fully investigated how these low surface tension layers are being formed by aerosol deposition. It could be that depositing micron-sized droplets of surfactant solution to an interface allows the interface to access physical states that are not accessible simply

by surfactant adsorption from the bulk. Further study would be very interesting here. Ellipsometry, brewster angle microscopy, or another form of surface scan might be able to reveal the surface structures behind these low surface tension states.

2.8 Phospholipid-induced transport of drugs on lung-mimic surfaces

In this section, we examine whether the transport induced by aerosolized lipid can transport the types of antibiotics that are used in the treatment of lung infections. One such drug is tobramycin. We found that tobramycin may be transported by aerosolized deposition of DPPC onto a PGM subphase even with the presence of a pre-deposited DPPC monolayer. This was expected from previous work showing that aerosolized DPPC dispersions can initiate Marangoni spreading on PGM and that this spreading continues to occur with continued deposition even once a lipid layer has been formed.

As described in the methods section, experiments were first conducted aerosolizing DPPC dispersions onto PGM and observing the Marangoni transport. Tobramycin was then added to the DPPC dispersion and a second set of aerosolization experiments onto PGM were conducted. Finally, a third set of experiments were conducted where a pre-deposited monolayer of DPPC was added to the PGM surface prior to aerosolization in order to mimic the preexisting lipid layer in the lung. These experiments were conducted in collaboration with fellow graduate student Steven Iasella. Marangoni transport was observed in all cases and described in detail below.

2.8.1 Transport of tobramycin with and without a pre-deposited lipid layer

Figure 2.34A shows the results of the simultaneous measurement of surface tension and tracer particle motion during delivery of aerosolized DPPC dispersions onto a PGM solution surface with no pre-deposited lipid monolayer. The surface tension immediately decreases and the bead begins to move as soon as aerosolization begins, indicated as 0 seconds on the

time axis. This is consistent with the shape of the DPPC Π/A isotherm on PGM solution: even small changes in surface area per molecule decrease surface tension in the region of direct deposition relative to the lipid-free PGM solution surface external to that region. The tracer particle moves most of the way across the trough before eventually sinking into the subphase due to the low surface tension. The surface tension reaches a minimum of ~ 5 mN/m.

Figure 2.34B shows the simultaneous measurement of surface tension and tracer particle motion during DPPC aerosolization onto a PGM solution surface with a pre-deposited DPPC monolayer. Negative times in the figure represent times before the aerosolization begins (showing the chloroform evaporating from the DPPC deposition solution and the DPPC monolayer equilibrating). The monolayer equilibrates at ~ 24 mN/m [61]. The tracer particles begin to move as aerosolization commences and the surface tension drops. The beads do not always reach the end of the trough. Often they sink before reaching the end due to the low surface tension that develops as DPPC moves across the surface. They do not always reach the end of the trough even when they do not sink. This could be due to the lower surface tension due to the pre-deposited layer, causing the bead to initially sit lower in the mucin and experience larger drag forces [98]. Another possibility is that the DPPC monolayer reaches complete compression and collapses before the bead has fully traversed the trough. The minimum surface tension achieved is consistently lower for experiments when DPPC was pre-deposited on the surface. Because the same amount of DPPC was delivered via aerosol in both experiments, this difference in minimum surface tension is likely due to the fact that there was simply more total DPPC present at the interface in experiments with pre-deposited layers.

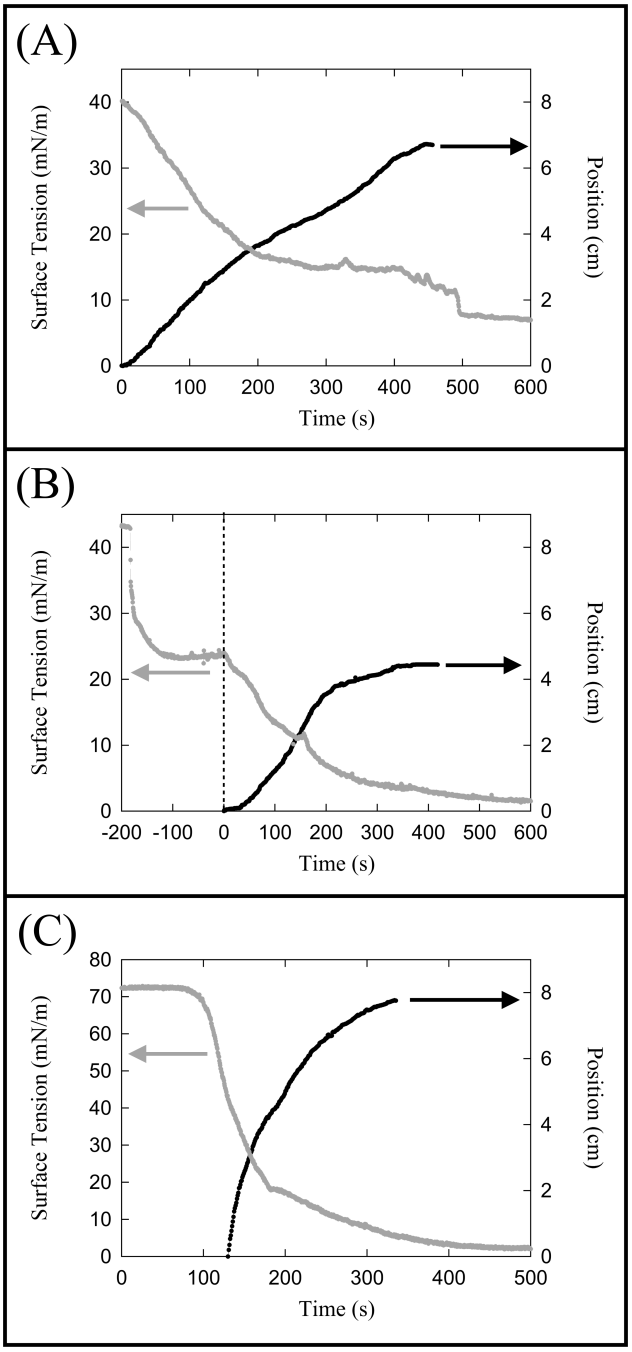

Figure 2.34: Surface tension and movement of a tracer bead during representative DPPC spreading experiments, (A) without pre-deposited lipid on PGM solution, (B) with pre-deposited lipid on PGM solution, and (C) without pre-deposited lipid on water. The grey line is the surface tension and the black line is the bead position with 0 cm being at the edge of the aerosolization chamber. Nebulization begins at zero seconds. In (A) the abrupt surface tension dip at about 500 s is a reproducible but as yet unexplained phenomenon. Negative times in (B) represent times before aerosolization begins, when the DPPC is being deposited onto the subphase.

For both cases with and without a pre-deposited DPPC layer, the surface tension decreases to below 10 mN/m by the time aerosolization stops. According to Figure 2.13, the DPPC delivered by aerosol is achieving a surface tension significantly lower than that which can be obtained by delivery of a chloroform DPPC solution onto the subphase via pipette. This is expected and agrees well with the ultra-low surface tension results seen previously (see Figure 2.30 and surrounding discussion). Because the aerosolized lipid achieves lower surface tensions than the pre-deposited layer, there is still a gradient in surface tension across the PGM solution surface and Marangoni stresses are induced.

2.8.2 Detection of transported tobyramycin

The assays in this subsection were conducted by fellow graduate student Steven Iasella.

Because there is a direct assay for tobramycin, mass and volume measurements for aerosol deposition are possible in this case. We assume, since tobramycin is soluble in water, that the concentration loaded in the nebulization chamber is the same as the concentration in the aerosol. Table 2.1 shows the average tobramycin dose, deposition time, and aerosol volumetric deposition flux for each of the experimental conditions. Only a very small fraction of the 240 mg of tobramycin in the formulation charged to the nebulizer was deposited onto the trough. The vast majority deposited elsewhere in the aerosolization chamber or was removed by the suction applied to the chamber. The calculated average aerosol deposition fluxes for all experiments were well within the "low flux regime" as defined in a previous publication from our group [100]. Droplet coalescence is not expected in this regime. Instead, post-deposition dispersal of a field of distinct droplets is expected. During a typical nebulizer treatment, low flux deposition would be anticipated in airway generations 7 and beyond [58]. A one-way ANOVA test shows statistically similar ($p < 0.05$) doses were delivered to the

trough both with and without DPPC in the aerosol formulations, so the resulting spreading data should be comparable for all conditions.

Table 2.1: Average dose, deposition time, and volumetric deposition flux in aerosol deposition experiments. Standard error is given in the table (n = 3).

	Tobramycin Dose (mg)	**Deposition Time (s)**	**Volumetric Flux (nL cm^{2}s)**
Tobramycin	0.63 ± 0.12	789 ± 69	1.32 ± 0.13
Tobraymcin/DPPC	0.50 ± 0.09	447 ± 8	1.88 ± 0.18
Tobramycin/DPPC Pre-deposited DPPC layer	0.51 ± 0.07	469 ± 18	1.81 ± 0.12

Figure 2.35 shows the concentration profiles determined for tobramycin outside of the aerosolization chamber (recalling that tobramycin outside of the chamber must have gotten there due to Marangoni transport). Each data point represents the mean of three trials and the error bars show the standard error. The surface-sample concentrations were normalized by the total concentration of tobramycin in the bulk of the subphase (after thorough mixing at the end of each trial, as described in the methods). The bulk concentration was approximately 7 μg/mL. When no DPPC was present in the aerosol, no tobramycin was detected on the trough outside the region of direct deposition. This indicates that (a) the precautions taken to prevent aerosol deposition onto the trough outside the aerosolization chamber were sufficient (see methods section) and (b) when no lipid was present in the aerosol formulation, no tobramycin transport occurred. Although we cannot assay for lipid on the surface, since the size distribution and density of the aerosol droplets, and, thus the Stokes numbers, are similar for all formulations, we expect that the spatial deposition behavior of all the aerosols to be the same.

As shown in Figure 2.35, in the cases where DPPC was present in the aerosol, the concentration of tobramycin was detectable across the full length of the trough. This spreading

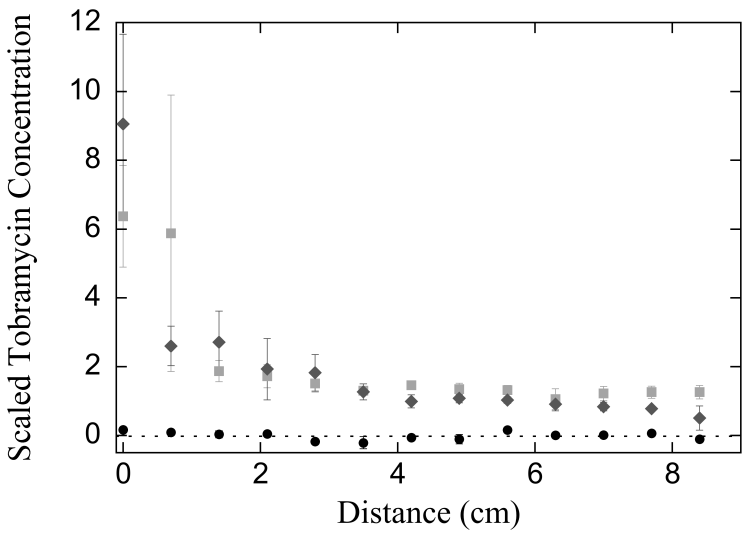

Figure 2.35: The tobramycin concentration on the subphase surface in the region outside the aerosolization chamber determined after complete nebulization of the contents of the reservoir. When no DPPC is present in the aerosol (black circles), no tobramycin escapes the aerosolization chamber. When DPPC is added to the aerosol, spreading occurs and tobramycin can be detected all the way across the trough (light gray squares). Spreading is similar when a DPPC monolayer is deposited on the subphase prior to delivery of the DPPC/tobramycin aerosol (dark gray diamonds). The error bars show the standard error of three trials (n = 3). The concentration is normalized by the total deposited dose for a given run. A scaled concentration of 1 corresponds to a tobramycin concentration of approximately 7 μg/mL, though it varies slightly for each trial. Average scaled tobramycin concentrations sampled inside the region of deposition were $\pm$ 5 for all trials.

of the tobramycin was accompanied by movement of a tracer particle across the surface. The outside portion of the trough is 8.5 centimeters long, suggesting that aerosolized lipid can transport materials several airway generations deeper into the lung from the point of aerosol deposition [116]. The average concentration of tobramycin across the trough outside the deposition region is $\sim$ 10 μg/mL when DPPC is present in the aerosol formulation regardless of the presence of a pre-deposited DPPC layer on the subphase.

The surface-sampled concentrations of tobramycin were similar with or without a pre-

deposited DPPC monolayer. At the very end of the trough, there was a small but reproducible decrease in tobramycin concentration for the trials with a pre-deposited monolayer of DPPC. This could be due to the pre-deposited DPPC layer acting like a "piston oil"; the DPPC monolayer compressed against the end wall of the trough could be stopping further surface transport of the lipid. While this layer could shut down flow on the surface, the tobramycin, being a hydrophilic molecule soluble in the subphase, may continue to be transported by induced subsurface flows. It is important to note that the end of the trough is an artificial limitation of our apparatus. In vivo, we would expect that the endogenous lipid would simply be pushed deeper into the lung.

2.8.3 Surface tension recovery

We observe that after 5-10 hours elapse, the surface tension of PGM recovers to around 27 mN/m as DPPC apparently desorbs from the surface into the bulk. This surface tension recovery happens only after the aerosol stops and is slow compared to the timescale of the experiment. The desorption process observed at the end of these experiments should be active during deposition but the rate of adsorption during nebulization is significantly higher than the desorption rate, meaning that the difference in these rates may be what allows for the formation of transient, ultra-low surface tensions. This gives some insight into how long exogenous surfactant will be present on the surface in the lungs, and how much time must elapse between treatments. After 5 - 10 hours (or less, as mucociliary clearance may speed up this process), the lung surface will likely recover to pre-treatment surface tensions. At this point, treatment could begin again with similar expected results.

Note here that this is a different result from that of DPPC aerosolized onto water (see Figure 2.30). On water, the ultra-low surface tensions achieved via DPPC deposition recover only 5 - 10 mN/m over a 24 hour period. The instability of these layers on PGM as compared

to water likely has to do with the hydrophobic moieties within the PGM. The DPPC may more readily desorb or nucleate off of the air-PGM interface to form complexes with the mucins, where there is no such drive in pure water.

2.8.4 Effect of isotherm shape on transport lag time

To demonstrate the impact of the shape of the isotherm on transport, a DPPC dispersion was directly aerosolized onto a DI water surface; results are shown in Figure 2.34C. This experiment also results in achievement of an ultra-low surface tension ($\sim$ 1 mN/m), however it has a longer lag time before the surface tension drops. There is a $\sim$ 80 second delay between the nebulizer being turned on and any measurable decrease in surface tension and correlated bead movement. This is consistent with the initial slopes of isotherms for DPPC on pure water. Without a pre-deposited DPPC layer, the lipid layer must build up on the surface in the gaseous phase for some time before reaching the liquid expanded state where a sufficiently dense monolayer can significantly decrease surface tension. This lag time was not observed on the PGM solution suphase, with or without a pre-deposited DPPC layer, because the Π/A isotherm shows a significant decrease in surface tension at large areas per DPPC molecule that would have corresponded to the gas phase on a simple water subphase.

Note that this lag time behavior is correlated with that seen in Section 2.5.1 where lower concentrations of lipid dispersions had longer lag times before surface tension reduction. In that case, the lower concentration of lipid resulted in a slower climbing of the isotherm, which resulted in a lag. In general, it is clear that the surface tension reduction in these experiments correlates with traversing the isotherms in that lipid deposition gradually decreases the area per molecule on the surface and, thus, increases the surface pressure in a manner dictated by the isotherm. This may not be identically due to the fact that the method of deposition likely does not create a true thermodynamic isotherm.

2.9 Transport using Natural Lung Surfactant

Bovine and porcine natural lung surfactants (also used in formulations for Surfactant Replacement Therapies, SRTs) have been used in the treatment of various lung ailments, from infant respiratory distress syndrome to advanced lung infections (for example, see [1, 39]). These surfactants contain a number of components including phospholipids (primarily DPPC and POPG) and peptides. In most cases, these SRTs are delivered via bolus delivery into the lung, however some work has been done to deliver them via aerosolization [5]. If they were delivered via aerosol, they would have the potential for the same transport seen with our phospholipid aerosols. In fact, we have shown that these natural lung surfactants show the same behavior as our phospholipid aerosols in that they do not induce transport when they are delivered as microliter drops onto a PGM surface, but do induce significant transport when aerosolized. This suggests that the mechanism for transport in this case could be similar to that of pure phospholipids. The vesicles of DPPC and other phospholipids contained in the SRTs may be sheared open by the aerosolization process, stored on aerosol drops, and then delivered to the ASL.

2.9.1 Microliter drop deposition

Microliter drops of two different SRT formulations (Curosurf and Infasurf) were delivered onto two different subphases (PA and PGM solutions). Experiments were conducted at room temperature $\sim 25°$C. We observed that both SRT formulations induced spreading on the PA solution, but did not induce spreading on the PGM solution.

When a 2μL drop of Curosurf or Infasurf is delivered onto PA solution, the surface tension of the subphase drops from the ~ 69 mN/m of PA to between 25 and 30 mN/m. This drop is accompanied by motion of tracer beads across the interface outward from the region of deposition.

This is a slightly different result from that seen for pure phospholipids. Dispersions of pure DMPC and DPPC do not induce spreading on either PA or PGM solutions. We believe this to be due to the stability of these phospholipid vesicles in dispersion and to the very slow rate of break-up of these vesicles at the air-liquid interface (see the introduction to this chapter). In the case of SRT formulations, there are additional natural components (peptides, salts, etc.) that may cause vesicles to be less stable, allowing them to break more easily at the air-liquid interface and release surface-active monomers. This allows for transport on the PA surface.

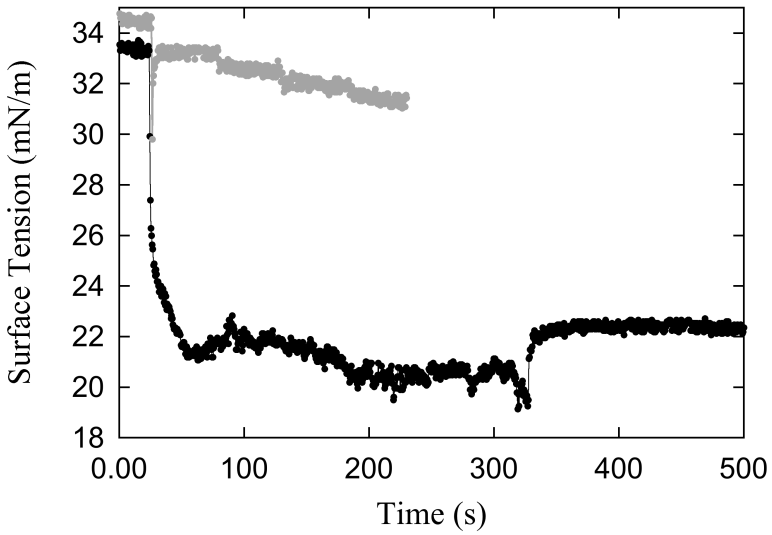

Figure 2.36: Aerosolization (black) and dropwise deposition (gray) of Infasurf onto a 5% PGM subphase at 25°C. The nebulizer is turned on at 25 seconds and runs out at 320 seconds. The first 2 μL drop is placed at 25 s and then three more 2 μL drops were placed, each one minute apart.

When a 2μL drop of either SRT formulation is delivered onto PGM solution, the surface tension of the PGM takes a very slight dip from its initial 33 - 37 mN/m value, but returns almost immediately to a value near the starting surface tension of the PGM (see Figure

2.36). The tracer particle at this moment is seen to "shiver", but no significant motion is seen. The surface tension then gradually drifts downward at a rate of approximately 1 mN/m per minute for the first 10 minutes, as is commonly seen for PGM. The surface tension after a number of minutes approaches 30 mN/m, but there is no observed transport of surface tracer particles.

There are two possible explanations for this lack of spreading on the PGM solution. First, the surface tensions achieved by breaking vesicles at the surface (which will be the surface tension of the SRT formulation itself) may still be higher than the initial surface tension of the PGM solution. Second, there may be a slower rate of vesicle break-up at the PGM interface than is true for PA. The PGM surface tension already drifts downwards, as is common of many polymeric subphases, so the rate of vesicle break-up may not be fast enough to lower the PGM subphase surface tension and induce spreading.

2.9.2 Aerosol deposition

We had limited quantities of these SRTs, so aerosolization experiments were not extensive. When Infasurf is loaded into the AeroNeb vibrating mesh nebulizer and delivered directly to a PGM surface at $\sim 25°C$, significant surface tension reduction and particle motion are observed (see Figure 2.36). The surface tension decreases to $\sim$ 20 mN/m over the course of less than 10 seconds and particle motion is seen almost immediately. Once nebulization has ended, the surface tension recovers slightly to 21-23 mN/m.

This result is quite similar to the result of aerosolizing pure phospholipid dispersions onto PGM where the aerosolized lipid was able to reduce the surface tension of the PGM subphase when droplets of lipid dispersions were not. This suggests that the mechanism behind SRT spreading may be the same as that of pure phospholipid and that the phospholipids may be the primary transport agents in these formulations at this temperature. It also suggests that

there is reason to expect these SRTs to achieve ultra-low surface tensions if nebulization is maintained.

Note that the temperature in the lung is higher than in these experiments. The ability of these formulations to induce transport may be highly dependent on the phase of the lipids and polymers included within them (even though this did not appear to be the case for pure phospholipid dispersions). In previous work by Amy Marcinkowski [77], Infasurf was seen to induce spreading on human bronchial epithelial cells at body temperature (37°C) wether it was deposited by microliter drop or by aerosolization.

Developing an understanding of the potential use of these SRT formulations in Marangoni transport, as well as understanding the mechanism behind this transport, is essential for future work involving delivery of SRTs to the ASL of the lung (as described in Section 1.1). The efficacy of SRT formulations as a surface tension-reducing agent will depend on the method of delivery. Additionally, isolating the components of SRT formulations that are responsible for this surface tension reduction could allow for more precise formulation of effective treatments.

2.10 Conclusions

We have shown that when lipid dispersions are aerosolized onto an air-aqueous interface, they produce Marangoni flow, whereas macroscopic droplets of the same dispersions do not. Lipid dispersions do not contain enough accessible surface-active material to initiate detectable Marangoni flow because the lipid is sequestered within non-surface-active multilamellar vesicles. We propose that nebulization acts both to shear open vesicles and to create a high surface area on which to store a lipid monolayer until it is deposited and transferred onto the subphase surface. Nebulization of the lipid dispersion and direct deposition of the resulting aerosol are both required for significant Marangoni flow. If the aerosol droplets are allowed to recombine in a bulk medium, the broken lipid structures quickly re-aggregate, leaving a bulk dispersion incapable of producing Marangoni stresses.

When the aerosol droplets land on the subphase, they transfer their stored lipid monolayer directly onto the surface. They also deliver the non-surface-active re-aggregated lipid SUVs to the bulk. Being non-surface-active, these aggregates diffuse from the surface region deeper into the (initially lipid-free) bulk, appearing within a thin region on the order of hundreds of micrometers from the surface on the time scale of these experiments. In contrast with what has been shown for bulk dispersions, these clusters evidently are not adsorbed onto or otherwise associated with the lipid monolayer. If there were aggregates attached to the surface, as Kim and coworkers observed in their work with bulk dispersions of pure lipid vesicles [62], ellipsometry would have revealed a thicker surface layer rather than the observed monolayer. With prolonged deposition, the packing of this monolayer increases until it creates a surface tension gradient between the deposition region and the remote surface, which induces Marangoni flow at the interface and subsequent subsurface flow within the bulk.

The ultra-low surface tensions achievable by lipid dispersions allow them to induce

Marangoni flow on subphases, such as PGM, that are lower surface tension than many common soluble surfactants. Use of this mechanism to enhance the distribution of aerosolized medication in pulmonary drug delivery depends not only on the ability to drive Marangoni flow on complex lung airway surface liquids with variable surface tensions, but also on their safety in the lung. As natural components of the pulmonary surfactant that is abundant in the respiratory zone of the lung, phospholipids are good candidates for enhanced pulmonary drug delivery in the bronchi and bronchioles. This work has shown that phospholipids can function as Marangoni spreading agents, provided they are administered via aerosol deposition, without the need for any other excipients.

The ability to induce Marangoni flow on very low surface tension surfaces is essential if we wish to apply this work to therapeutic applications in the lung, either for enhanced drug delivery using self-dispersing aerosolized carriers or for delivery of SRT formulations. Although the surface tension, and its spatial variation, in the lung is still debated in the literature [2, 49, 93, 95], the fact that surface tensions as low as 1 mN/m can be achieved using aerosolized lipid dispersions indicates that these dispersions will spread well in the lung. In addition, the fact that we consistently observe convection beneath the surface suggests that any drug that one may disperse with (or encapsulate in) lipid vesicles will be transported by convection over large distances after deposition. This would allow the delivery of aerosolized lipid dispersions to aid in transport of non-surface-active medication to the lung.

When tobramycin was added to the aerosolized phospholipid dispersions at concentrations similar to those currently used in medical treatment, antibiotic concentrations of over 8 μg/mL are found across the PGM solution surface as far as 8.5 cm away from the region of deposition. For reference the Minimum Inhibitory Concentration (MIC90) of tobramycin for *Pseudomonas aeruginosa*, a common CF-associated pathogen, is 8 μg/mL [101], meaning this method of treatment would likely be effective against this pathogen. No spreading

is seen from the control experiment of a tobramycin aerosol delivered onto the substrate without DPPC. These results suggest that administering aerosolized solutions of DPPC and tobramycin will transport the antibiotic across biologically relevant length scales in the lung.

Tobramycin transport is little affected by the presence of pre-deposited lipid. There is some evidence that the pre-deposited layer is compressed by the newly deposited lipid forced onto the surface by the aerosolized dispersion, but this compression is an extrinsic effect due to the finite area of our mucin surface and has very little effect on spreading of the tobramycin. Preexisting lipid is unlikely to inhibit the effectiveness of the lipid transport of the tobramycin.

Chapter 3

Evolution and Disappearance of Solvent Drops on Miscible Polymer Subphases

3.1 Introduction

Much of the work in this chapter will be published in the following manuscript:

Disjoining Pressure Dominated Drop Shape Evolution of Solvent Drops in Miscible Polymer Solutions. **A.Z. Stetten**, B.W. Treece, T.E. Corcoran, S. Garoff, T.M. Przybycien, and R.D. Tilton. *Journal of Colloid and Interface Science.* (In Final Preparation)

The work in this chapter was a collaboration between myself and fellow graduate student Bradley Treece. I carried out all experimental work. Bradley developed the numerical methods for solving the augmented Young-Laplace Equation.

Generally, when one measures the interfacial tension between fluids, these fluids are immiscible. The definition of interfacial tension involves a minimization of the free energy of the system including the interface, which requires that interface to be in thermodynamic equilibrium. However, there are many cases in which two miscible fluids will maintain a distinct interface for long times when they are not in equilibrium, despite the fact that they will eventually become a homogeneous mixture. The most familiar example of this, perhaps, is honey being poured into tea. The honey maintains a rounded drop shape due to its interfacial tension with the water, but then gradually dissolves into solution. This phenomenon is described in the literature as an "effective interface" with an "effective interfacial tension (EIT)" (first proposed in [67], with many references since). The interfacial thickness and interfacial tension associated with this effective interface are controlled by the diffusive mixing of the two phases.

The theory behind these "effective interfaces" relies on the assumption that they are in local equilibrium. So, rather than a full minimization to find the interfacial free energy, the free energy is instead expanded in powers of the concentration gradient to find the effective interfacial free energy. This non-equilibrium theory of miscible interfaces has been developed for both simple and complex miscible fluid interfaces (For references, see: [17, 54, 55, 59, 75, 112, 120]).

A number of research groups have measured the effective interfacial tension between miscible fluids using various techniques. Smith and collaborators made early measurements of effective interfacial tension using a Wilhelmy plate and Kojima and collaborators showed that the toroidal shapes achieved by miscible drops can be best explained with the addition of a small interfacial energy between the miscible fluids [66,102]. A number of groups studied the interfacial tension of drops, bubbles, and plumes of glycerine in water [53,104,105]. May and collaborators measured the EIT using capillary wave relaxation [20, 79], and Pojman and collaborators measured the EIT using spinning drop tensiometry [86]. For a review of

diffuse interface models and techniques for measurement of EITs, see [4].

Truzzolillo and collaborators examined the effective interfaces between colloidal and polymeric systems. They predict a quadratic relation between EIT and polymer concentration for long-chain polymers, an exponential behavior for tight colloidal particles, and something in between for short-chain polymers [113, 114]. Polymer systems were studied by Zoltowski and collaborators using spinning drop tensiometry and were shown to obey the theoretically obtained relationship between their EIT and the concentration difference between bulk fluid and drop [120]. An informative review of experimental miscible interface work between complex phases can be found in Truzzolillo and Cipelletti's paper from 2016 [112].

In the systems we will be studying, a drop of solvent is placed on a miscible complex solution subphase. The drop is wetted by the subphase and sits just beneath the surface with only a thin wetting layer between the drop and the subphase-air interface. When two interfaces are brought close together, there is an interaction free energy per unit area leading to the so-called "disjoining pressure" between the two interfaces, which is a function of the distance between them. Repulsive disjoining pressures between a fluid drop and a more rigid, higher surface tension interface will act to flatten the drop (reduce the drop's curvature near the interface) [18, 110, 118, 119]. This deformation of the drop will occur in the portion of the drop that is within the "interaction zone", where the disjoining pressure is significant. Most observed films showing the effects of disjoining pressure are only a few nanometers thick [48, 91]. The thickest such films in the literature, between near-critical fluids, have been measured on the order of hundreds of nanometers [57, 82], however, Chan and collaborators suggest that the range of the "interaction zone" could be hundreds of microns [18].

Most of the work done examining miscible interfaces has been in two-phase systems where a drop is suspended within the bulk fluid. In our work, we explore miscible interfaces between a dilute polymer solution and its solvent, where the solvent drop is placed at the air-solution

interface. This allows us to observe the three-phase wetting condition of the drop / subphase / air contact line and compare it to an immiscible wetting condition. If the drop has been wetted by the subphase, our setup allows us to examine the pressures on the drop via the drop curvature. Our system is unique in several ways. First, before dissolution, the solvent drops obey immiscible wetting conditions leading to their being fully wetted by the polymer subphase. Second, small gravitational driving forces (a small density difference between drop and subphase) yield a very sensitive probe of the pressures acting on the drop; therefore, we can examine how disjoining pressures affect the upper and lower drop interfaces at very large distances from the air-liquid interface. Third, we may observe the power law spreading, slow evolution, and eventual disappearance of solvent drops as their interfaces diffuse.

3.2 Experimental Materials and Methods

3.2.1 Materials

All water was purified to 18MΩ·cm resistivity, with < 10 ppb total organic carbon (Milli-Q Academic Unit, Millipore Corporation, Billerica, MA). The purified water had a surface tension of 71.5 ± 0.4 mN/m measured using a Wilhelmy pin apparatus (Nima Technology Limited, Coventry, England).

Primary experiments were performed with poly(acrylamide) (PA) of molecular mass 5 - 6 MDa (CAS# 9003-05-08), which was purchased in powder form from Polysciences (Warrington, PA) and used as received. This is the same material used in the previous chapter; methods are repeated here for completeness. Aqueous solutions of 1% w/w PA were prepared in DI water by adding the PA powder in increments of 2 g every 2 - 3 days in a 3/4 full 1 L bottle under nitrogen with continuous gentle mixing on a gyratory shaker (New Brunswick Scientific, Edison, NJ, model G79, speed "4"). After adding the final 2 g of powder, water was added to bring the total volume up to 1 L, and mixing continued for 2 - 3 more days or until the solution was homogeneous, whichever took longer. The observed entanglement concentration is 0.45 wt% [97]. The surface tension of the PA solution after pouring a fresh sample was 70.8 ± 0.5 mN/m (standard error of the mean for three replicates), which typically decreased by ∼ 1 - 2 mN/m over 5 minutes and then leveled off. Dilutions to 0.8 wt%, 0.6 wt%, 0.4 wt%, and 0.2 wt% were created from the original 1% stock.

Secondary experiments were performed with a lower molecular weight of poly(acrylamide). Poly(acrylamide) of molecular mass 600,000 - 1 MDa (CAS# 19901) was purchased as a 10% solution in water form from Polysciences (Warrington, PA) and used as received. Dilutions to 0.8 wt%, 0.6 wt%, 0.4 wt%, and 0.2 wt% were created from the original 1% stock.

Side-view videos were taken using a model K2 DistaMax^{TM} long-distance microscope purchased from Infinity Photo-Optical Company (Boulder, CO). The microscope was out-

fitted with a STD 1.1 x objective and lit from behind using a variable intensity light source with a diffusing plate in front of the aperture.

Top-view videos were taken using a Nikon AZ100 microscope (Nikon Instruments Inc, Melville, NY) equipped with an AZ-Plan Apo 0.5 (NA 0.05/ WD 54 mm) objective. The microscope camera (model DS-QiMc-Nikon) had 0.6 x magnification. Images were captured with NIS-Elements Basic Research software and analyzed using NIS-Elements Advanced Research software, both purchased from Nikon Instruments Inc., Melville, NY.

3.2.2 Methods

For side-view experiments (shown in Figure 3.1), we used a 3 cm glass cube cell (purchased from Hellma Analytics) filled to a depth of approximately 2 cm with polymeric subphase fluid. A pipette was then used to place a 2 μL drop of water atop the subphase at the center of the cell. This was done as gently as possible to avoid adding kinetic energy into the system and perturbing the effective interface between the two materials. The cell was then covered to keep the humidity high and prevent skinning of the polymer subphase. The cell was large enough that the lowest, center region of the interface was nearly flat and the drop could not be detected to rise along the subphase meniscus due to the tilt angle the meniscus makes with the cell wall. During these trials, the microscope was focused at the center of the cell. In Figure 3.1 the meniscus is seen as a dark band at the top of the image above the drop. Water drops were observed on multiple concentrations of 5 MDa PA subphase and their changing shapes were recorded. For a more complete set of stills from these experiments, see Appendix B.1.

Side-view experiments were also conducted depositing the water drop from beneath the interface of the 1% 5 MDa PA using a curved syringe (results shown in Figure 3.2). The volume in this method was inexact due to the fact that the drop's surface tension is too

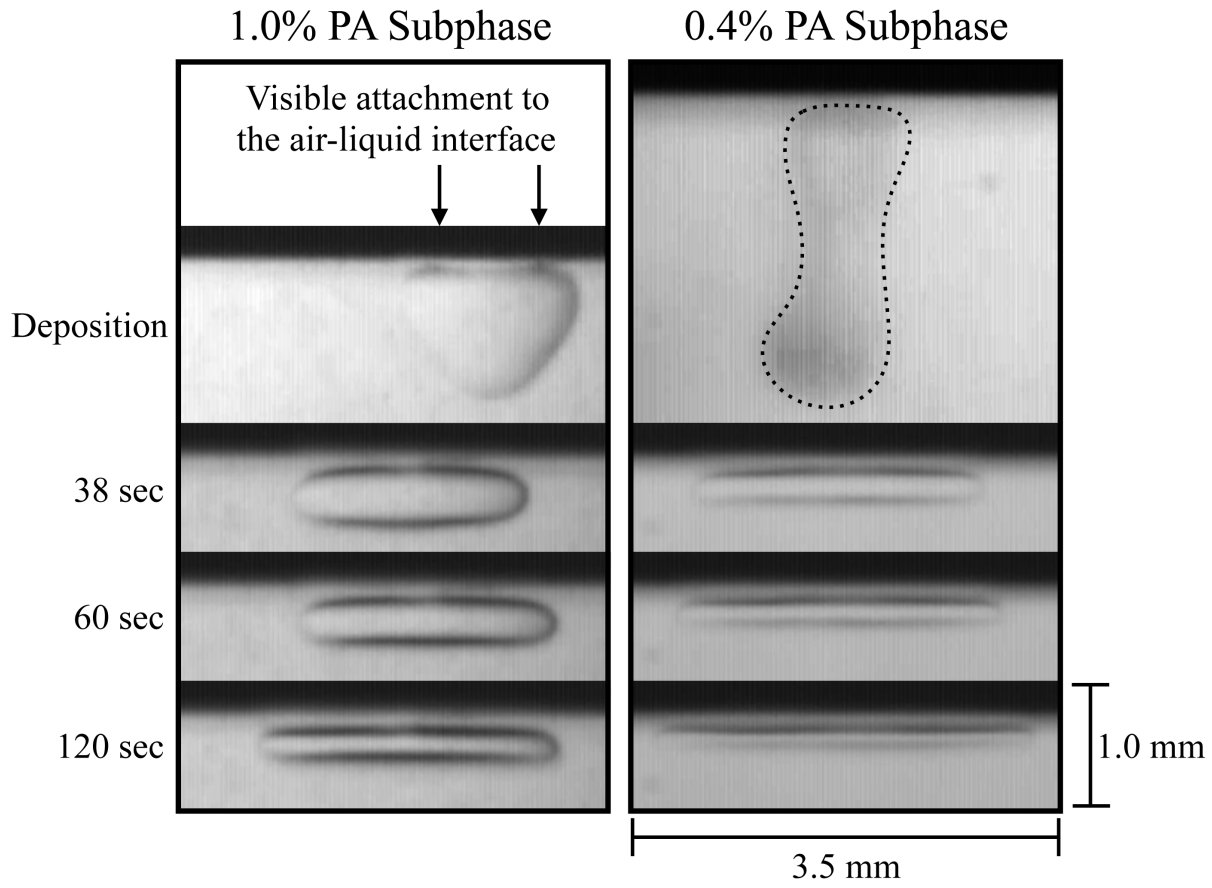

Figure 3.1: Still images from side-view experiments. A 2μL droplet of water was placed atop a 1% or 0.4% 5 MDa PA solution and a wetting layer of PA can be seen to come over top of the drop. The drop gradually changes shape with time as the EIT between the miscible phases decreases. On the higher concentration subphase, the water drops remain rounder and disappear more slowly, giving evidence for a higher EIT.

low to fully pinch off from the syringe (as can be seen by the trail at the bottom of these side-view images). Although the trail attaching the drop to the syringe makes these drops poor candidates for shape examination, it is important to note that, as they rise to the surface of the PA, they form a thin wetting film. The drops never break the air-PA interface and maintain a PA layer that is the same order of magnitude thickness as seen in deposition from above.

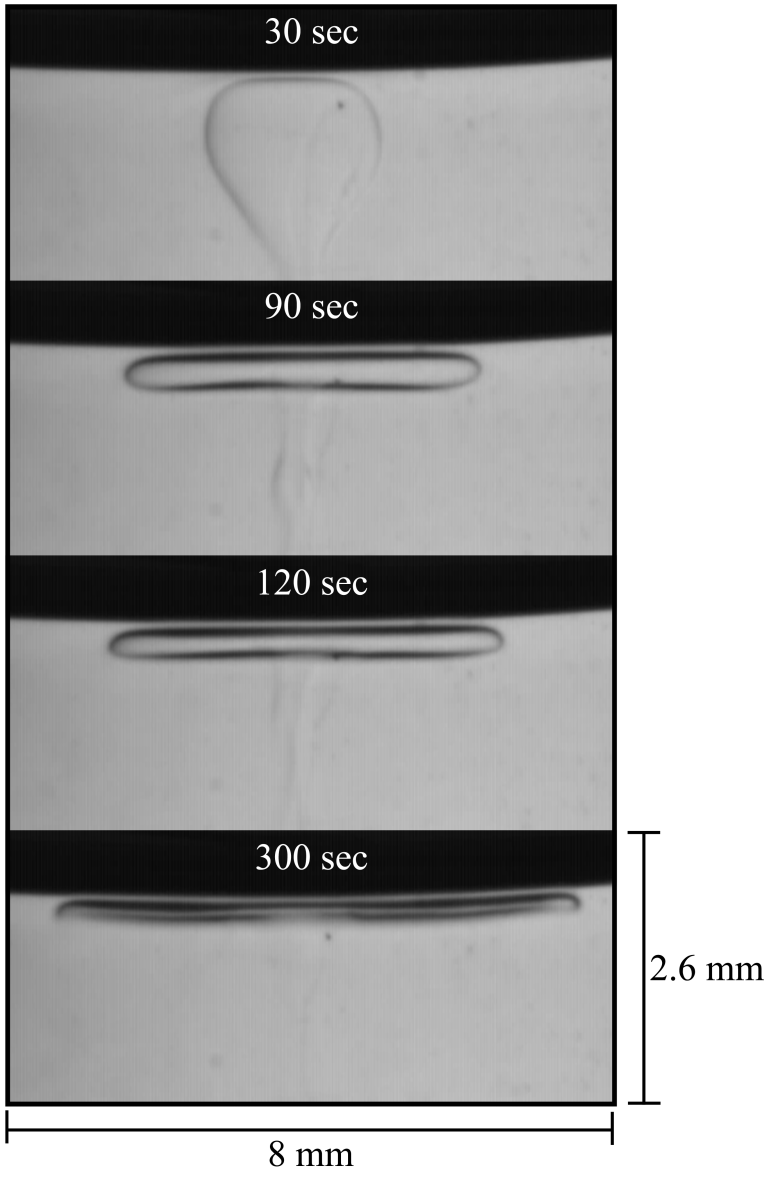

Figure 3.2: Still images from side-view experiments with deposition from beneath the interface. A droplet of water was deposited beneath the surface of a 1% 5 MDa PA solution using a curved syringe. The volume in this method was inexact. The drop rises, but maintains a thin wetting layer of PA between it at the air interface. The drop gradually changes shape with time as the EIT between the miscible phases decreases.

In all experiments, the sample cell was covered to keep a high humidity. If this precaution was not taken, the PA was observed to form a "skin" at the air-PA interface. This could

be observed from the side as a gradually thickening dark band just beneath the band of the meniscus. This band increased in width to ~ 100 μm over the course of an hour. If drops were placed atop this band, they appeared wrinkled rather than smooth as the drops seen in reported experiments here. This type of dehydration of a polymer solution at an air-liquid interface is common and was avoided throughout this thesis work.

For our top-view experiments, we used a 7 cm radius Petri dish. The Petri dish was filled with approximately 1 cm of subphase fluid. Beneath the Petri dish, we placed a black-lined Ronchi ruling slide (Edmund Optics, Barrington, NJ - 150 lines per inch) which enhanced our visualization of the drop (for example, see [15]). A 2 μL drop of water was then pipetted, gently, atop the subphase surface (see Figure 3.3). The Ronchi ruling slide was necessary in these top-view experiments because the drop is so thin in the vertical dimension that it is difficult to visualize relying only on the index gradient through the sample. The dark bands on the Ronchi ruling slide shift slightly due to the curvature along all bounding interfaces and index of refraction change along the optical path through the subphase and drop, thus allowing us to see the edges of the drop more clearly. After videos were taken, a bare image of the Ronchi ruling through the sample (before the drop was deposited) was subtracted from each subsequent image to show the shifted lines at the edges of the drop. This was not needed in the side-view case because the drop is much wider in the horizontal dimension and, thus, visibly displaced the light rays passing through it.

The entire top-view experiment was contained within a humidity-controlled chamber kept above 95% relative humidity. The chamber was constructed such that the Ronchi ruling slide and Petri dish could fit inside and a small hole was left for the probe end of the Sensirion humidity gauge. Humidified air was passed through the chamber using inlet and outlet gaskets. This extent of humidity control was not necessary in the side-view experiments because the small square cells could simply be covered. Covering the top-view experiments after drop deposition resulted in a slight motion of the dish, which made Ronchi ruling

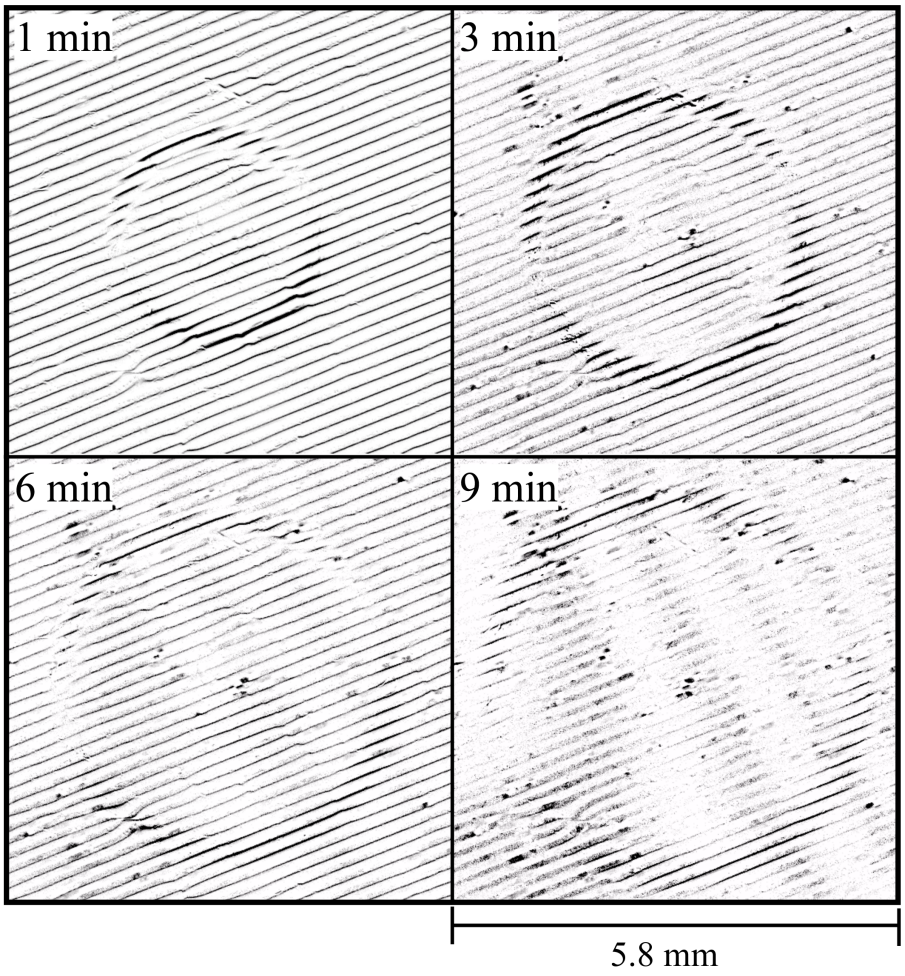

Figure 3.3: Still images from top-view experiments. A 2μL droplet of water is placed atop a 1% 5 MDa PA solution and is visualized using our Ronchi ruling technique.

subtraction impossible.

Water drops were, again, observed on multiple concentrations of PA subphase and their time-evolving radii as well as their final disappearance times were recorded. Disappearance of the drop in either view is a complex problem controlled by a combination of the drop curvature, the decreasing height of the drop, the broadening of the diffuse boundary between the drop and subphase, and the decreasing index of refraction difference between the drop and the subphase. Thus, the "disappearance time" depends on the particular optics used, so

care was taken to make sure the optics were consistent from one experiment to the next. In addition to consistent optics, we also used consistent image contrast enhancement to increase visibility of the shifted Ronchi ruling lines.

A number of image detection methods were tried in order to automate the process of determining a "disappearance time", however, they were each confirmed to be less sensitive than the human eye. These other methods included intensity scans (both linear and summed radial) of the drop as well as examining the Fourier transform of the images. The most successful automated method for determining disappearance time was achieved by taking the 2D Fourier transform of the image, which looks like a series of evenly spaced bright spots representing the wavelength modes between Ronchi ruling lines. These bright spots will be very sharp in the case of an image of the Ronchi ruling slide alone because the slide is highly periodic. The bright spots in the Fourier transform image will be broader the more shifted the Ronchi ruling lines are. We took a radially weighted average (weighting bright pixels further out more heavily) of the intensity in a circle surrounding the first Fourier mode spot and plotted this weighted average versus time as the drops disappeared. This value decreased as the line shifting disappeared, but it showed disappearance times consistently many minutes earlier than did the human eye. This is likely due to the fact that the Fourier transform does not include shape information that our eye naturally looks for and predicts.

We eventually chose to measure disappearance time by eye. Images were given to three separate individuals and each was asked for the disappearance time and a confidence range. The largest difference between stated times was used as the error on all points.

The fundamental cause of drop disappearance is somewhat complicated. There are four major factors at play and it is unclear which is dominant. Each of these factors has the ability to shift the light rays passing through the drop (and, thus, the Ronchi ruling lines) in a way that would allow us to visualize the drop:

(i) Curvature at the ends of the drop

(ii) Decreasing total height of the drop (top views) or increasing width of the drop (side views)

(iii) Broadening diffuse interface between the drop and the subphase

(iv) Decreasing index of refraction difference between drop and subphase

Although all four factors affect the bending of light through the drop, the latter three depend on curvature at the ends of the drop. As the total height of the drop decreases, the path length through the drop decreases, and, thus the shift distance from where a ray enters the drop also decreases. Broadening of the diffuse boundary layer will also decrease the shift distance. Decreasing index of refraction difference will decrease shift distance by decreasing the change in angle of the incoming ray. Although these factors are difficult to distinguish from one another, by being consistent in optical methods, we expect that our disappearance times measure the same set of circumstances in each drop.

Densities and viscosities of the various poly(acrylamide) solution subphases were required for analysis. Densities were measured at 23°C using a 5000M Anton Paar Densimeter with μg/mL precision. Density results are shown in Table 3.1. Viscosities for the polymer solutions were measured using a Cannon Ubbelohde viscometer (sizes 450 and 1C, Cannon Instrument Co. State College, PA). Viscosity results are shown in Figure 3.4.

Table 3.1: Densities of various concentrations of 5MMW aqueous poly(acrylamide) solution and aqueous fluorescein solution. Standard deviations were less than 50 μg/mL over 10 trials.

Material	**Density (g/mL)**
DI Water	0.997535
0.2 wt% PA	0.998058
0.4 wt% PA	0.998623
0.6 wt% PA	0.999190
0.8 wt% PA	0.999707
1.0 wt% PA	1.000345

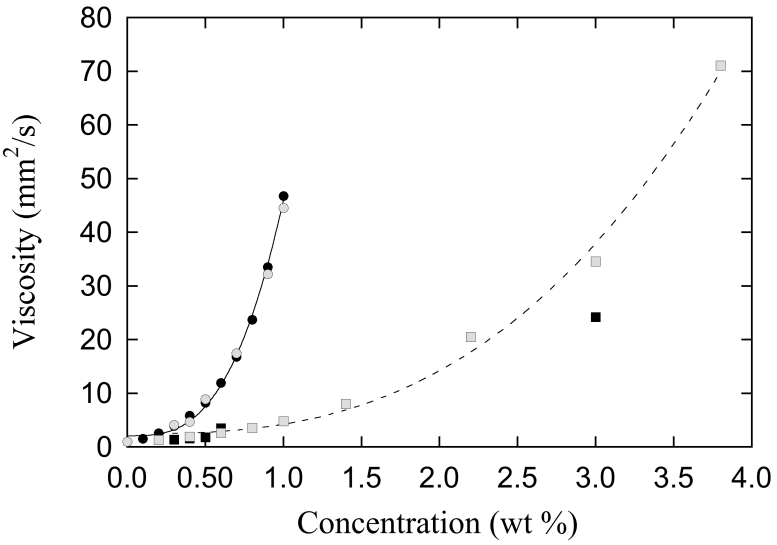

Figure 3.4: Measured kinematic viscosities for aqueous poly(acrylamide) of two different molecular weights at multiple concentrations. 5 MDa PA is shown in circles (black for one trial, gray for a second). 1 MDa PA is shown in squares (black for one trial, gray for a second). The connecting curves are guides for the eye.

3.3 Observed Drop Shape Evolution

Despite being placed gently, the kinetic energy of physically placing a water drop on a PA subphase results in an initially deformed drop shape, as is seen in the earliest panels of Figure 3.1. Significant care is taken to place the drop in the center of the dish or cell so that there will be negligible horizontal forces from the meniscus, and the drop will be as close to axisymmetric as possible [50]. Within seconds, the drop is wetted by the subphase and sits just beneath the surface. Over the next 10 - 30 seconds, the drop recovers from the initial shape perturbation and the forces balance so that its position is static to the precision of our measurements.

As the drop evolves, the wetting film above it does not change in apparent thickness, as measured from the top center of the drop to the bottom of the meniscus (see Figure 3.5). The only change in the drop's center-of-mass height is through shape change. The average apparent film thicknesses over time are 140 $\pm$ 40 μm for the drop on 1% PA and 110 $\pm$ 20 μm for the drop on 0.4% PA with no statistically significant variation. The thickness varies slightly from one experiment to the next. The drop's unperturbed shape is elongated, rotationally symmetric, and nearly top-bottom symmetric (see Figure 3.1 and Figure 3.3 at late times).

Over the next 5 - 20 minutes (depending on subphase concentration), the drop interface gradually becomes more diffuse and the drop shape gradually becomes flatter and more elongated. Visually, the drop outline becomes lighter, broader, and more difficult to discern. This flattening and elongation gives evidence for a decreasing EIT and increasing dominance of gravitational forces in the system (i.e. increasing Bond number.) Eventually, the drop interface diffuses to the point that it is no longer detectable by our optics and "disappears".

These observations provide three ways in which we may examine the EIT between the solvent drop and the polymer solution subphase: 1) The solvent drops recover from the

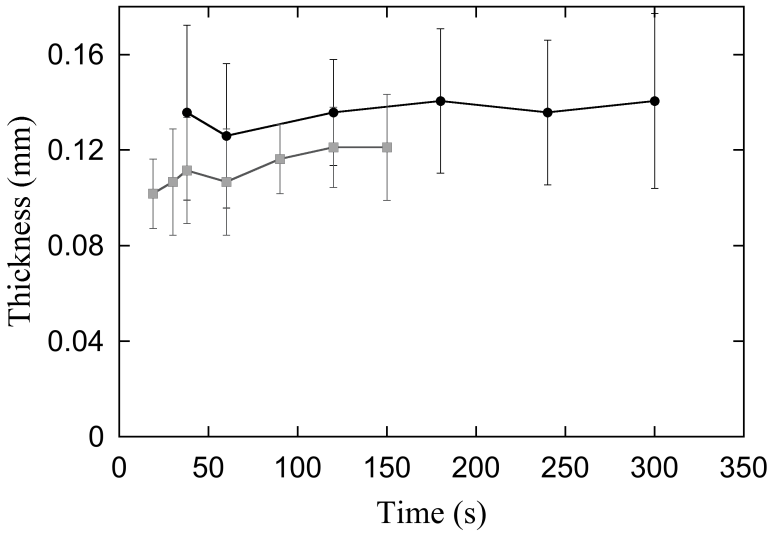

Figure 3.5: Film thickness (measured from the center top of the drop to the closest point in the dark meniscus band) plotted versus time for two drops at different concentrations. Black circles show data for water atop a 1% 5 MDa PA solution subphase, gray squares show data for water atop a 0.4% 5 MDa PA solution subphase. Error bars represent the standard deviation on the mean for three measurements at each point.

initial perturbation because their capillary forces work against viscous flow to reduce the curvature of the drop/subphase interface. 2) A film of subphase forms between the drops and the air due to the relative magnitudes of the drop/air, subphase/air, and drop/subphase interfacial tensions. 3) The post-recovery shapes of drops can be described by solutions to the augmented Young-Laplace equation (AYLE). We examine each of these in detail below.

3.3.1 Interface shape recovery

Using the recovery time from initial perturbation, we make an approximation of the early-time EIT between PA and water. Recovery is slow, so inertia is not significant. The upper bound on the Reynolds number is 0.15 (using 0.1 mm/s for the velocity of the drop's lower

interface as it recovers, 1.7 mm for the length scale – the distance from the bottom of the initially perturbed drop shape to the bottom of the recovered drop shape, and the viscosity of the less viscous water phase). The recovery is governed by a visco-capillary time, $T = \mu L/\gamma_{DB}$, where γ_{DB} is the EIT, μ is the dynamic viscosity of the subphase and L is the drop size. The time it takes for the drop interface to recover from perturbation and reach a nearly symmetric shape is ~ 20 sec for the 0.4 wt% PA subphase, which has a dynamic viscosity of ~ 5 mPa·s, leading to an estimate for the effective interfacial tension at early times of order 0.5 mN/m. All concentrations of PA subphase yield the same order of magnitude early time EITs. Literature measurements of EITs between polymer suspensions and their monomer (poly(dodecyl acrylate) and dodecyl acrylate [113]) and between microgels and their solvents (poly-N-isopropylacrylamide and water [120]) are shown to be this same order of magnitude at early times. The EIT likely decreases significantly over the course of the experiment as the interface becomes more diffuse.

3.3.2 Wetting condition

In the case of three immiscible phases in contact with one another, three spreading coefficients may be defined to determine the dominant surface tension [23, 109]:

$$\begin{cases} S_1 = \gamma_{BA} - (\gamma_{DA} + \gamma_{DB}) \\ S_2 = \gamma_{DB} - (\gamma_{BA} + \gamma_{DA}) \\ S_3 = \gamma_{DA} - (\gamma_{BA} + \gamma_{DB}) \end{cases} \tag{3.1}$$

where the γ's are the interfacial tensions of the interfaces between the drop (D), bulk (B), and air (A). These spreading coefficients tell us whether the three phases will produce a contact line (if all three are negative), or whether one phase will be completely wetted by another (if one is positive). The spreading coefficient pertinent here is S_3. In this case, if

the drop-air surface tension is greater than the sum of the other two (positive S_3), then the bulk fluid will form a thin wetting film over the top of the drop.

Even though our system contains a miscible interface, it obeys the same wetting conditions as an immiscible system using the EIT for γ_{DB}. The values for our surface tensions are water's $\gamma_{DA} = 71.5 \pm 0.4$ mN/m, and PA's $\gamma_{BA} = 70.8 \pm 0.5$ mN/m; note that PA's surface tension tends to drift downwards by 1-2 mN/m over the first 5 minutes. If the EIT between these two miscible fluids is less than $\gamma_{DA} - \gamma_{BA}$, the spreading coefficient S_3 will be positive and a wetting film of PA will occur. Although, accounting for error, it looks like S_3 could initially be negative or positive, with the downward drift of the PA surface tension (γ_{BA}), it is likely that S_3 will be positive. Our experimental results verify that this analysis of the spreading coefficient correctly predicts the interfacial behavior. As shown in the experimental work, images of drops of water atop PA do, indeed, pinch off from the interface and a layer of PA forms on top of them even though the PA is the denser fluid (see Figure 3.1.)

Additionally, reflection confocal microscopy was used to characterize the macroscopic flatness of the PA interface after a drop of water was placed. These experiments were carried out by collaborators at the Max Planck Institute for Polymer Physics in Mainz, Germany (experimental procedures described here [52, 84]). For comparison to a known low-contact-angle drop, confocal images were taken of a phase separated 1:1 mixture of butanol and heavy water (D_2O). Drops of the butanol rich phase atop the butanol poor phase have a contact angle of $\sim 3°$. This contact line is clearly observed in Figure 3.6, showing that this method can detect extremely low contact angles. When a drop of water is placed atop a PA subphase, no contact angle is observed and the interface is macroscopically flat to less than a micron over ~ 1.5 mm of interface (see Figure 3.7). This suggests that the water drop is, indeed, beneath the surface and that it does not have a strong enough buoyancy force to deform the PA interface.

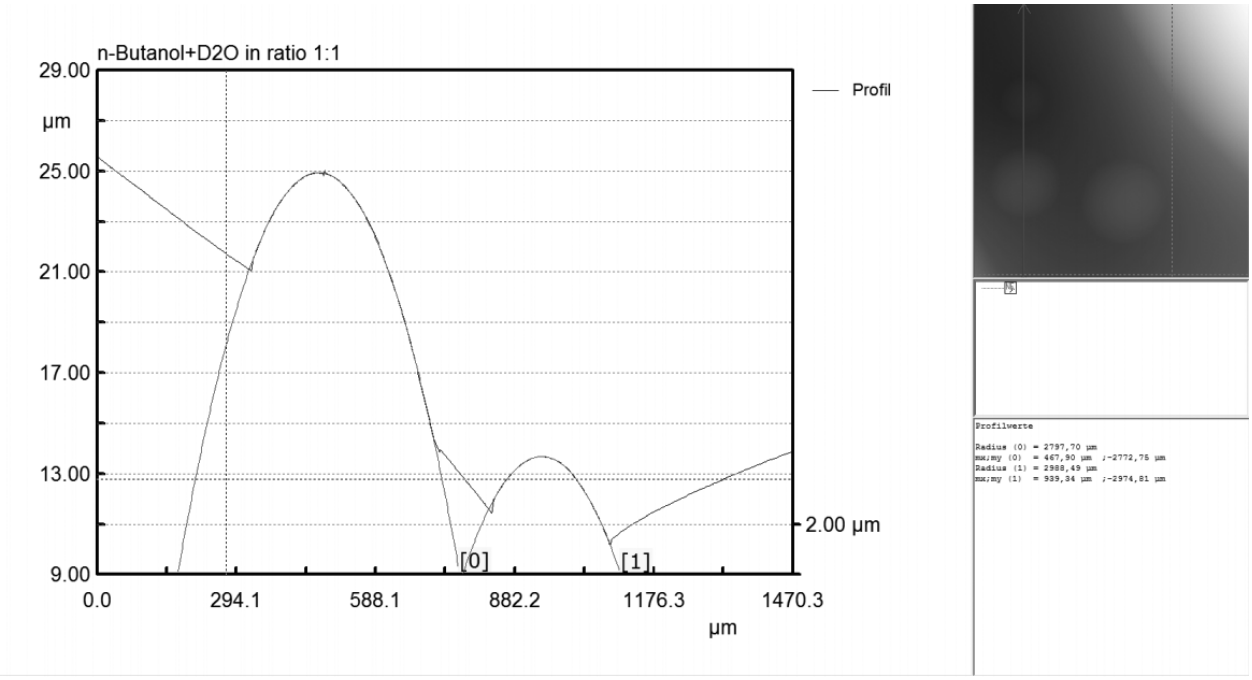

Figure 3.6: Confocal microscopy images of a phase separated 1:1 mixture of butanol and D_2O. The plot shows the roughness of the surface of the butanol poor subphase with butanol rich drops atop it. The drops are measured to have a very low contact angle of $3.0 \pm 0.5°$. Data taken by collaborator Franziska Henrich at the Max Planck Institute for Polymer Physics in Mainz, Germany.

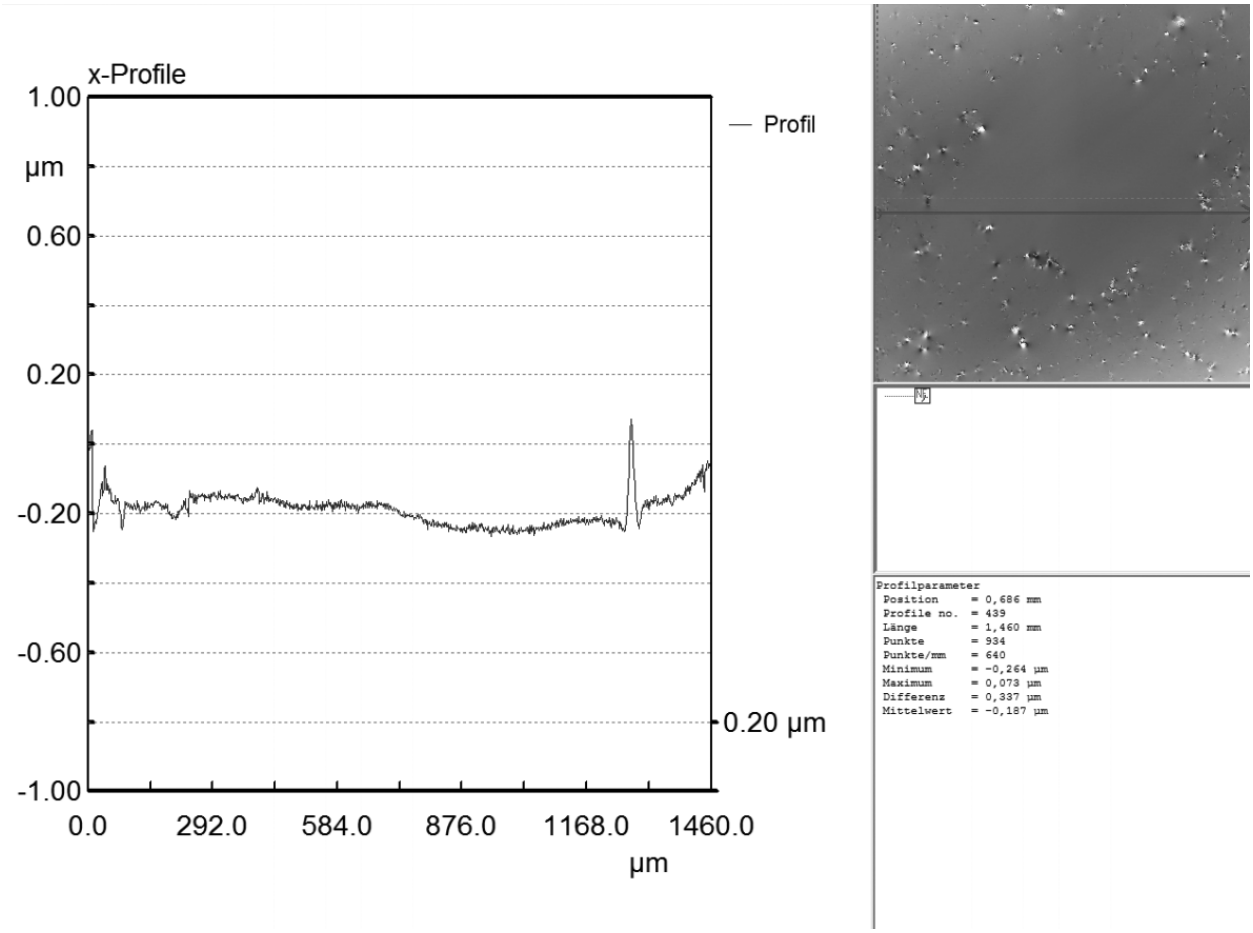

Figure 3.7: Confocal microscopy images of a water drop atop a PA subphase. The plot shows the roughness of the surface. No contact line is detected. Data taken by collaborator Franziska Henrich at the Max Planck Institute for Polymer Physics in Mainz, Germany.

3.4 Pressures Governing Drop Shape

The third observation of an EIT derives from the fact that drops have capillary shapes. In order to examine those shapes further, we use numerical techniques to calculate and fit the drop shape.

We use the augmented Young-Laplace equation (AYLE) for an immiscible drop (for a few examples, see [13, 18, 76, 88, 92]) to analyze drop shapes:

$$\gamma\kappa = P_L + \Delta\rho g z + P(z) \tag{3.2}$$

where κ is twice the mean curvature, γ is the interfacial tension, P_L is the constant Laplace pressure in the absence of gravity (as will be used to define the Bond number in Equation 3.10), $\Delta\rho$ is the difference in density between the outer phase and the drop phase, g is the gravitational acceleration, z is the height change from the reference height, and $P(z)$ is the pressure required to balance the buoyancy of the drop and stop its vertical motion. As shown in Appendix Figure C.1, in order for the solution to the AYLE to form a closed, continuously smooth drop shape in the presence of gravity, it must include an additional pressure opposing the buoyancy. In the system under examination here, this pressure either arises from hydrodynamic forces (due to slow draining of the solution film above the drop or the motion of drop shape change), or from the disjoining pressure of the film covering the drop. To fully solve for this drop shape with hydrodynamics, we would need to consider convective motion within the drop, making this an incredibly difficult problem. Here we will not consider such internal convection as the interface is not being driven [32].

As mentioned earlier, to the detectability limit of our optics, the film above the drops does not change thickness over the course of the experiments and we cannot detect film drainage. However, the buoyant force applied to the film is extremely small due to the very small density difference between the fluids. Assuming the drop is a disk with the same radius

and volume as the drop, the buoyant force results in a pressure of 0.02 Pa applied to the film. With pressures this small and kinematic viscosities between 5 and 45 mm^2/s for the various polymer solutions, the film may be draining too slowly to detect significant motion before the drop is no longer visible. Examples of slow film drainage occurring over hundreds of seconds appear in the literature in systems such as an air bubble in an electrolyte pressed against a quartz plate [18].

When we deposit water drops from beneath the interface, the drops rise to the interface and immediately form a film; they never break the interface and they do not "dimple" on approach (as seen in Figure 3.2). "Dimples" occur when the fluid cannot drain quickly enough and gets trapped against the interface. To contrast, in the case of deposition from the top, the film is first formed when the drop pinches off of the interface, and then it may drain (as seen in Figure 3.1). Both cases produce the same apparent film thickness after initial transients. The absence of both "dimple" deformation and detectable film drainage suggests that the hydrodynamics of film thinning does not contribute significant pressures to the system [18].

While the film thickness is not changing significantly, the shape of the drop is changing due to the temporal evolution of the EIT. Using the characteristic velocity measured for the outward motion of the edge of the drop $V \sim 0.01$ mm/sec, the capillary number may be calculated for this motion. $C_a = \mu V/\gamma$, where μ is the dynamic viscosity of the PA. For our system, $C_a \sim 0.5$, meaning that capillary forces are somewhat greater than hydrodynamic forces in the system at this point. This, again, shows that viscous hydrodynamic forces are not dominant in balancing the buoyant force and halting the vertical motion of the drop.

The second possibility for the source of the additional pressure $P(z)$ in the AYLE is disjoining pressure. Traditionally, disjoining pressures have been investigated only for much smaller film thicknesses than observed here, on the order of the nanometer thickness of a molecular interface. The thickness of the film above our drops is on the order of 100

μm. Disjoining film thicknesses in literature are at most 600 nm for cases involving critical fluids [57, 82] and 120 nm for those involving polymer solutions [28, 64]. However, their corresponding disjoining pressures are measured to be on the order of kilopascals, whereas our estimated pressure applied to the film is 20 millipascals. Thus we are in a position to probe the asymptotic, large-distance tail of the disjoining pressure because of the incredibly low buoyancy force of the drop.

Another possibility for why the disjoining pressure is significant over a larger distance in this particular system is because of the broad, diffuse interface between PA and water. Not much work has been done studying disjoining pressures in entangled polymer solutions with these large film thicknesses. If disjoining pressure is an interaction between the concentration gradients that form the air-PA and the PA-water interfaces, the PA-water interface is quite a bit wider than a simple molecular interface would be. So the added pressure could act over a larger distance than in an immiscible system. Still, this distance would not be hundreds of microns.

We may gain some information about the form of this disjoining pressure by taking a polynomial expansion of $P(z)$ about the vertical position $z = 0$, which we will set to be the point of peak curvature in our drops, and then assessing the significance of each term. This can be done for any given function $P(z)$ so long as it is smooth and differentiable in the region of the drop. Equation 3.2 then becomes

$$\gamma\kappa = P_L + \Delta\rho g z + (P_0 + P_1 z + P_2 z^2 + P_3 z^3 + P_4 z^4 + \dots) \tag{3.3}$$

Given this description of the disjoining pressure, the polynomial coefficients can be probed using the observed curvature of the drop. This is done by analyzing and fitting Equation 3.3 to the shapes of the drops seen in Figure 3.1. However, we cannot separate the contributions of P_L from P_0 or $\Delta\rho g$ from P_1 without independent information on the form of $P(z)$ or the

value of the EIT. The AYLE, therefore, does not permit the determination of EIT by drop shape analysis alone.

3.5 Fourier Analysis to Examine Drop Curvature

3.5.1 Determining a drop outline

The side-view images pictured in Figure 3.1 were imported into Photoshop in order to create a single-pixel outline of each drop at multiple time steps. It was helpful to increase the pixel density of the image in order to avoid sharp pixel jumps in the later Fourier analysis. These outlines were drawn by eye. Other image analysis methods may be used to automatically locate the outline (such as using the ImageJ "MorophoLibJ" morphological segmentation plugin), however the quality of our images and the uneven diffuseness of the interface do not provide the uniform intensity gradient required for these sorts of automated processes. Once the outline was selected using the Photoshop pen tool, it was then drawn (or "stroked") using a single-pixel-wide pencil tool. The resulting outline was then saved as a high resolution image to be imported into Mathematica for analysis.

The reproducibility of this tracing process is shown in Figure 3.8 and Table 3.2. Residual distances were taken as the Euclidean distance between points with the same normalized arclength. This residual distance was on the order of 0.01 mm between three hand-drawn outlines of the the same drop. In order to examine the symmetry of these drops, we flipped the drops about their midline and calculated the residuals between the drop and its inversion. These residuals were less than or equal to 0.01 mm, slightly smaller on average than the residuals between three outlines. As we continue in this section, it is important to remember that the limiting factor – the factor that introduces the most error – in producing accurate drop shape representations is the outlining process.

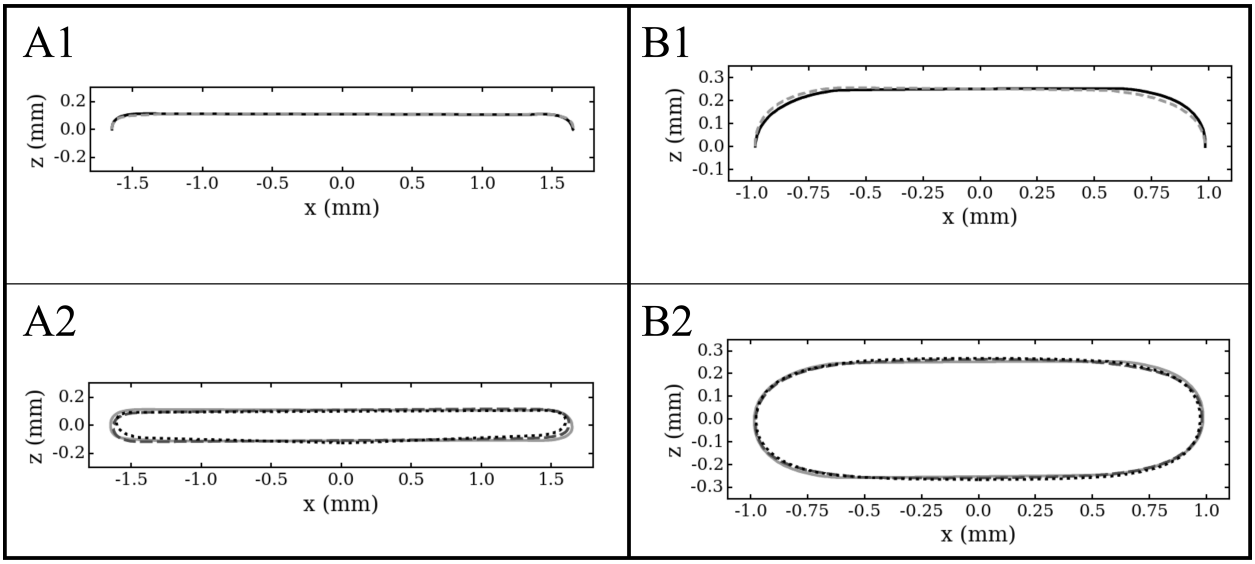

Figure 3.8: A1 and B1 show a sample flat and a sample round drop flipped about their horizontal axes (about our $z = 0$ line). The flat drop is on a 0.4% 5 MDa subphase at 150 s and the round drop is on a 1.0% 5 MDa subphase at 38 s. They are the same drops seen in Figure 3.1 and will continue to be used as examples throughout this chapter. Residual distances between the top of the drop and the flipped lower half are typically less than or equal to 0.01 mm. A2 and B2 show the same flat and round drops outlined three independent times by eye. Residual distances between these three outlines are typically on the order of 0.01 mm.

3.5.2 Interpolating the drop outline using Fourier analysis

We next compute parametric representations of each of the pixel-by-pixel outlines. These data sets are discrete, but may be cast into a continuous form by calculating their Fourier series representation, providing an easily differentiable interpolation of the data [103].

In order to do this Fourier interpolation, the 8-bit grayscale, single-pixel outline of the drop shape is first imported into Mathematica as a matrix. The matrix is searched for all black pixels in the boundary and then compiled into a list of x and z coordinates. The list is ordered along the curve by identifying the points' nearest neighbors using the "Find-ShortestTour" function. This is a greedy function that searches locally near each point to find that point's closest neighbors. It then orders the points by nearest neighbor around the

Table 3.2: Residuals for three cases. 1) residual distances between three independent hand-drawn outlines of a water drop placed on 1.0% PA (a round drop), 2) residual distances between three independent hand-drawn outlines of a water drop placed on 0.4% PA (a flat drop), and 3) residual distances between round and flat drop outlines and their respective inversions about the horizontal midline. This data corresponds to the outlines shown in Figure 3.8.

	Mean Residuals (mm)	**Median Residuals (mm)**
Outlines for a round drop		
1	0.006977	0.008178
2	0.005716	0.006054
3	0.012105	0.012100
Outlines for a flat drop		
1	0.015034	0.015491
2	0.017012	0.020207
3	0.030793	0.032468
Flipped Outlines		
Round drop	0.009539	0.010327
Flat drop	0.001337	0.002090

outline. There is no arc length parameter describing position around the circumference of the drop image intrinsic to the data, so one is defined and appended to the list so that each list element contains (x, z, s). This allows the data to be separated into two curves, $x(s)$ and $z(s)$. The arc length is defined using the Euclidean distance between points:

$$\Delta s = \sqrt{(\Delta x^2 + \Delta z^2)}$$

The full arclength around the curve, T, is then the sum of the Δs steps:

$$T = \sum_{n=1}^{N} \Delta s_n$$

The curve can now be characterized by two functions of arclength, $x(s_n) = x_n$ and $z(s_n) = z_n$. These discrete functions are then interpolated by a Fourier series.

$$x(s) = \sum_k \left(a_k \cos\left(\frac{2\pi k}{T} s\right) + b_k \sin\left(\frac{2\pi k}{T} s\right) \right)$$

$$z(s) = \sum_k \left(c_k \cos\left(\frac{2\pi k}{T} s\right) + d_k \sin\left(\frac{2\pi k}{T} s\right) \right)$$

The coefficients necessary to produce the Fourier Series are calculated from the following equations:

$$a_k + i\, b_k = \int_0^T x(s) e^{\frac{2\pi i\, k}{T} s} ds \qquad c_k + i\, d_k = \int_0^T z(s) e^{\frac{2\pi i\, k}{T} s} ds$$

Because the data are discretized, these integrals must also be discretized.

$$a_k + i\, b_k = \sum_{n=1}^{N} x_n e^{\frac{2\pi i\, k}{T} s_n} \Delta s_n \qquad c_k + i\, d_k = \sum_{n=1}^{N} z_n e^{\frac{2\pi i\, k}{T} s_n} \Delta s_n$$

Using these equations and the values for x, z, and s at each point, we are able to calculate as many Fourier coefficients as we wish and then discretely sum the series in order to get functions for $x(s)$ and $z(s)$. For each data set, the number of Fourier components is adjusted to approximate the data well, while not taking so many components that ringing appears in the curvature, which will be calculated in the following section (see Figure 3.9). Higher order Fourier modes will do a better job of fitting the flatter regions of the drop, but can cause ringing around the high curvature ends of the drop. In order to choose the optimal number of modes for each drop outline, we take the residual distances between the Fourier representation and the drop data for varying numbers of modes (from 2-30). We then find the average and maximum value of these residuals for each number of Fourier modes. The average residuals tend to decrease with increasing number of modes, while the maximum residual tends to increase as more ringing is introduced at higher modes. We, thus, form an objective to be minimized by multiplying the average residual by the maximum residual

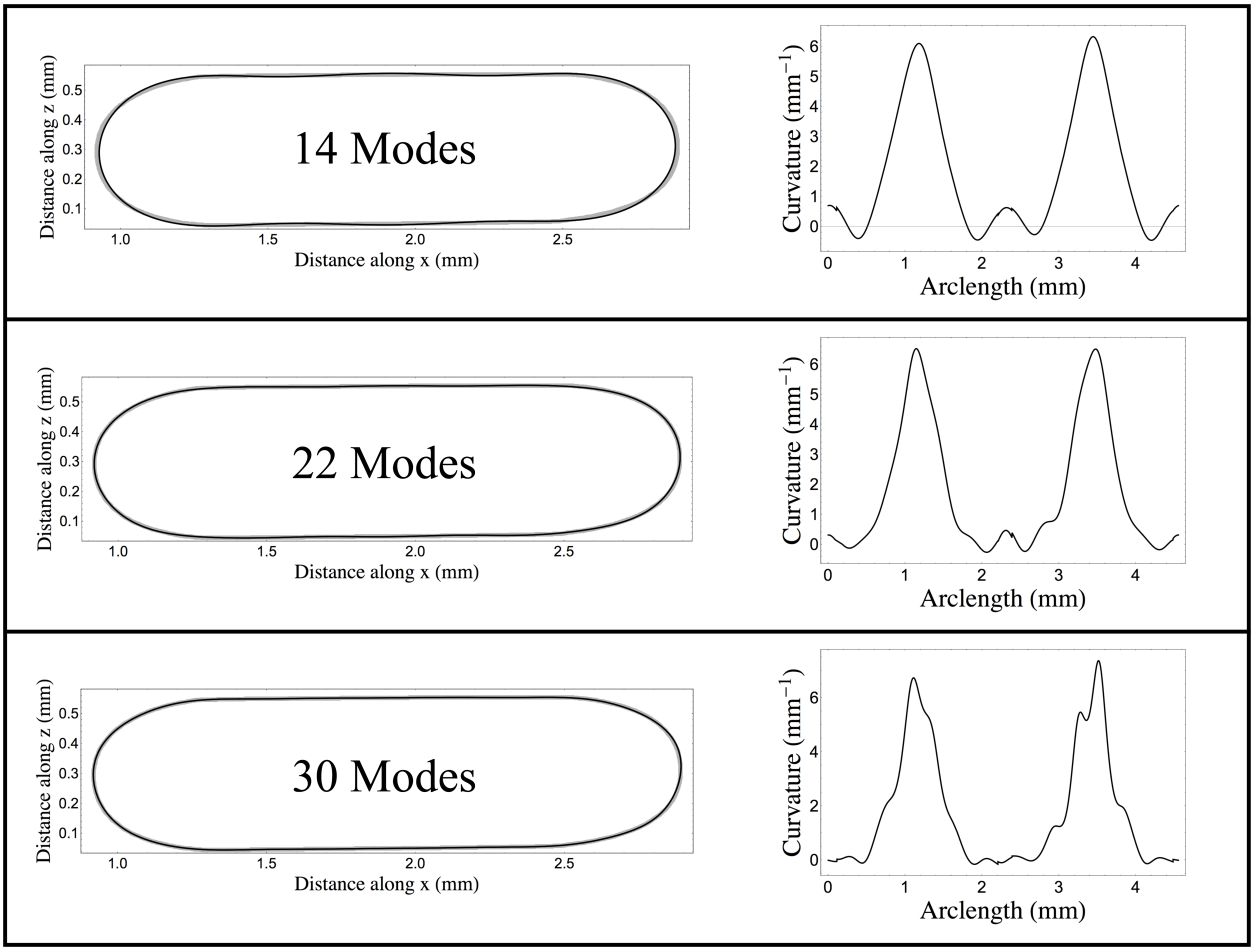

Figure 3.9: Drop outline and curvature attained via our Fourier method for a single drop calculated with three different numbers of Fourier modes. The top panel shows 14 modes, which underfits the drop (as can be seen by the drop outline not matching the drop well). The middle shows 22 modes, which is our calculated ideal based on residuals to the drop. The bottom shows 30 modes, which overfits the drop (as can be seen by ringing in the curvature).

for each number of modes. This multiplied value will have a minimum, which will be the optimal number of modes so as to minimize the average residuals without causing ringing. Deviations between the data and the Fourier representation of the data are an order of magnitude smaller than the uncertainty in the data from the tracing process, as can be seen in Figure 3.10.

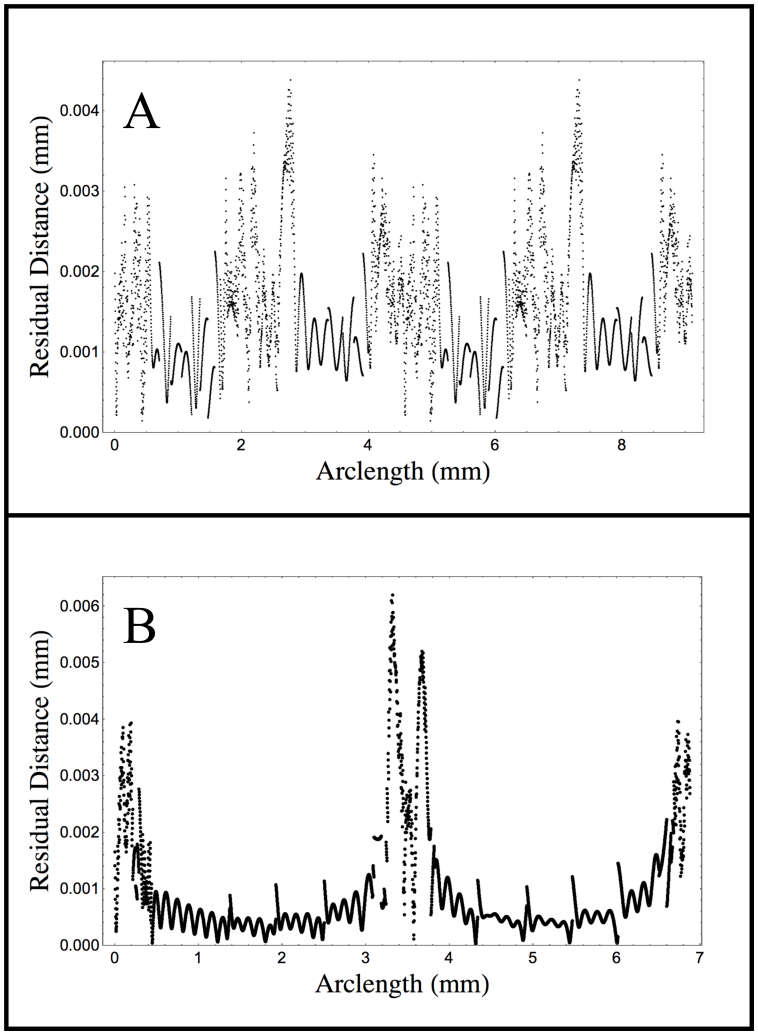

Figure 3.10: Residual distances between the raw drop outline and the optimized Fourier interpolation for two drops. A shows residuals for a round drop (on 1% PA at 38 s) and B shows the residuals for a flat drop (on 0.4% PA at 150 s). Note that the axes have different y maxima.

3.5.3 Calculating the mean curvature along the drop surface

We assume that our drop images are two-dimensional cross sections of three dimensional objects that are rotationally symmetric about their central axis. We believe this to be a good assumption due to the fact that the drops are circular when viewed form the top (see Figure 3.3). Assuming axisymmetry, the full drop surface can be reconstructed by rotating

the profile around its vertical axis:

$$\{x(s), 0, z(s)\} \quad \longmapsto \quad \{x(s)\cos\theta, x(s)\sin\theta, z(s)\}$$

where θ is the angle around the circle as viewed from the top and x becomes our radial coordinate.

For the axisymmetric shape described, the mean curvature, κ, can be written [8, 68]:

$$\kappa = \frac{x(x'\,z'' - z'\,x'') + z'\Big((x')^2 + (z')^2\Big)}{x\Big((x')^2 + (z')^2\Big)^{3/2}} \tag{3.4}$$

where the primes are derivatives with respect to a general arc length parameter, s. Because our drops will have different sizes, we choose our arc length parameter to be normalized by total arc length. The Fourier series representation of our data facilitates taking the derivatives needed to extract the curvature from our data. For more details on how this curvature is derived, see Appendix C.1.

Figure 3.11 shows the curvature data for two typical drops, one early in the drop shape evolution and one later. As expected, this curvature is nearly zero along the top and bottom of the drop, with some ringing due to the limitations of the finite number of terms in the discrete Fourier series, and then peaks at the rounded ends of the drop. We choose z=0 to be the location of maximum curvature, which, in the case of our water drops, is also the approximate mid-plane of the drop. By choosing z=0 at the maximum in the curvature, the net linear term in Equation 3.3 is identically zero. Additionally, the drops, and thus their corresponding curvatures, are very symmetric in z (see Figure 3.8), which suggests that higher order odd terms in the curvature are also small.

From the Fourier representation plots of curvature versus height (Figure 3.11), we can see that the general trend is for the curvature to be an even function of z that opens down-

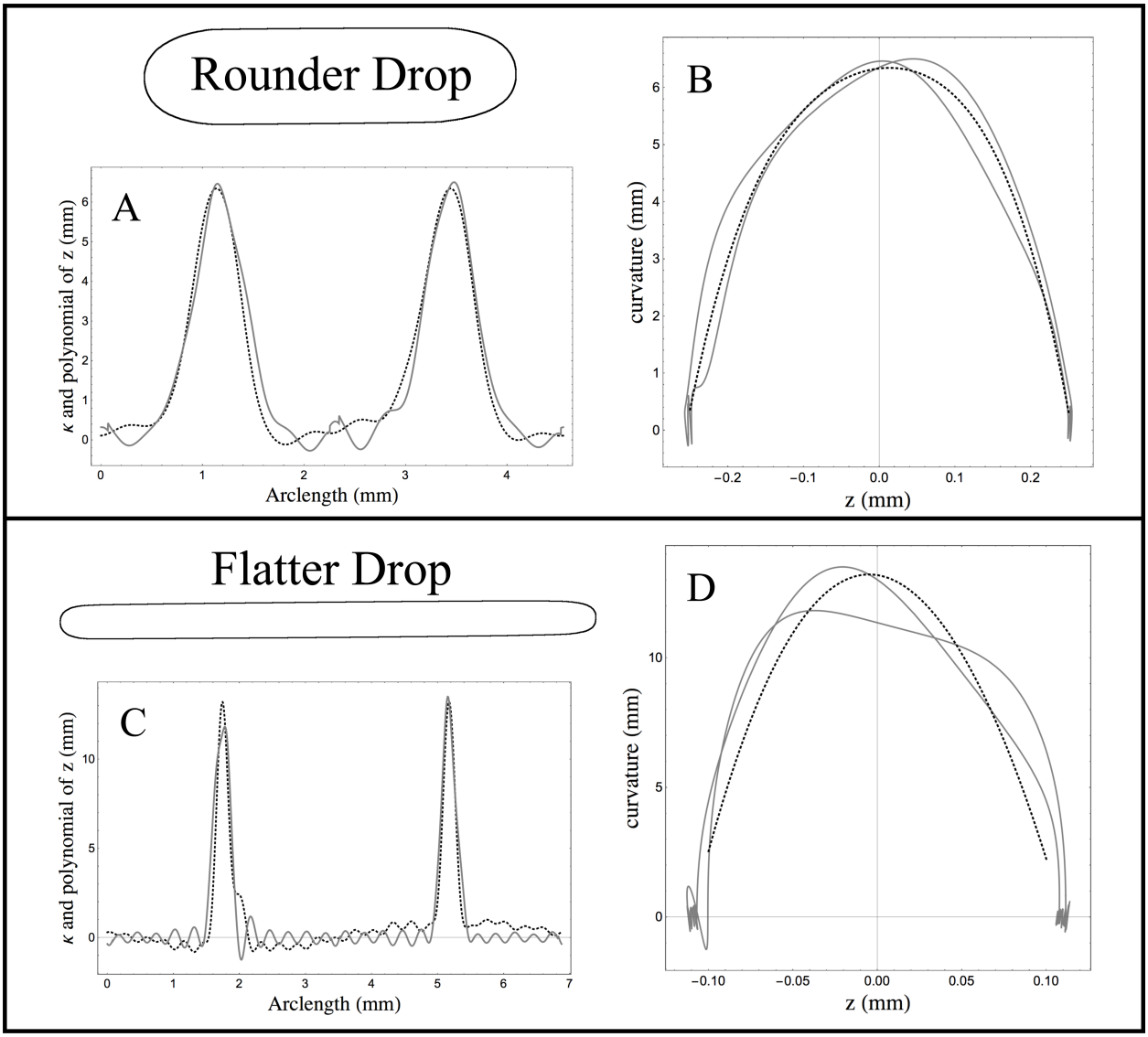

Figure 3.11: Curvature attained via our Fourier method (in gray) and a 4th order polynomial fit to the curvature versus z (in dashed black) for two drops with different shapes (a rounder drop shape in the top panel: A and B, and a flatter drop shape in the lower panel: C and D). The curvature is plotted versus arclength on the left (A and C) and versus z on the right (B and D). In the curvatures plotted versus z (B and D), the two gray curves represent the two ends of the drop; the black dashed curve is the fit, which averages over the two ends.

ward. There are asymmetric components in many of these plots, but, looking at the form of dozens of drops, or over multiple alternative tracings of the same drop, shows us that these

asymmetries are not consistently toward the top or bottom of the drop, meaning they are most likely due to error in our chosen outlines of the diffuse interfaces, possibly amplified by the interpolation and multiple derivatives performed on the Fourier representation of the data. Additionally, the flat regions of the drop are occasionally tilted with respect to the frame. This is likely due to the inertia of initial placement of the drop or the particular choice of drop outline by eye. Again, over many drops, this tilt averages out.

As a check of whether our assumption of symmetry agrees with the curvature data, we fit the curvature versus z data to a 6th order polynomial and examine the magnitudes of each order. As seen in Table 3.3, we find that, as expected from symmetry, the even order terms are systematically larger than the odd order terms and the fourth order term is always larger than the third, fifth, and sixth order terms (see Table 3.3). It is interesting to note that the dominant term in the flatter drops is more likely to be the second order term, while for the rounder drops, the fourth order term is largest. This is likely due to the fact that, as the drop gets thinner, it is sampling closer and closer to the peak in the curvature function and all peaks will look second order as you approach them. This is not a very robust fitting method due to the error propagated through the derivatives and due to the fact that a significant percentage of the data is located at the top and bottom flat regions of the drop at the same z value (see the excess of data points at the top and bottom of the drop in Figure 3.11). However, it does give us a strong sense of what the model for the curvature should be.

This method of Fourier interpolation is quite useful, but has its limitations. It is useful for creating an interpolation of the drop outline data and for getting a sense of what the curvature looks like. However, as can be seen in Figure 3.9, this curvature is highly dependent on the number of Fourier modes used in the fit. Too few modes will result in large oscillations around the outside of the drop shape (see the 14 mode case) and will fit particularly poorly in the flatter regions of the drop. Too many modes will fit the flat regions better, but it will result in ringing in the curvature around the ends of the drop (see the 30 mode case). Ideally,

Table 3.3: This table shows the polynomial pressure expansion fitting parameters for $\kappa(z)$ from our Fourier curvature calculation to a 6th order polynomial in z. The three "outline" columns show fits to three separate outlines of the same flat or round drop. The data in these columns represents the raw fit parameter multiplied by z^O where z is the height of the drop (0.1 and 0.25 mm respectively) and O is the order of the term in the polynomial. Multiplying by this z^O allows us to examine the approximate magnitude of the full n^{th} order term rather than simply the coefficient. The quadratic and quartic fitting parameters are shown in bold. Outline 3 for the thin drop was fit only to 4th order because the 6th order fit severely overfit the data, resulting in residuals that were larger than the data itself.

	Order	**Outline 1**	**Outline 2**	**Outline 3**
Round Drop 1.0% PA 38 s	0	6.37	6.35	6.15
	1	0.04	-0.12	0.33
	2	**-3.89**	**0.22**	**0.60**
	3	0.68	-0.25	-1.39
	4	**-1.41**	**-14.23**	**-12.74**
	5	-0.76	0.39	1.02
	6	-0.74	7.98	6.57
Flat Drop 0.4% PA 150 s	0	10.11	16.39	15.93
	1	0.63	-0.17	4.39
	2	**-9.97**	**-29.25**	**-27.02**
	3	0.39	-0.17	-3.83
	4	**-24.00**	**13.79**	**10.85**
	5	0.06	-0.05	NA
	6	8.39	-0.72	NA

if one wanted to achieve the most accurate calculation of the curvature via this method, one would want to either create a piecewise fitting around the drop with few modes at the ends and many modes in the flat regions, or choose to fit with a set of orthogonal functions better able to approximate both flat and round regions. However, the efficacy of such work must be considered in light of the uncertainties created in tracing the drop shape and would improve with higher quality images. Given the limitations of the Fourier method, we chose, instead, to approximate the right side of the AYLE (Equation 3.2) as a 4th order, even function of z and to fit it numerically.

This symmetric, 4th order model may be used to numerically generate drop shapes, which

may be fit directly to the outline of each drop. Due to the drop's symmetry, we keep only the second and fourth order terms in P(z) and our AYLE becomes:

$$\gamma\kappa = (P_L + P_0) + P_2 z^2 + P_4 z^4 \tag{3.5}$$

3.6 Numerical Solutions to the Augmented Young-Laplace Equation

In this section, the Python code used to numerically solve the AYLE was developed and written by fellow graduate student Bradley Treece.

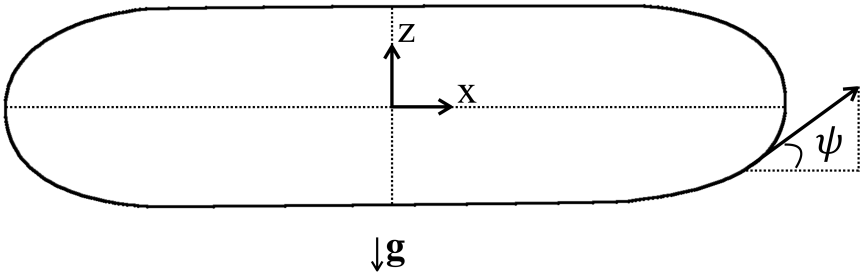

Figure 3.12: Schematic of coordinate system used in anaysis.

We fit the drop shape data (the raw map of pixel coordinates) directly by generating solutions to the AYLE with the truncated expansion of $P(z)$ in Equation 3.5, and adjusting the parameters to minimize the total residual distance between the solution and the drop outline. For this method, we express the curvature in terms of the tangent angle with respect to the surface (for example, see [18]). The derivatives of x and z are the components of the tangent vector to the surface and are therefore defined in terms of the tangent angle to the surface, ψ (see Figure 3.12). Here, the dot derivatives are all with respect to a normalized arc length parameter (rather than the primed derivatives with respect to a general arc length parameter).

$$\dot{x} = \cos(\psi) \qquad \ddot{x} = -\sin(\psi)\dot{\psi}$$

$$\dot{z} = \sin(\psi) \qquad \ddot{z} = \cos(\psi)\dot{\psi}$$

$$\dot{x}^2 + \dot{z}^2 = 1$$

We can then insert these x and z derivatives into our equation for the curvature to find the curvature in terms of ψ.

$$\kappa = \frac{x(\dot{x}\,\ddot{z} - \dot{z}\,\ddot{x}) + \dot{z}\Big((\dot{x})^2 + (\dot{z})^2\Big)}{x\Big((\dot{x})^2 + (\dot{z})^2\Big)^{3/2}}$$

$$\kappa = (\dot{x}\,\ddot{z} - \dot{z}\,\ddot{x}) + \frac{\dot{z}}{x}$$

$$(\dot{x}\,\ddot{z} - \dot{z}\,\ddot{x}) = \dot{\psi}$$

The resulting equation for the curvature is:

$$\boxed{\kappa = \dot{\psi} + \frac{\sin(\psi)}{x}} \tag{3.6}$$

We may now re-write the AYLE with this parametrized curvature:

$$\boxed{\gamma\Big(\dot{\psi} + \frac{\sin(\psi)}{x}\Big) = \Delta\rho g z + P_0 + P(z)} \tag{3.7}$$

To non-dimensionalize this, we choose the lengthscale $(2\gamma)/P_L$, which is the radius of a drop in the absence of external forces ($g = 0$ and $P(z) = 0$). This gives us dimensionless lengths as follows:

$$x = \frac{2\gamma}{P_L}\tilde{x} \quad z = \frac{2\gamma}{P_L}\tilde{z} \quad s = \frac{2\gamma}{P_L}\tilde{s}$$

Then Equation 3.7 becomes

$$\left(\dot{\tilde{\psi}} + \frac{\sin\tilde{\psi}}{\tilde{x}}\right) = 4\frac{\Delta\rho g\gamma}{P_L^2}\tilde{z} + 2 + \frac{2P(\tilde{z})}{P_L} \tag{3.8}$$

Without the added pressures $P(z)$, a single parameter controls the dimensionless shape of the drop:

$$\frac{4\Delta\rho g\gamma}{P_L^2} \tag{3.9}$$

This single parameter can be expressed as a more traditional Bond number

$$Bo = \frac{\Delta\rho g R_0^2}{\gamma} \tag{3.10}$$

where R_0 is the radius of the drop in the absence of gravity and $P(z)$. This traditional Bond number does not take into account the effects of the additional pressure $P(z)$, which would require the definition of a new length scale in the problem.

With our tangent-angle formulation, the differential equations governing curvature are first order (i.e. solving a boundary value problem). The drop shape data is fit using the numerically generated solutions to the differential equations:

$$\dot{\tilde{\psi}} = 2 + a\tilde{z}^2 + b\tilde{z}^4 - \frac{\sin\tilde{\psi}}{\tilde{x}}$$

$$\dot{\tilde{x}} = \cos(\tilde{\psi})$$

$$\dot{\tilde{z}} = \sin(\tilde{\psi})$$

The three parameters (a, b, and an overall scaling factor on the solutions) are fit by minimizing the sum of the residuals of the physical distance between points with the same normalized arc length value in the model solution and in the data.

The numeric solutions to the governing boundary value problem are solved using "scipy.integrate.solve_bvp", a 4th order collocation algorithm for numerical solution of ordinary differential equations available in Python. Similar packages are available in other software. The domain of the solution extends from the bottom of the drop to the top in a counterclockwise fashion, giving half a profile (the drop is assumed to be left-right symmetric). The boundary conditions are that the x coordinate is zero at the top and the bottom of the profile, and that the tangent angle is zero at the bottom and π at the top. The parameters that must be provided externally are the coefficients of the second and fourth order terms in the dimensionless formulation of the AYLE. These parameters are part of the search space used in fitting the drop data.

In order to fit generated drop shapes to the experimental data, Euclidean distances between corresponding points in the two profiles are minimized. Corresponding points in the profiles are determined by matching their dimensionless arclengths. The algorithm used to search for the best fit is scipy.optimize.minimize, given bounds on the parameters that give the correct sign and prevent the aspect ratio of the drop from exceeding about 50:1.

Two examples of our drop fits using this numerical method and their corresponding euclidean distance residuals are shown in Figures 3.13 and 3.14 respectively. The two representative drops are one very round drop from an early time on a high concentration 1% PA subphase and one very flat drop from a late time on a low concentration 0.4% PA subphase. The mean residuals between the drop and the outline are approximately 0.005 mm and the location of the maximum residual distance varies from drop to drop. More examples of numerical drop fits are shown in Figures 3.15 and 3.17.

When we perform these fits to the numerical AYLE solutions, we see that the experimental drops are not consistently deformed asymmetrically upward or downward compared to their fits (47% upward to 53% downward out of 38 samples). Any significant asymmetry would suggest that one or more of the higher odd-order terms played a significant role in

determining the shape (see Appendix Figure C.2). A significant positive or negative cubic term, for instance, would deform the drop upward or downward respectively. In addition, the residual distances between these fits and their corresponding drop outlines are nearly an order of magnitude smaller than the residuals between three different alternative outlines of the same drop (see residuals in Figure 3.8 and Figure 3.13). This suggests that we do not have the experimental precision to measure the cubic term in these drops, if it indeed plays a role, and that our symmetric model was well motivated. Our lack of experimental precision likely arises from the quality of images and complex optics of the system.

In the Figures 3.15, 3.16, 3.17, and 3.18, we show our numeric drop fits and the corresponding curvatures from two time-series of water drops on PA. There are a few key features

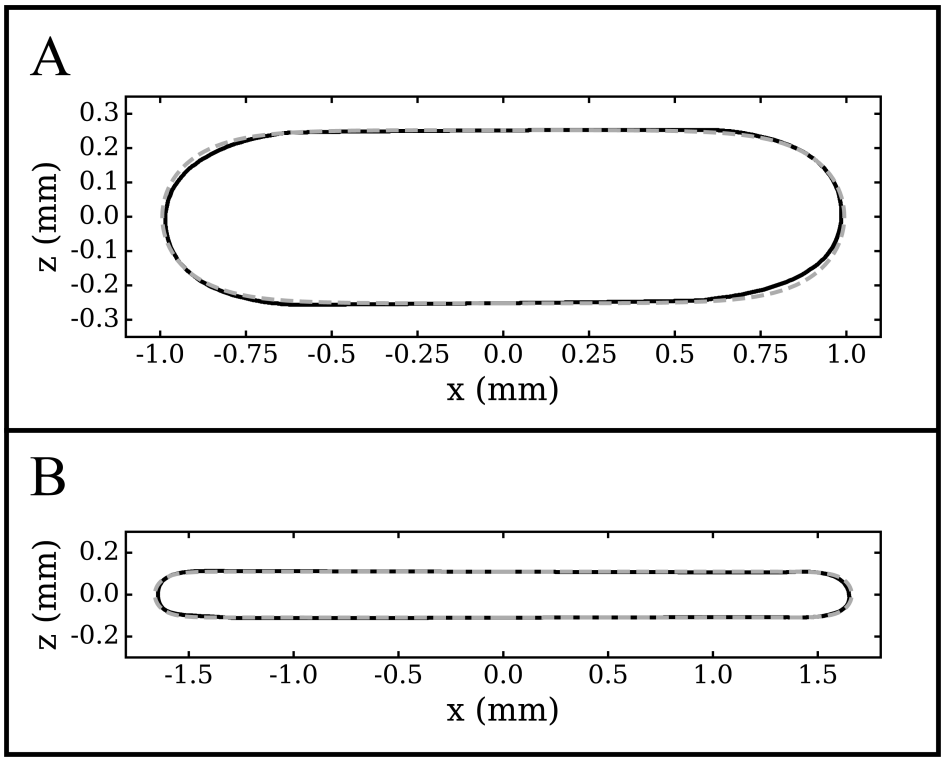

Figure 3.13: Numerical drop fits. A) shows a round, early time (38 s) water drop in 1.0% 5 MDa PA. B) shows a flat, late time (150 s) water drop in 0.4% 5 MDa PA. The original drop outlines are in solid black. The numerical solutions are overlaid in dashed gray.

of note. First, the fits tend to be better at later times than earlier times. This is likely due to the fact that, at early times, the drops are more affected by initial perturbations in shape. Second, the drop curvature becomes more sharply peaked and the overall arclength increases with time. Third, the time that it takes the drops to flatten and achieve a highly peaked curvature is significantly shorter in the case of the less dilute polymer solution (as can be

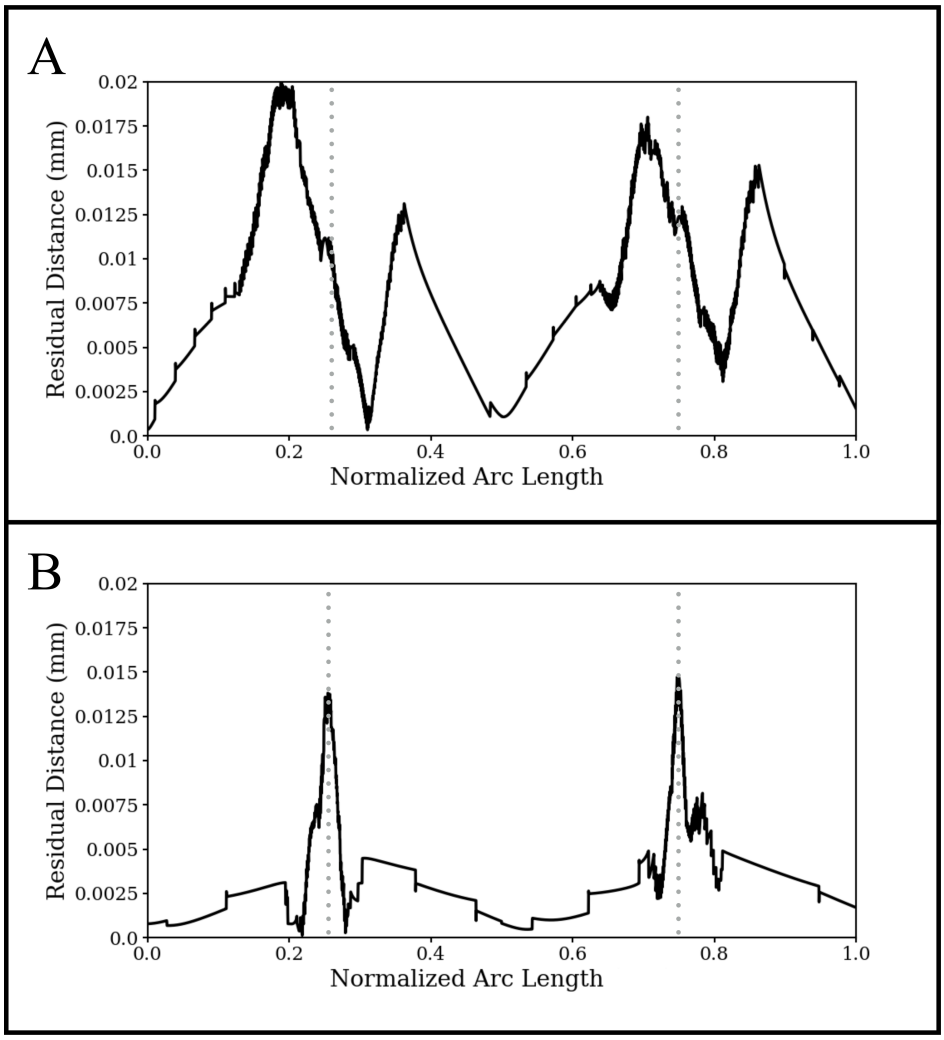

Figure 3.14: Residuals to numerical drop fits. A) shows residuals for the round, early time water drop in 1.0% 5 MDa PA shown in Figure 3.13A. B) shows residuals for the flat, late time water drop in 0.4% 5 MDa PA shown in Figure 3.13B. The dashed gray lines show the $z = 0$ endpoint of the drops. The mean residual distance between the drops and their outlines is ~ 0.005 mm.

seen by comparing the curvatures in Figures 3.16 and 3.18 at 120 seconds). All drops and curvatures are plotted below on the same set of axes so that this difference may be clearly observed.

In Figure 3.19, we show both the numeric fits and the fits to the Fourier-generated curvature for a flat and a round drop. We see that they are in good agreement but that the numerically-generated curvature is significantly smoother. Because the numerically generated curvature comes directly from the solution to the AYLE and not from taking multiple derivatives of interpolated data, it does not contain ringing in the flat regions of the drop or roughness from lack of data points in the curved regions.

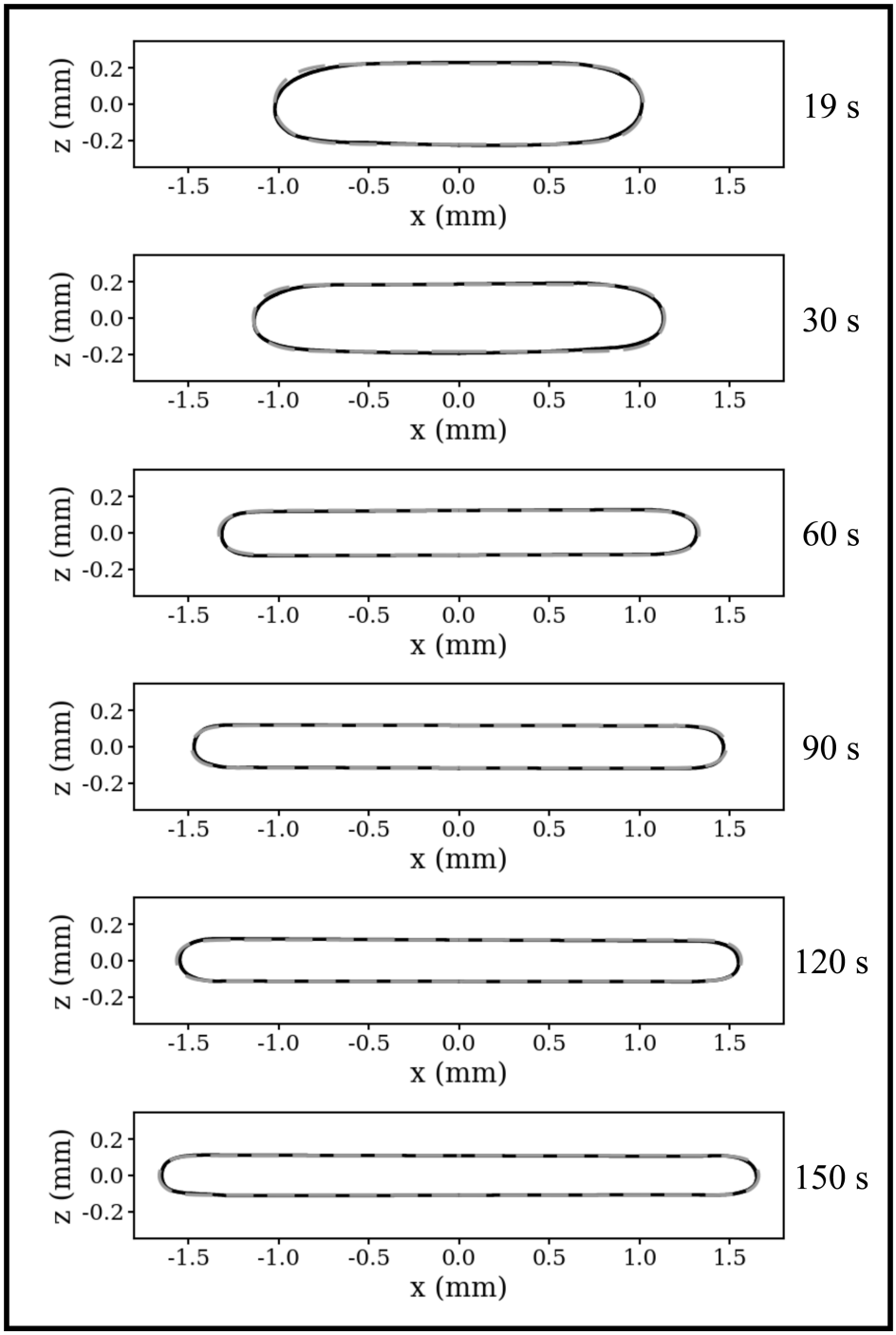

Figure 3.15: Numerical drop fits for a 2μL drop of water placed atop 0.4% 5 MDa PA traced over the course of 150 seconds. True drop outline in black, numeric fit in dashed gray.

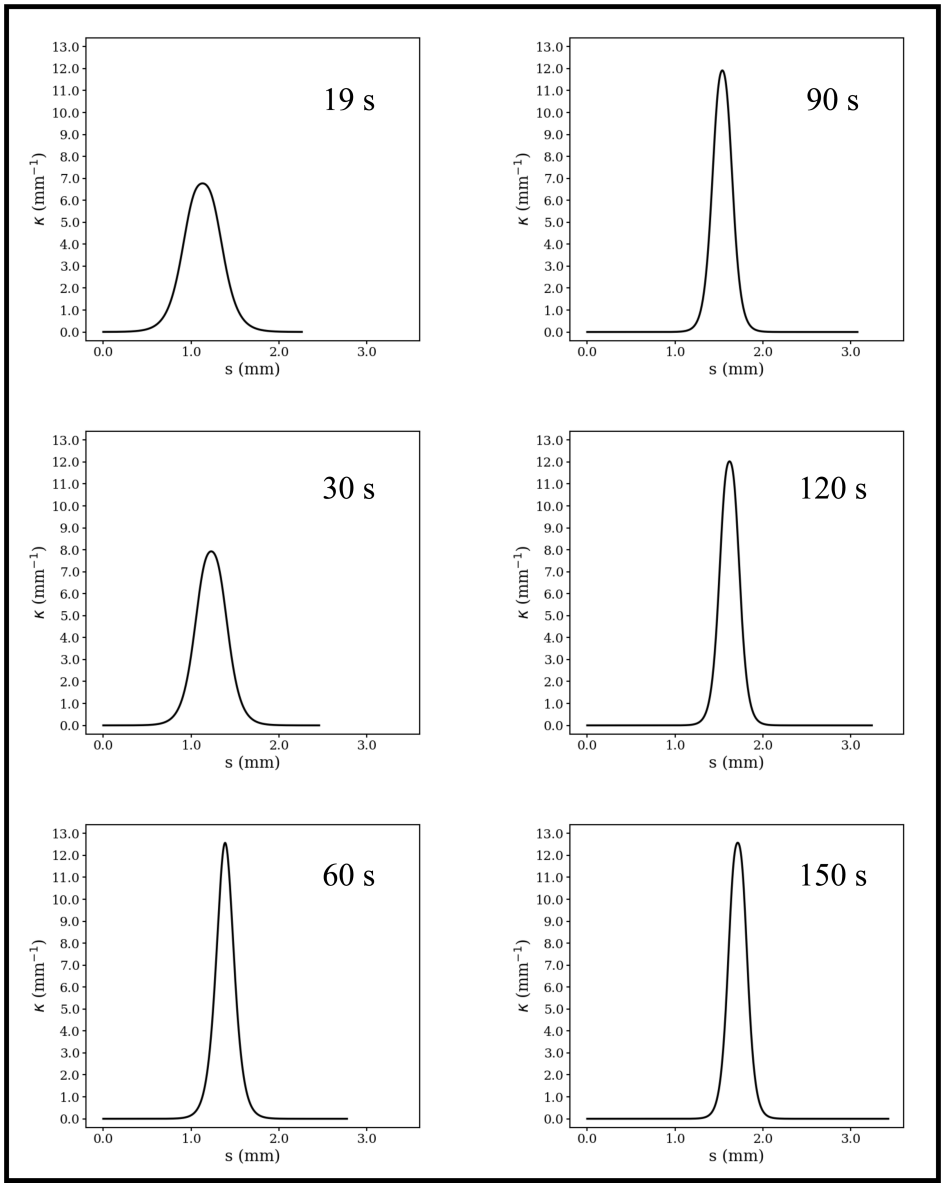

Figure 3.16: Numerical drop fit curvatures for a 2μL drop of water placed atop 0.4% 5 MDa PA traced over the course of 150 seconds.

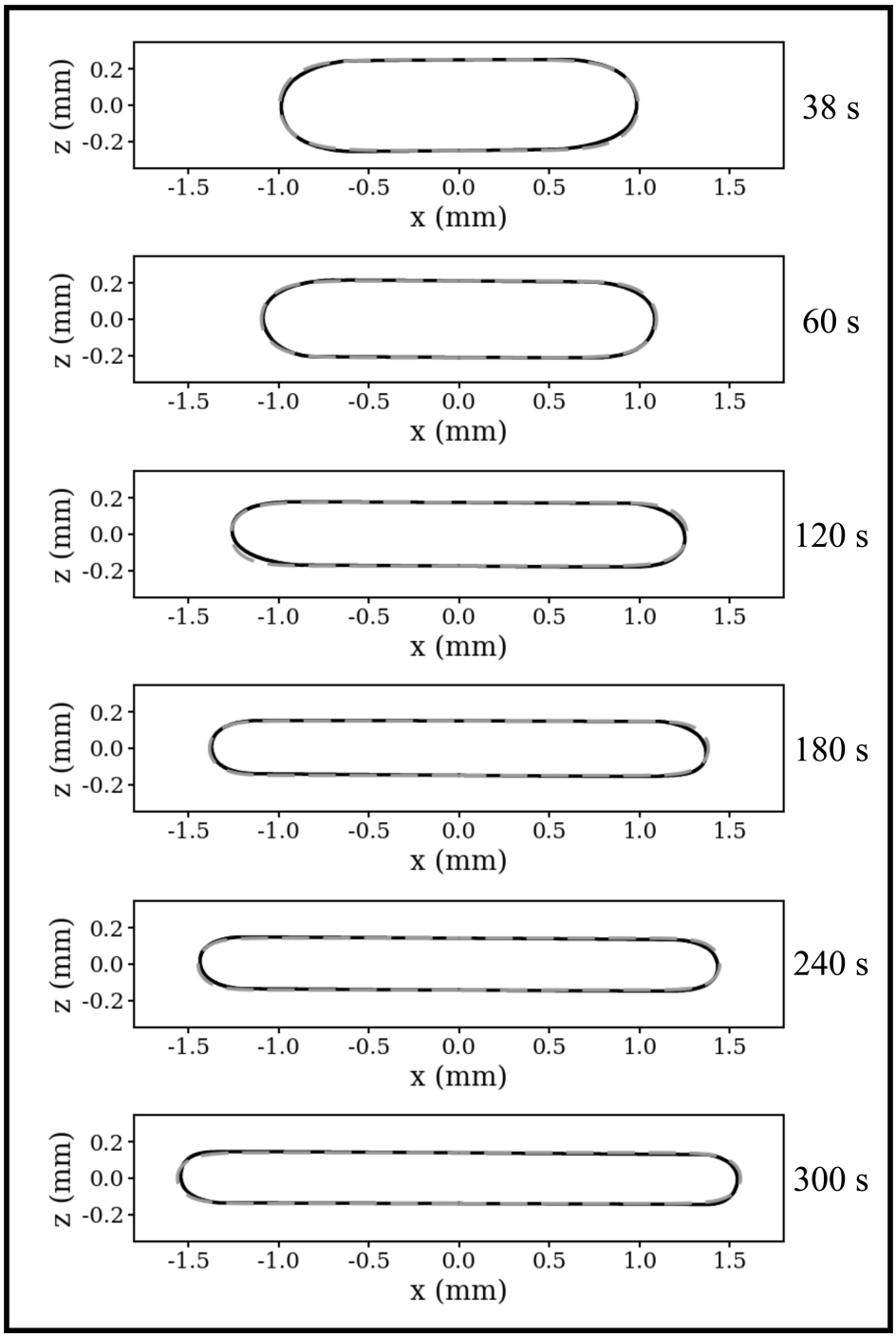

Figure 3.17: Numerical drop fits for a 2μL drop of water placed atop 1.0% 5 MDa PA traced over the course of 300 seconds. True drop outline in black, numeric fit in dashed gray.

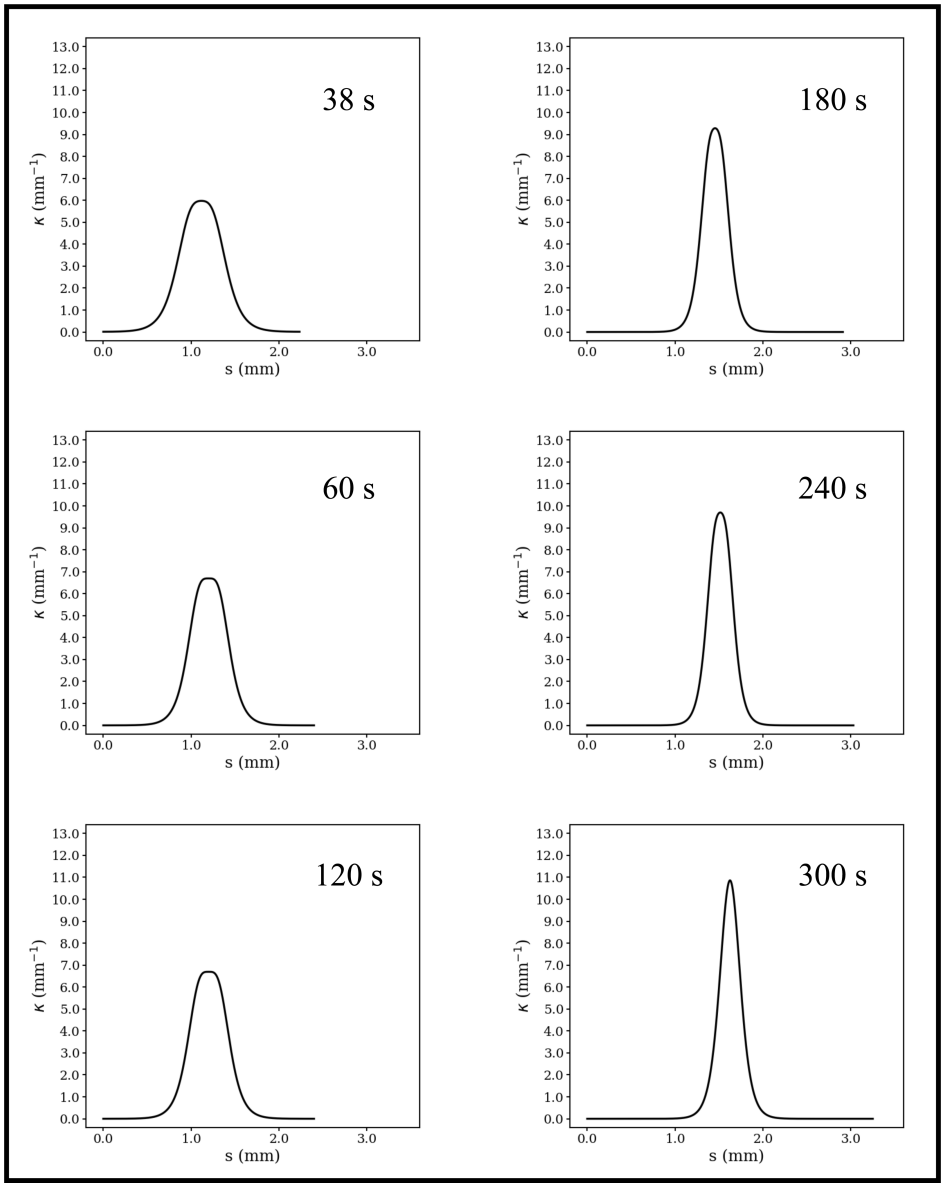

Figure 3.18: Numerical drop fit curvatures for a 2μL drop of water placed atop 1.0% 5 MDa PA traced over the course of 300 seconds.

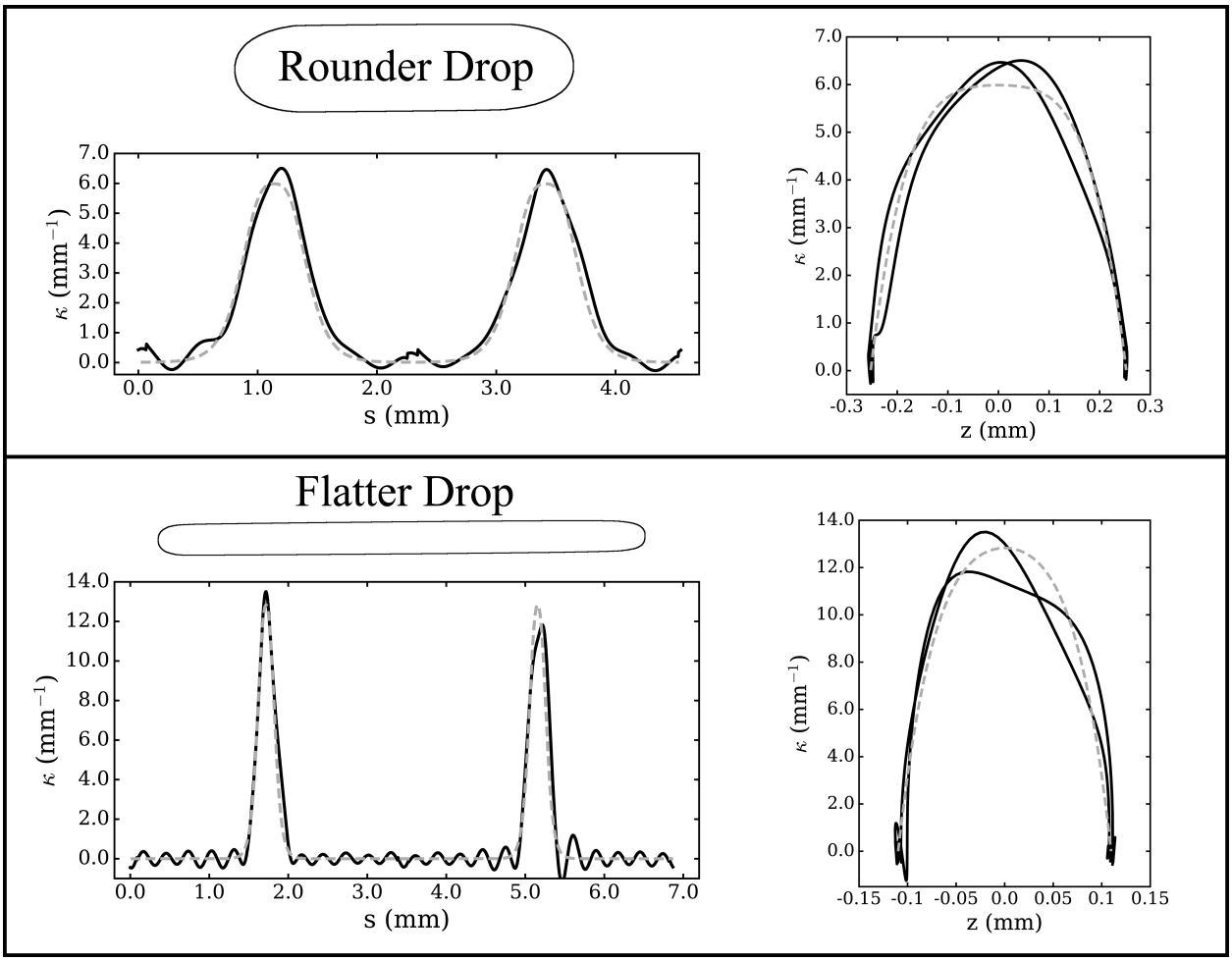

Figure 3.19: Curvature calculated from the Fourier representation (in solid black) and from the numerical AYLE solution (in dashed gray) plotted versus arc length (left) and versus height (right). The top panel shows results for a round drop (water on 1% PA at 38 seconds) and the bottom panel shows results for a flat drop (water on 0.4% PA at 150 seconds).

3.7 Analysis of Drop Curvature and Pressures

Analysis of the drop images and the results of the numeric fitting discussed above show that the drops have apparent mirror symmetry despite the fundamental lack of mirror symmetry in the physical problem. This lack of detectable asymmetry arises first because the drop is flattened and sampling only a small range of $P(z)$, and second because this small range is centered on a peak in the curvature. In the more common case (e.g. an air bubble in water pressing up against a wetted interface), the Bond number is much lower and the bubble covers a greater range of $P(z)$. The bubble curvature is peaked, but the larger range of z reveals the curvature's asymmetry (as will be described in Figure 3.20).

In order to better understand and generalize our description of the additional pressure in the AYLE and the resulting total curvature, we have created a reference plot in Figure 3.20 corresponding to drops of different shapes. This figure shows the two opposing pressures on a drop near an interface. The interface is located at the top of the figure. Note that, in order to show the physical orientation of the interface, our independent variable, z, is on the vertical axis. The buoyancy pressure is positive and linear with z. The additional pressure from the interface is a decreasing function of z, the form of which is not fully understood. Here we show it as a decaying exponential, for illustration's sake. Both of these pressure functions are smooth functions of z, but only physically exist at the surface of the drop. Up to scaling factors, the total mean curvature as a function of height is given by the sum of these two pressures, as can be seen from the AYLE. If the total curvature is a symmetric function, then the drop will be symmetric top-bottom. As we can see in the figure, the curvature is not symmetric everywhere, but it is nearly symmetric very close to the point of maximum curvature. Because our drops have very high Bond number and, therefore, have very small heights (are flattened), they exist close enough to the peak in the curvature that their total curvature function is approximately symmetric.

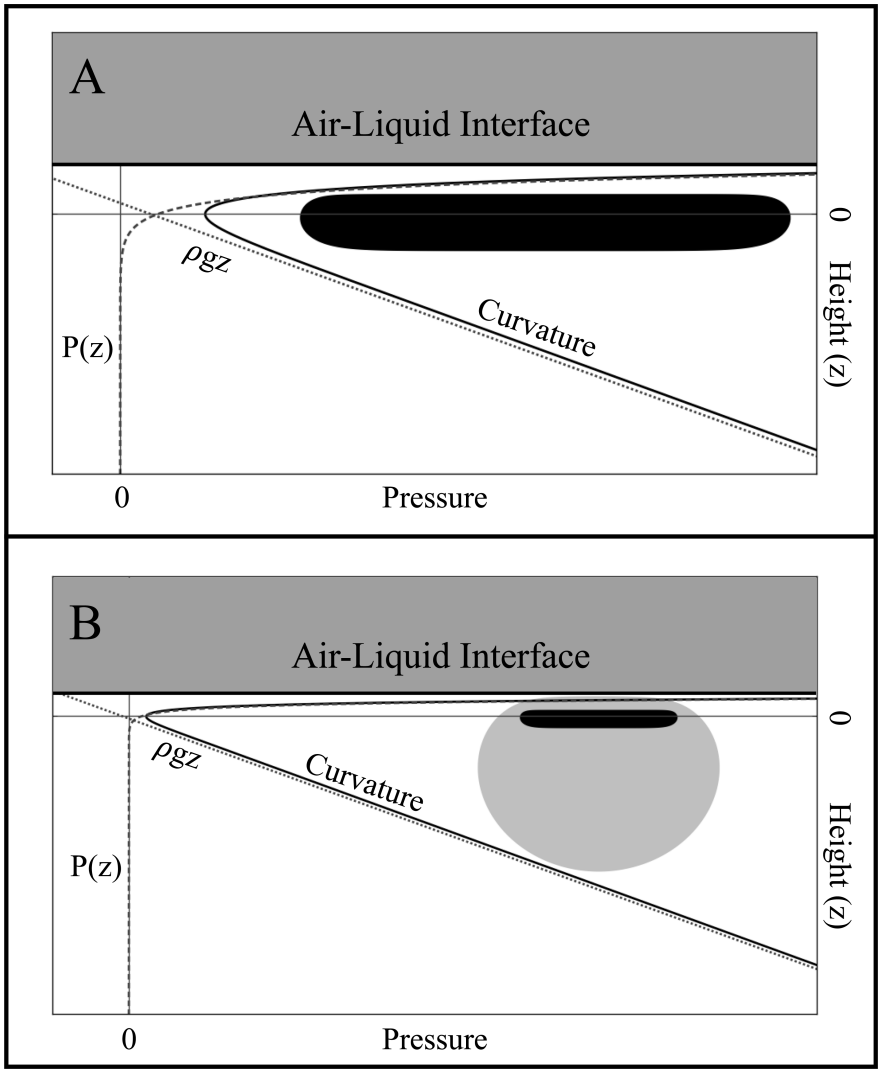

Figure 3.20: Schematic diagram of pressure components acting on buoyant, wetted drops. The air-liquid interface is located at the top of each plot. The dotted lines show the buoyancy pressure, which goes linearly with height. The dashed lines show an illustrative functional form for $P(z)$ (a decreasing exponential in z), which is largest near the interface and then decreases to zero far away. The solid black line shows the sum of these two pressures, which, but for scaling factors, is the curvature of the drop. Panel A shows the case of a highly symmetric drop spanning a highly symmetric piece of the curvature. Panel B is zoomed out to show both the highly symmetric drop and a highly asymmetric drop that spans a greater height and, therefore, a more asymmetric portion of the curvature. Note that the pressures have been shifted slightly along the vertical axis to allow for better visualization. This does not affect the form of the resulting curvature.

Other cases may also be visualized in Figure 3.20B, which contains the same pressure fields extended to higher z values. For example, if a drop with the same pressure fields were to be significantly larger or have a significantly lower Bond number, it would span a greater height. This means the total curvature would be significantly more asymmetric. The portion of the drop at high negative z values would be less affected by $P(z)$ and the curvature would be primarily determined by the buoyancy pressure. This is exactly the case for a standard sessile drop. These drops are highly asymmetric, bulging away from the interface. In this case, it would be possible to measure the effective interfacial tension of the drop. The $P(z)$ term would be negligible except very close to the surface because the height range over which $P(z)$ acted would be smaller than the total height of the drop. The EIT could then be determined directly by neglecting the region near the interface in the shape analysis; $\rho g/\gamma$ would become the linear fitting parameter. However, in our case of a water drop on PA, because $P(z)$ acts over the whole drop, its effect cannot be neglected. This means that, without a priori knowledge of the form of $P(z)$, we cannot directly measure the effective interfacial tension using this method.

3.8 Drop Spreading and Dissolution

3.8.1 Power law growth of drop diameter

The diameter of drops of water under a PA surface can be determined from either the top or side views. The drops' diameters increase as power laws with time, as shown in Figure 3.21. Systematic variation in the exponent with polymer concentration cannot be determined from our data (see the different results from two identical trials in Figure 3.22).

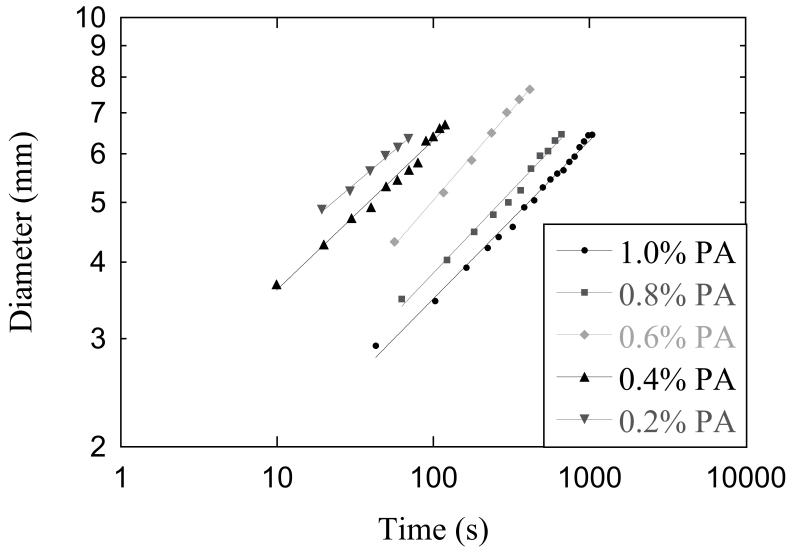

Figure 3.21: Diameter versus time for a 2μL water drop atop multiple concentrations of 5 MDa aqueous poly(acrylamide) solution subphases. The data shown here are for five individual trials taken in the top view setup. The same power law trend is seen when taking diameter data in the side view setup.

As mentioned above, the capillary number for this spreading is less than 1. The Reynolds number is also less than 1. Therefore the spreading is likely driven by the slow decrease in the EIT. We note that immiscible sessile drops spreading on top of a liquid pool with constant surface tensions often also exhibit power law spreading [1, 56]. Although this is a different

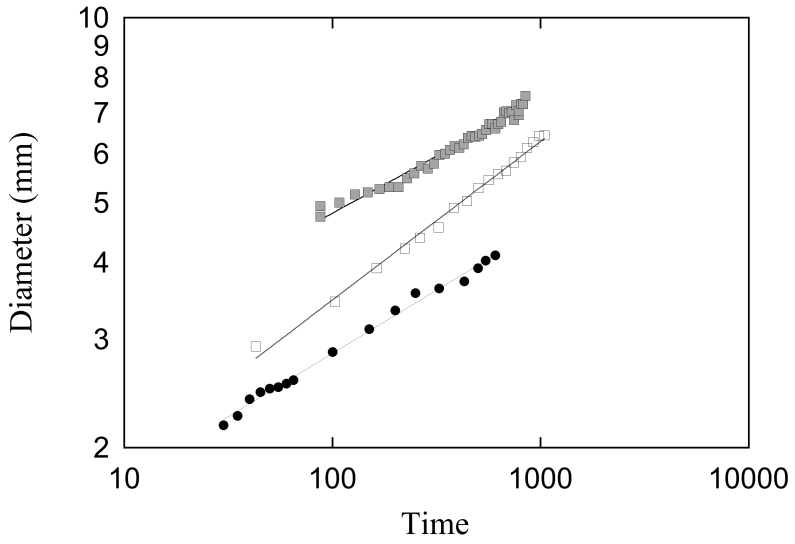

Figure 3.22: Diameter versus time for a 2μL water drop atop 1% 5 MDa aqueous poly(acrylamide) solution from the side and from the top. Two different trials are shown from our top-view setup (gray and unfilled squares) to show variation trial to trial. The third set of data shown is the same system viewed from the side (black circles) to show that side and top view setups give similar results. Exponents for the power law fits are 0.20, 0.26 for the two top-view trials and 0.19 for the side-view trial.

case – driven by contact line forces rather than surface tension change – there may be a connection between the mechanisms that is worth investigating. To solve for the power law spreading theoretically, one would have to solve for the coupled flow fields inside and outside of the drop. Such work has been done in the case of a gas bubble pressed against a liquid-gas interface with zero Bond number [18], and in the case of drops sliding along an inclined surface [50].

3.8.2 Relationship between disappearance and interfacial tension

As discussed above, the drops eventually disappear in the optical measurements. This is due to some combination of the decreasing height of the drop (caused by the lowering EIT

Table 3.4: This table shows power law growth coefficients and R^2 values for the drop trials shown in Figure 3.21. Power law fits were of the form Diameter = At^B. The data shown here is for five individual trials taken from the top. The difference in the value of the power for two trials on the same subphase is approximately the same as the difference between subphases.

PA Concentration (wt%)	**A**	**B**	$\mathbf{R^2}$
1.0	1.06	0.26	0.99726
0.8	1.12	0.27	0.99438
0.6	1.30	0.29	0.99855
0.4	2.09	0.24	0.99256
0.2	2.56	0.21	0.99742

and concomitant spreading of the drop), the broadening of the diffuse boundary between the drop and subphase, and the decreasing index of refraction difference between the drop and the subphase. Thus, the disappearance is indicative of some later stage of dissolution of polymer chains into the drop and water into the subphase. Figure 3.23 shows that the disappearance time increases with increasing polymer concentration.

Disappearance is controlled by diffusive, not by convective, processes. We observe no optical evidence of mixing patterns in our side views. Being diffusive, the EIT is expected to decrease with the square root of time [10]. Dissolution of the polymer into the drop is controlled by (1) water being driven in to the surrounding network by osmotic pressure, (2) reptation of polymer chains out of the network, and (3) diffusion of escaped chains away from the interface [80]. Flow of water out of the drop driven by osmotic pressure should be slow due to the already low molar concentration of the polymer network; only a small decrease in the volume of the drop, $\sim$ 5 - 10% over two minutes, is in fact measured. Using the rotated shape of the drop to calculate the volume, a water drop atop 0.4% PA decreased from 2.66 to 2.24 μL between 38 s and 150 s, and a water drop atop 1.0% PA decreased from 2.64 to 2.51 μL between 120 s and 240 s.

The balance of this diffusion and the unknown reptation time for chains leaving the network will determine if the dissolution process is transport limited. In our case of a drop of water atop PA, the small osmotic driving force likely decreases as polymer chains reptate into the drop. In the inverse problem of a drop of PA solution placed atop water, the PA drop disappears almost instantaneously, suggesting that the osmotic driving force is maintained due to the effectively infinite reservoir of solvent outside of the drop.

For miscible interfaces between long-chain polymer solutions and their solvents [112],

$$\gamma = \frac{K}{\delta}(\Delta\phi)^2$$

where γ is the effective interfacial tension, K is a material constant for the polymer, δ is the breadth of the diffuse interface, and $\Delta\phi$ is the difference in concentration between the two liquid phases. The optical properties driving the disappearance of the drop depend on both γ and δ (as we discussed in Section 3.2.2). We see that the disappearance time varies quadratically with the concentration of polyacrylamide in our subphases, which suggests that the quantity $(\gamma\delta)$ is proportional to the disappearance time. This connection between disappearance time and EIT would be a very interesting area for further research.

This quadratic relationship between disappearance time and concentration extends to a second molecular weight of aqueous poly(acrylamide), 1 MDa. Figure 3.24 shows data for disappearance times on both the 1 and 5 MDa PA (Figure 3.24 is replotted independently of Figure 3.23 because the slopes are so different that the 5 MDa data is difficult to discern on the combined plot.)

As a check to be sure that the disappearance effect we are seeing is based on interfacial tension effects and not on viscosity, Figure 3.25 shows disappearance time versus viscosity for both molecular weights of PA. If disappearance time were dependent on viscosity, this data should collapse onto a single plot. It does not, suggesting that viscosity and disappearance

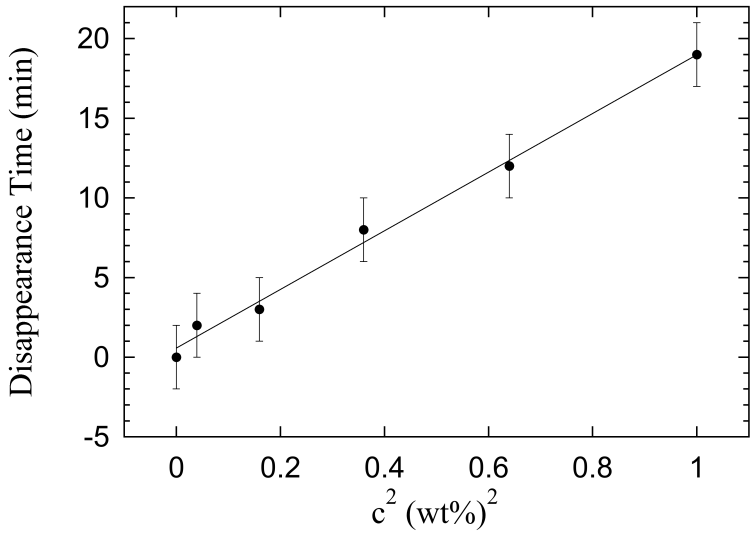

Figure 3.23: Disappearance time versus concentration squared for 2 μL water drops in 5 MDa aqueous poly(acrylamide) solution. The line is a linear fit to the data, which reveals the quadratic behavior of concentration with disappearance time.

time are independent.

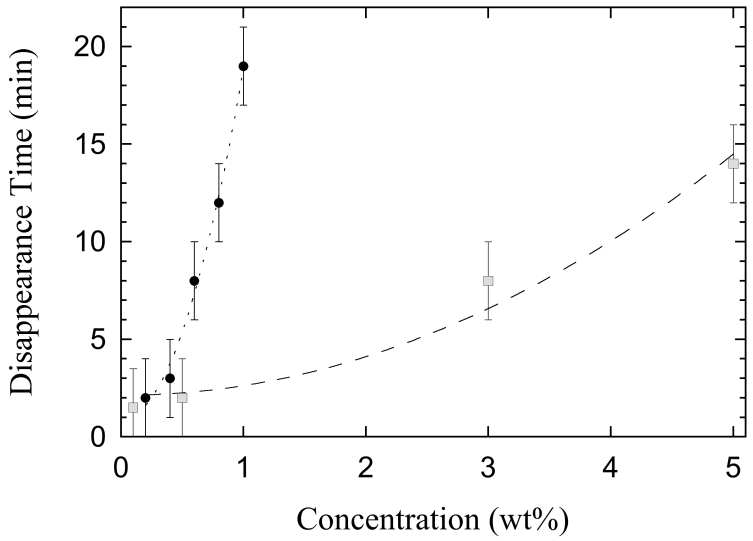

Figure 3.24: Disappearance time versus concentration for 2 μL water drops in 5 MDa (black circles) and 1 MDa (gray squares) aqueous poly(acrylamide) solution. The lines are quadratic fits to the data, which reveal the quadratic behavior of concentration with disappearance time.

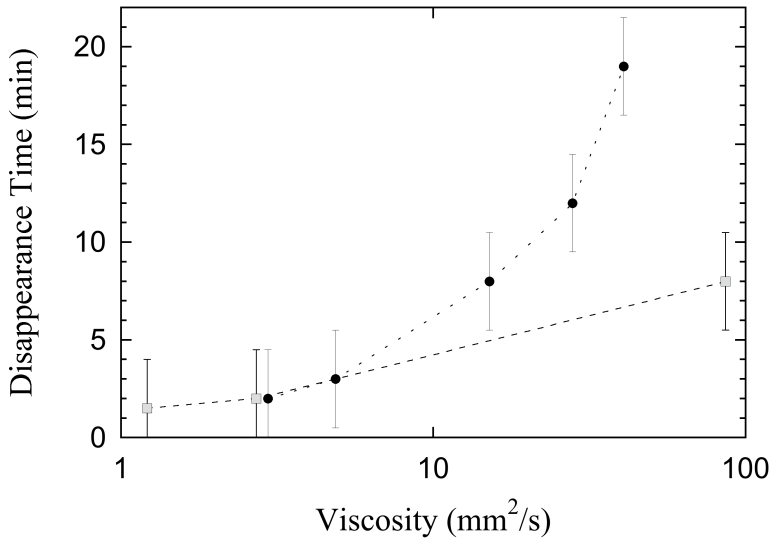

Figure 3.25: Disappearance time versus viscosity for 5 MDa (black circles) and 1 MDa (gray squares) aqueous poly(acrylamide) solution.

3.9 Conclusions

In this chapter, we have clear evidence of an EIT between a polymer solution and its solvent. Drops of solvent atop a polymer subphase recover from perturbation, follow proper wetting conditions, and maintain rounded, capillary shapes for long times.

We are able to examine the shape of these droplets in order to probe the pressures involved. In the case of a solvent drop on a polymer subphase, the disjoining pressure is comparable in magnitude to the buoyancy pressure over the full height of the solvent drops such that these drops take on flattened, approximately symmetric forms. We model these drops by numerically solving an expansion of the AYLE.

The particular experimental system we explore is unique in a number of ways. The fact that the additional disjoining pressure is significant across the full height of the drops is uncommon for sessile drops. Most measurements of disjoining pressures from interfaces are on the order of kilopascals measured over length scales on the order of a hundred nanometers from the interface. The disjoining pressures in the case of this polymer/solvent system are of order millipascals measured over length scales on the order of hundreds of microns from the interface. The small density difference between the two fluids in our system drives this unusual sensitivity. This is a unique class of systems that reveal the form of the disjoining pressure far from the interface.

In addition to examining the drop shapes at a given time, we may also examine these shapes as the interface evolves in time. With time, the interface becomes more diffuse and the EIT between the miscible fluids decreases. This changes the pressures on the drop and, therefore, changes the drop shape.

Chapter 4

Conclusions

Delivery of small droplets to miscible subphases is prevalent in a wide variety of circumstances, from drug delivery to adding honey to tea. This work studies the specific case of drug delivery to the lungs and also examines the general governing forces at play in the behavior of these drops. The specific case involves the use of phospholipid surfactants as initiators of surface-tension driven flows. The more general case examines the wetting and shape evolution of water droplets delivered to a similar aqueous interface.

We have shown that when lipid dispersions are aerosolized onto an air-aqueous interface, they can produce Marangoni flow. We propose that nebulization acts both to shear open vesicles and to create a high surface area on which to store monomeric lipid until it is deposited and transferred onto the subphase surface. Nebulization of the lipid dispersion and direct deposition of the resulting aerosol are both required for significant Marangoni flow.

When the aerosol droplets land on the subphase, they transfer stored monomeric lipid directly onto the surface. They also deliver the non-surface-active re-aggregate SUVs to the bulk. Characteristic of Marangoni flow, the surface flow induces a subsurface flow within the bulk, which causes convection of lipid clusters beneath the surface. This subsurface flow is capable of carrying non-surface-active species such as drug therapeutics beyond the region of deposition.

Because surface tension gradients may be maintained down to very low surface tensions with aerosolized lipid deposition, these dispersions are able to induce Marangoni flow on subphases, such as PGM, that have surface tensions lower than the limiting surface tensions of many common soluble surfactants. Use of surfactant-driven Marangoni flows to enhance the distribution of aerosolized medication in pulmonary drug delivery would depend not only on the ability to drive Marangoni flow on complex lung airway surface liquids with variable surface tensions, but also on their safety in the lung. As natural components of the pulmonary surfactant that is abundant in the respiratory zone of the lung, phospholipids are

good candidates for enhanced pulmonary drug delivery in the bronchi and bronchioles.

The ability to induce Marangoni flow on very low surface tension surfaces is essential if we wish to apply this work to therapeutic applications in the lung, either for enhanced drug delivery using self-dispersing aerosolized carriers or for delivery of SRT formulations. Although the surface tension, and its spatial variation, in the lung is not agreed upon in the literature [2, 49, 93, 95], the fact that surface tensions as low as 1 mN/m can be achieved using aerosolized lipid dispersions means that there is a good chance that these dispersions will spread well in the lung.

When tobramycin was added to the aerosolized phospholipid dispersions, transport of this antibiotic was seen across biologically relevant length scales. Tobramycin transport was not hindered by the presence of pre-deposited lipid, meaning this transport would likely be successful in the lung despite the presence of a preexisting lipid layer.

In order to better understand what controls the behavior of small drops deposited on complex, miscible subphases, we examined drops of water atop aqueous poly(acrylamide) solutions. In this work, we see clear evidence of an effective interfacial tension between the polymer solution and its solvent. These drops recover from perturbation, follow proper wetting conditions, and maintain rounded, capillary shapes for long times.

We are able to examine the shape of these droplets in order to probe the pressures involved. In the case of a solvent drop on a polymer subphase, the disjoining pressure is comparable in magnitude to the buoyancy pressure over the full height of the solvent drops such that these drops take on flattened, approximately symmetric forms. We may model these drops by numerically solving an expansion of the augmented Young-Laplace equation. We find that, due to the uniquely small density difference in our experiment, we are able to probe the tail end of the disjoining pressure far from the interface.

In addition to examining the drop shapes at a given time, we may also examine these shapes as the interface evolves in time. With time, the interface becomes more diffuse and the

effective interfacial tension between the miscible fluids decreases. This changes the pressures on the drop and, therefore, changes the drop curvature.

This work opens the doors to exciting potential future projects. As treatments for CF and other lung diseases improve, this work will provide the ability for these treatments to be delivered effectively to the lungs of affected patients. Perfecting these methods will require a deep understanding of the governing forces driving shape and dissolution behavior of two-phase miscible systems. The methods described here will, hopefully, continue to aid in the development of this rich field.

4.1 Future Work

4.1.1 Phospholipid-induced Marangoni transport

There are a number of important directions for the continuing study of Marangoni transport in the lung. Our work is limited by our ability to completely simulate all the complex characteristics of the airway surface liquid layer, including mucociliary clearance, heterogeneous surfaces, and thin liquid films. The simplified systems used in these experiments do not capture the lung's compound layers of fluid and cells, its pre-existing surfactant content, its cylindrical geometry, or its ability to perform mucociliary clearance. These complexities may alter or limit Marangoni transport.

In the future, we should consider aerosol-induced transport on thin liquid layers, which may differ from transport on the deeper liquid pools used here. When transport occurs on thin liquid layers, the lower bounding interface becomes important to determining flow patterns. Because Marangoni spreading creates a longitudinal wave with height proportional to the surface tension gradient, there is the possibility that this outward wave of fluid will de-wett the lower interface. There is also the possibility that the top of the Marangoni wave

will touch the other side of a small, cylindrical airway and create a fluid bridge that could block the airway. Because of these effects, it is likely that a small, steady concentration gradient will be preferable to a very large gradient so that the Marangoni wave front is not exceedingly large.

Phospholipid delivery from aerosol seems to be ideal for this purpose as the spreading is slow and the gradient at any given point in time is not very large. Future work has already begun (by Steven Iasella) and will continue to examine the effects of induced Marangoni transport on thin films atop various lower bounding interfaces. It would be interesting to include in this work a study of the rate of delivery of surfactant to such thin films. Additionally, this work could be combined with miscible interface work with the possibility for delivery of a thin fluid layer on which to spread. If the interface de-wet, or if spreading was more effective atop a slightly different interface than exists in the lung, a fresh thin layer may be able to be delivered via aerosol and, due to effective interfacial tension, may exist long enough to be spread upon.

Work has also begun (by masters student Haicaho Wu) and should continue to study Marangoni transport in different geometries. The cylindrical geometry of the lung airways, as well as their extremely large total surface area, are quite dissimilar to the small, flat, bounded experiments we perform. It would also be useful to find an experimental way to remove surfactant from the end of a trough or dish during experiments so that the effect of an "infinite" interface can be simulated. This could be achieved by a delicate vacuum or possibly by flowing the packed interface out of the dish and into a waste repository. If this could be achieved, we could examine the role of the rate of deposition in a "nearly infinite" system similar to that in the lung.

In addition to looking at different geometries, work is currently being done to examine the physics of Marangoni transport against a preexisting lipid layer (a collaboration between myself and fellow graduate student Madeline Sauleda). We showed in this thesis that DPPC

will initiate spreading even when it is aerosolized onto a preexisting monolayer of the same lipid. The next step in this work will be to observe the spreading of other soluble and insoluble surfactants against a lipid layer. Preliminary experiments show that insoluble surfactants (such as DPPC and oleic acid) will act as a "piston oil" when spread on a preexisting lipid layer; they will spread until the lipid layer has compressed to be the same surface tension as the deposited insoluble surfactant. Soluble surfactants, however, show very interesting retraction behavior; they spread against the layer at first, but then, as they desorb from the surface, the layer pushes back and the spread area retracts. Both of these types of surfactants have advantages and disadvantages in lung transport. Soluble surfactants have the advantage of desorbing from the interface so that they do not permanently alter the surface tension, however, the retraction would hinder spreading. Insoluble surfactants semi-permanently alter the interface onto which they are deposited, but they do not retract. Understanding the interplay and timescales on which these events occur will be important to refining Marangoni transport in the lung.

The ultra-low surface tensions achievable by aerosolized phospholipid dispersions are also worthy of future research. The phospholipid layers created through aerosolization of DMPC have been observed by ellipsometry to be monolayer structures, however these have only been observed at surface tensions above $\sim$ 20 mN/m (either before ultra-low surface tensions were achieved or after they had had time to recover). It would be very interesting to observe these layers, either using ellipsometry or another surface observation technique such as Brewster angle microscopy, in order to see whether they still have a monolayer structure or some more complicated, three dimensional structure. These sorts of three-dimensional collapse structures are especially likely on mucin where there are added polymer components. Observation of this ultra-low surface tension structure as well as the structure as the surface tension recovers could aid in our ability to predict when and how these sorts of surface tensions could be achieved and whether they might be achievable by other surfactants or by

other methods.

Other methods may also be used to destabilize phospholipid vesicles and allow monomer to be released and induce Marangoni transport. Such destabilization is likely already being caused by peptides and other components within the lung, which allows the preexisting lipid layer to be created. Other techniques (chemical or molecular) could induce similar Marangoni spreading and might have advantages over aerosol deposition in certain cases. It would be intersting to see whether any of these other techniques could be used to achieve ultra-low surface tensions.

There could also be myriad other uses for ultra-low surface tension surfaces. Low surface tension fluids detach from interfaces very easily and form very easily broken droplets. This could be useful for flow problems of many types as well as problems where a high-viscosity/high-surface tension fluid may be difficult to manipulate. These low surface tensions can also cause objects attached by capillarity to an interface to sink (to drown unwanted mosquito eggs or to initiate very gentle sinking in an experiment). Because phospholipids are everywhere in nature, most natural systems would probably be able to tolerate them well.

4.1.2 Miscible drop shape evolution

Work on solvent drops in miscible polymer subphases is already being continued by collaborators (Doctors Hans-Jürgen Butt, Guenter Auernhammer, and Franziska Henrich) at the Max Planck Institute for Polymer Research in Mainz. This research aims to better understand the dissolution and reptation of polymers out of solution and into a solvent drop. The rate of this reptation will control the gradient of polymer concentration that determines the effective interfacial tension between the two fluids. Our collaborators plan to use fluorescently-tagged poly(acrylamide) in tandem with confocal microscopy in order to directly observe the loca-

tion of the polymer chains. Preliminary results have already confirmed the presence of a wetting film atop water drops placed on the surface of PA.

This work on polymer reptation could also lead to a better understanding of the connection between the drop disappearance time and the effective interfacial tension. If we were able to make this connection, either theoretically or experimentally, it would provide a direct link to the theoretical work relating EIT to polymer concentration. This would strengthen our ability to predict dissolution times or EITs for a given system.

In addition to this work, further study on this subject is being continued in this lab at Carnegie Mellon. A visiting undergraduate from USTC, Zhaofei Zheng, has been working to continue this project with other polymer/solvent systems (polyethyleneoxide (PEO)/water and polystyrene/toluene). In both cases, drops of the solvent were visible atop the miscible polymer solution. In the case of PEO/water, disappearance times were seen to be proportional to polymer concentration squared. In the case of polstyrene/toluene, the toluene has a slightly lower surface tension than the polymer solution, thus the wetting condition is observed to be that of a lens, which agrees with its spreading condition. There are, of course, many many more examples of systems where one could observe the shape of miscible drops with low buoyancy forces.

Other systems that have this property of a low density difference will likely share the property of having the drop act as a very sensitive force transducer. This type of high-sensitivity force probe could be useful in a number of ways. If we were to use another method to measure the effective interfacial tension, as suggested by others in the literature, we would then be able to characterize $P(z)$. Similarly, if we had access to the full form of $P(z)$ theoretically, we could use this to determine the effective interfacial tension. Additionally, gradually changing the density of the drop phase could allow the drop to rest at different distances from the interface, allowing the full pressure profile to be observed. This sort of analysis would work whether $P(z)$ arose from a simple disjoining pressure or from some

other applied pressure in the system. It could also provide insight into how the disjoining pressure changes depending on surface structure (i.e. a dehydrated polymer interface versus a hydrated one).

If there were a system for which $P(z)$ were well understood (via the method described above) and for which the dissolution was predictable, then the full progression of the drop shape evolution could be solved for. This would allow us to predict the rate at which the radius of the drop should change with time and to examine its power-law behavior.

When this work is tied back into the problem of Marangoni transport in the lung, there are a few exciting avenues for future study. If droplets with different EITs with the subphase were deposited, it could be observed whether this EIT has an effect on the rate of Marangoni transport. Additionally, Marangoni transport could be enhanced by the addition of a higher surface tension liquid being delivered to the lung ASL before delivery of the surfactant solution. We have seen, in preliminary studies, that when lipid dispersions are aerosolized onto PA solutions, the lipid clusters move within a discrete layer atop the PA solution (see Appendix A.2). Understanding the timescales over which such a fluid layer could exist and comparing those to the timescales of Marangoni transport would be important to the implementation of such a technique.

Appendix A

Further examples of spreading experiments

A.1 Spreading of indicator beads versus talc

We have observed that recorded spreading behavior is somewhat dependent on the tracer used in the experiment. Smaller tracer particles tend to spread further and give a larger recorded spread areas. When compared to molecular markers such as fluid dyes, these smaller particles tend to do a better job of matching the spread area indicated by the dye [100]. Here, we tested two different tracer particles, large $\sim$1 mm polystyrene beads and small talc powder, on the same subphase during the same spreading experiment. The subphase was a 75% glycerine solution in water (chosen because its higher viscosity than water slows Marangoni transport, making it easier to capture via video). A ring made up of half talc and half polystyrene particles was placed on the surface and then a 2μL drop of 0.5 mg/mL tyloxapol was pipetted at the center of the dish. The beads and the talc were then tracked with time. It was observed that the talc spread significantly further than the polystyrene beads. Additionally, the ring of talc compressed as it moved outward (the width of the ring decreased) as the talc particles closest to the point of surfactant deposition moved first and joined the ring and they moved outward together. As in the Sharma paper cited above, two distinct spreading zones were observed: a fast initial spreading and then a slower continuation. These experiments were repeated 6 times with similar results. One example is shown here in Figures A.1 and A.2.

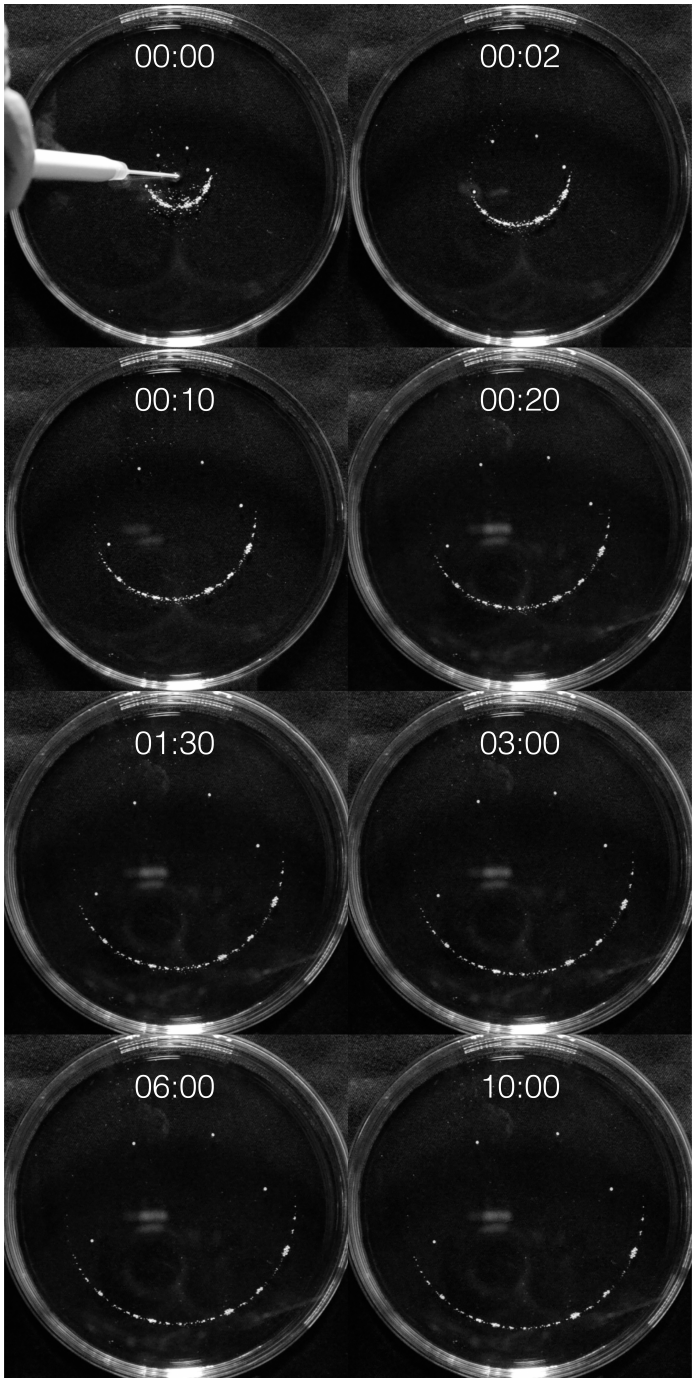

Figure A.1: Stills taken from spreading experiments with polystyrene particles and talc powder on the same 75% glycerine in water subphase. Talc forms a ring on the lower half of the dish (the "smile") and polystyrene beads are placed on the upper half (the "eyes") A 2 μL drop of 5 mg/mL tyloxapol was placed at 0 seconds. Times are marked as minutes:seconds on the images. The dish measures 7 cm in radius.

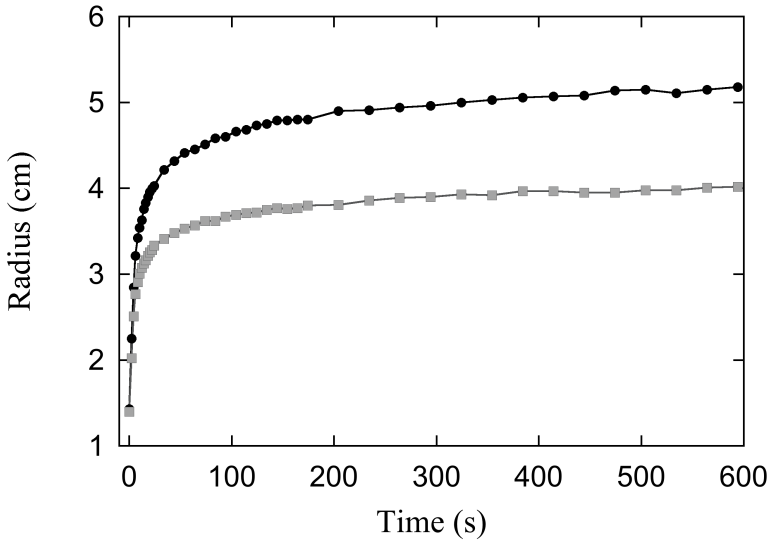

Figure A.2: Radius versus time for spreading experiments with polystyrene particles (gray squares) and talc powder (black circles) on the same 75% glycerine in water subphase. A 2 μL drop of 5 mg/mL tyloxapol was placed at 0 seconds. The dish measures 7 cm in radius. This data is from the experiment shown in Figure A.1.

A.2 Subsurface transport on PA solution

In Section 2.6.2, we used microscopy to show that aerosolizing phospholipid dispersions onto a water subphase results not only in a phospholipid monolayer at the interface, but also clusters of non-surface-active lipid vesicles just beneath the surface. This subsurface material is transported by subsurface flows induced by the Marangoni transport along the air-liquid interface. On water, the lipid clusters are seen to decrease in density with increasing depth. This transition is smooth over 200 μ or more depending on how long the experiment has been running.

A noticeably different result is seen in preliminary experiments on a PA solution subphase (these experiments had the same procedures as those on water). In this case, when aerosolized lipid is delivered, the lipid clusters are, again, visible beneath the interface, but they are more tightly constrained and there is a fairly discrete jump in density between the surface layer of clusters to the plain PA solution beneath.

The 1% 5 MDa PA solution used in this experiment innately contains small particulates that have not be characterized. These particulates are seen homogeneously throughout the PA solution before any aerosol is deposited (see Figure A.3A). As lipid aerosol is deposited, smaller, distinctly different lipid clusters can be seen moving across the field of view of the microscope. When we pan through the depth of the subphase, it is clear that the smaller lipid clusters are confined to the first $\sim$ 100 μm beneath the air-liquid interface (see Figure A.3B). Below this depth, there is a discrete transition to clean PA subphase, containing only the larger PA particulates (see Figure A.3C). This discrete layer was observed for the duration of surface transport and for $\sim$ 20 minutes following.

This work could mean a very interesting connection between Chapters 1 and 2 of this thesis. The aqueous phospholipid dispersion being delivered to the PA subphase may maintain a distinct miscible interface during surface transport. If this is the case, it has broad

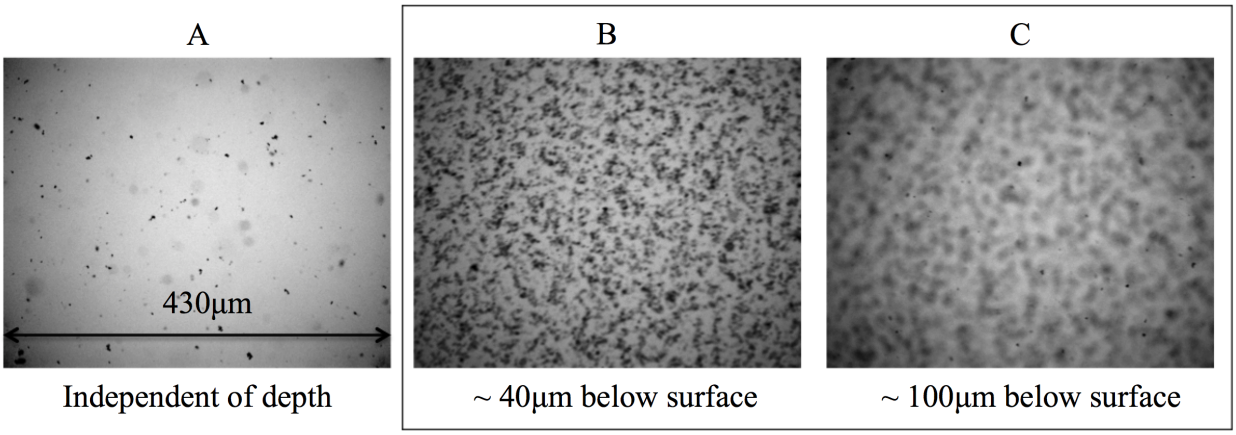

Figure A.3: Stills from subsurface transport microscopy images of 10 mg/mL DMPC dispersion aerosolized via vibrating mesh nebulizer onto a 1% 5 MDa PA solution subphase. A shows pure PA, which contains small particulates. This particulate matter is homogeneous and independent of depth. B and C show PA during deposition of aerosolized DMPC dispersion. B is focused $\sim$ 40 μm below the air-liquid interface, which is in the middle of the layer containing lipid clusters. C is focused $\sim$ 100 μm beneath the air-liquid interface, which is just beneath the layer containing lipid clusters. Lipid clusters can be seen out of focus, while PA particulates are in focus and approximately the same density as in the pure PA.

implications for Marangoni transport and drug delivery in the lung. It suggests that we could create a layer on which to spread if spreading conditions were not ideal. It also suggests that we could heal a de-wetted interface by adding a new surface liquid layer.

Appendix B

Further drop shape examples

B.1 Time series of drop shape evolution

Figures B.1 and B.2 show a more complete series of stills from our side-view videos. Figure B.1 shows a drop of water placed on 1.0% 5 MDa PA and Figure B.2 shows a drop of water placed on 0.4% 5 MDa PA. These are not the same trials used in analysis within the thesis. Note that the drop on the higher concentration subphase lasts longer and looks more crisp than on the more dilute subphase.

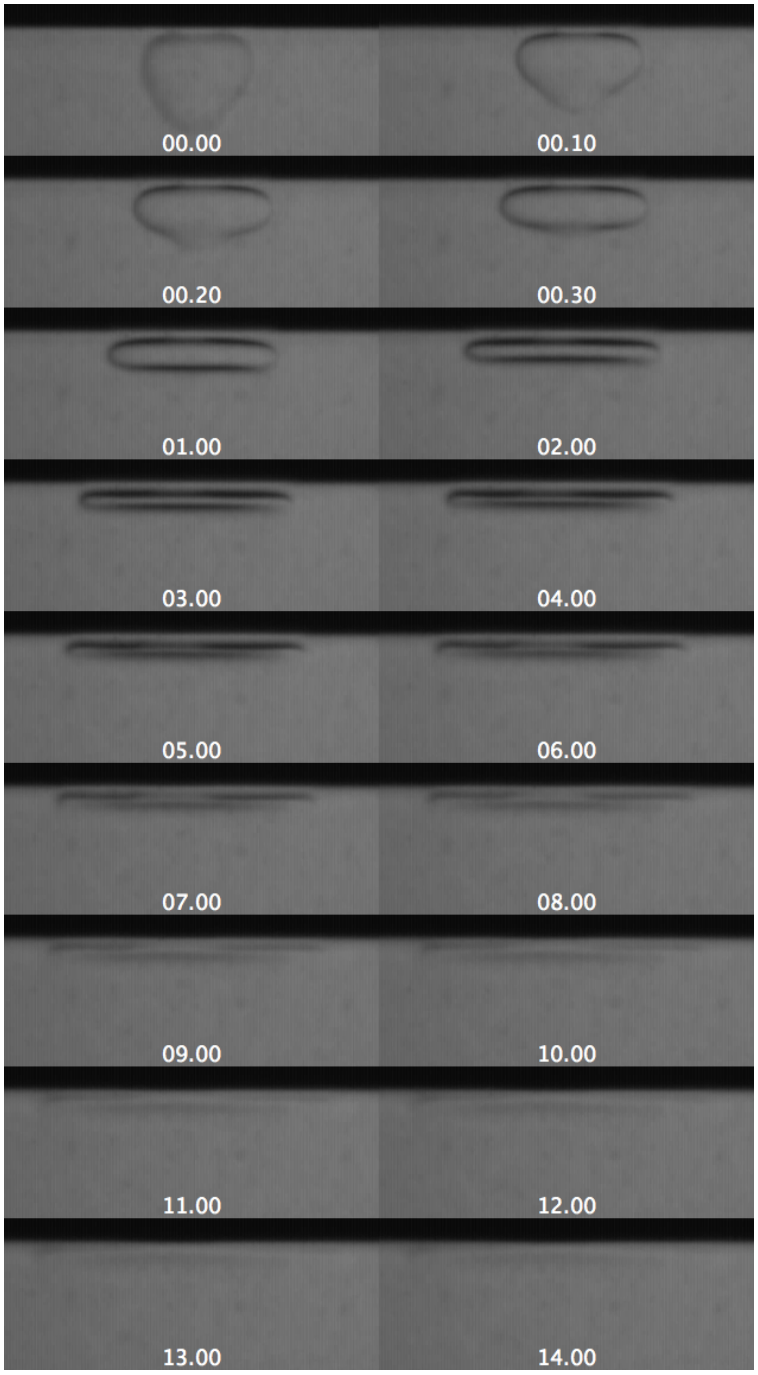

Figure B.1: Stills from side-view trials of a 2 μL drop of water placed on 1.0% 5 MDa PA. Times are shown on each image in the format minute:second. Each frame is 1.8 mm tall by 4.5 mm wide.

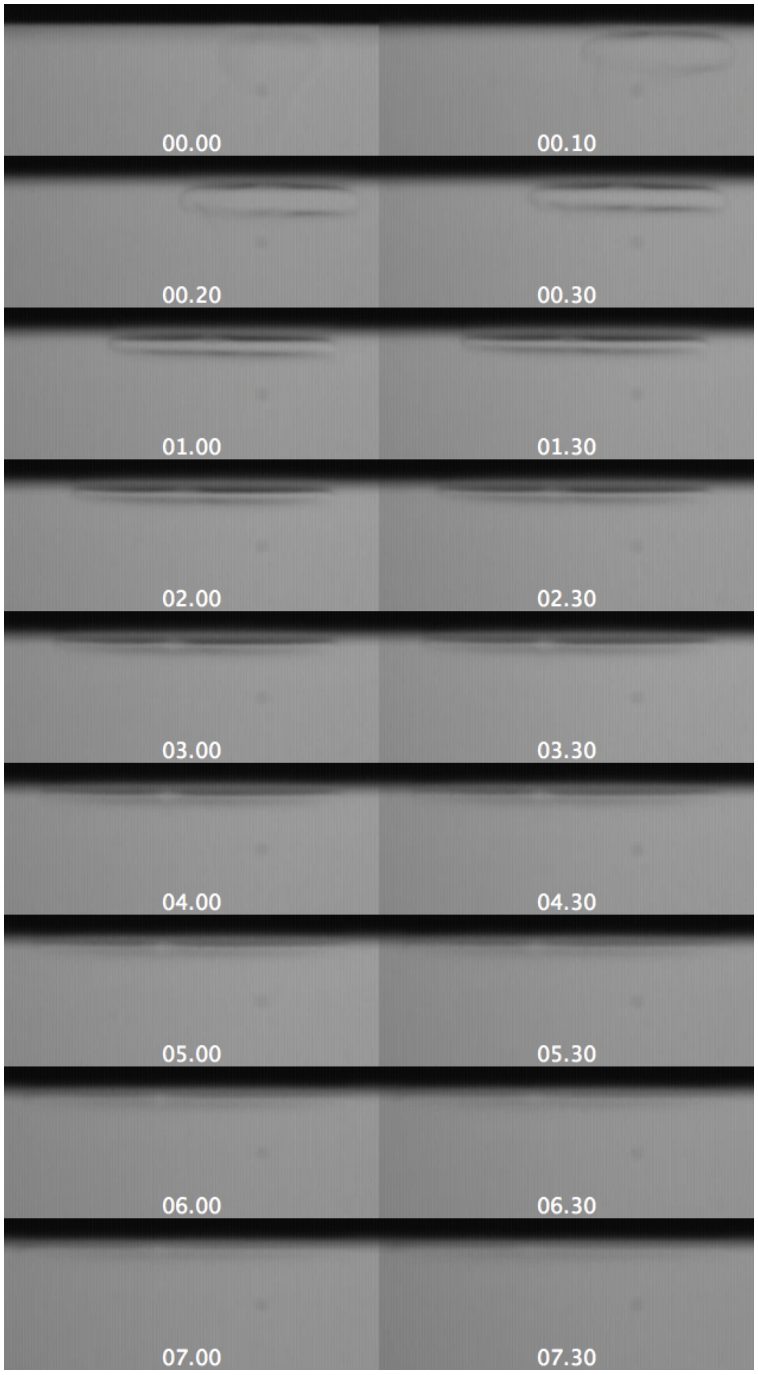

Figure B.2: Stills from side-view trials of a 2 μL drop of water placed on 0.4% 5 MDa PA. Times are shown on each image in the format minute:second. Each frame is 1.8 mm tall by 4.5 mm wide.

Appendix C

Mathematical and Computational Methods

C.1 Calculating the Sum of the Principal Curvatures of a Drop

The following curvature analysis for a rotationally symmetric shape has been performed many times in the literature (see, for example, [8, 68]). We repeat it here for completeness.

Our drop side-view images are two-dimensional cross sections of a three dimensional object. The full drop surface can be reconstructed by rotating the profile around its vertical axis. Here, we use the general (not necessarily normalized) t as the arc length variable to explicitly distinguish it from our normalized s.

$$\{x(t), 0, z(t)\} \quad \longmapsto \quad \{x(t)\cos\theta, x(t)\sin\theta, z(t)\}$$

The first step to calculating the mean curvature is to get the first fundamental form, also called the metric, of the surface. This object indicates how the inner product should be taken and allows measurements of lengths on non-flat surfaces. Here $\vec{\mathbf{e}}_i$ is used to denote the derivative of a position vector.

$$g_{ij} = \vec{\mathbf{e}}_i \cdot \vec{\mathbf{e}}_j \qquad \vec{\mathbf{e}}_i = \vec{r}_{,i} = \frac{\partial \vec{r}}{\partial u^i}$$

The metric of this surface of revolution, being a rank two tensor, can be expressed in matrix form as:

$$g = \begin{pmatrix} (x')^2 + (z')^2 & 0 \\ 0 & x^2 \end{pmatrix}$$

The second fundamental form, also called the shape operator, is another characteristic of the surface which depends on derivatives of the position vector on that surface. In this case, the second derivatives relate to the curvature of the surface. The mean curvature is

proportional to the trace of the shape operator and the Gaussian curvature is the determinant. To calculate the shape operator, the surface normal is dotted with various derivatives of the surface position. The surface normal is calculated through the cross product of the first derivatives, which lie tangent to the surface.

$$b_{ij} = \vec{r}_{,ij} \cdot \hat{n} = \vec{\mathbf{e}}_{i,j} \cdot \hat{n} \qquad \hat{n} = \frac{\vec{\mathbf{e}}_i \times \vec{\mathbf{e}}_j}{|\vec{\mathbf{e}}_i \times \vec{\mathbf{e}}_j|} \quad = \quad \frac{\{-z' \cos\theta, -z' \sin\theta, x'\}}{\sqrt{(x')^2 + (z')^2}}$$

$$b = \frac{1}{\sqrt{(x')^2 + (z')^2}} \begin{pmatrix} x'\,z'' - z'\,x'' & 0 \\ 0 & x\,z' \end{pmatrix}$$

The sum of the principal curvatures is two times the mean curvature, which is calculated by taking the trace of the second fundamental form. This requires summation of upper and lower indices (differential geometry/Einstein summing convention) and, thus, a raising operation using the inverse of the metric (first fundamental form). Taking the inverse of the metric is done in the usual matrix inversion way.

$$\kappa_1 + \kappa_2 = 2H = b^i_i = b_{ij} g^{ij} \quad \xrightarrow{\text{Matrix Notation}} \quad \text{Tr}\left(b \cdot g^{-1}\right)$$

$$b \cdot g^{-1} = \frac{1}{\sqrt{(x')^2 + (z')^2}} \begin{pmatrix} x'\,z'' - z'\,x'' & 0 \\ 0 & x\,z' \end{pmatrix} \begin{pmatrix} \frac{1}{(x')^2+(z')^2} & 0 \\ 0 & \frac{1}{x^2} \end{pmatrix}$$

$$= \frac{1}{x\Big((x')^2 + (z')^2\Big)^{3/2}} \begin{pmatrix} x(x'\,z'' - z'\,x'') & 0 \\ 0 & z'\Big((x')^2 + (z')^2\Big) \end{pmatrix}$$

$$2H = \frac{x(x'\,z'' - z'\,x'') + z'\Big((x')^2 + (z')^2\Big)}{x\Big((x')^2 + (z')^2\Big)^{3/2}}$$

We have discrete Fourier series for $x(t)$ and $z(t)$. Because these simply consist of sines and cosines, it is a simple process to find $x'(t)$, $x''(t)$, $z'(t)$ and $z''(t)$. These derivatives are then entered into the above equation to find the curvature.

C.2 Necessity of additional pressure for closing of drops

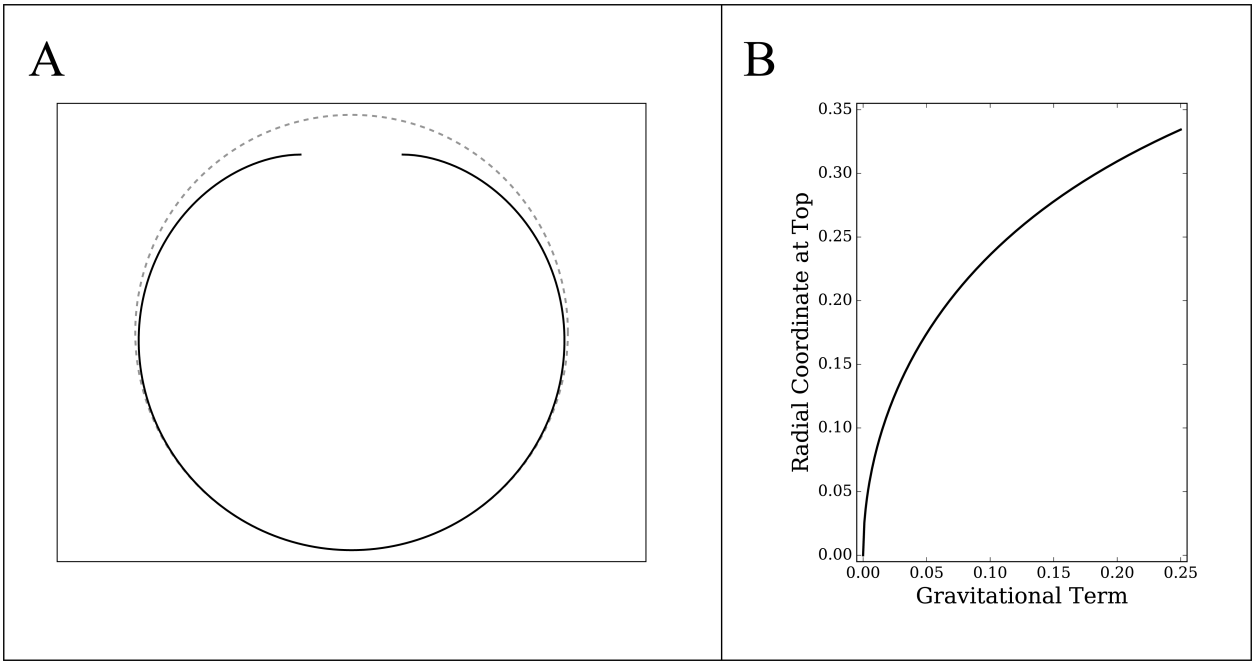

Figure C.1: A) In dashed gray, we show the spherical drop shape in the absence of external pressures. In black, we show a numerically solved drop shape with only buoyancy pressure, $R_0^2/a^2 = 0.1$. B) The value of the radial coordinate of the solution at the top of the drop, $\psi = \pi$, is plotted as a function of the Bond number, R_0^2/a^2. Only at zero gravity does the drop close at the top where the tangent to the curve becomes horizontal.

In our analysis of capillary drop shapes, we discuss that if there exists a buoyancy pressure on the drop, there is the need for an additional pressure ($P(z)$) to the AYLE in order for the drop to be closed and continuously smooth. Conceptually, this may be explained by the fact that the drop is static and there must, therefore, be a force cancelling the force of gravity.

$P(z)$ is, however, also required mathematically. If we were to ignore the $P(z)$ term in the Young-Laplace equation, it would be clear that the curvature must increase as a function of z because the buoyancy term is linear in z:

$$\gamma\kappa = P_L + \Delta\rho g z + \cancel{P(z)}$$

This means that the curvature would be lowest at the bottom of the drop (negative z) and then increase around the sides of the drop (to positive z). At some point, the solution of the Young-Laplace Equation would curl in on itself in a manner similar to the Euler elastica solutions characteristic of menisci in a trough. In Figure C.1A, we present a numeric analysis (conducted by Bradley Treece) demonstrating that solutions to the Augmented Young-Laplace equation without this added $P(z)$ do not close at the top. Rather, the two sides of the solution have tangents parallel to the interface at x positions away from the central axis of the drop. If these solutions were numerically progressed beyond this parallel tangent condition, they would continue to curl in on the drop, reversing along the x direction and not closing the drop shape. This would be, clearly, a non-physical solution. In reality, a contact line or an additional pressure must be present to close the shape. The only closed shape that this equation can produce is a circle, which occurs when there is no gravitational component (see the dashed line in Figure C.1A). Drops resting on interfaces can have closed shapes due to the surface with which they are in contact. The drop then has a flat region where it is connected to the surface and has a discontinuity in its smoothness at the contact line. The same is not possible for a drop suspended in a medium.

Figure C.1B shows the extent to which the drop does not close, that is, the extent of the gap at the top of the drop. These results are from the same numerical analysis as Figure C.1A. As the buoyancy pressure increases, or the Bond number increases, the gap at the top of the drop grows monotonically. In our case of extremely large Bond number drops,

there would be a considerable gap and, thus, there is the need for a considerable additional pressure.

C.3 Role of the z^3 term in drop shape

In our numerical solutions to the AYLE, we choose to neglect the third order terms in our curvature function. This choice is motivated by the observed symmetry of our drops. Across all of our observed drops, small asymmetries observed are also inconsistent in their sign, some bulging upward and some downward. As shown in Figure C.2, the addition of a cubic term introduces an asymmetry directionally dependent on the sign of this term. Since $P(z)$ is very unlikely to vary from one image to the next in a time sequence, the cubic term should have a consistent sign and, thus, we should see consistent deformation upward or downward. As discussed in Sections 3.5.3 and 3.6, the upward and downward bowing of the drop outlines is random and clearly due to noise in our image tracing. Therefore, we should assume that our experimental technique does not have the resolution to detect a third order term above the level of noise.

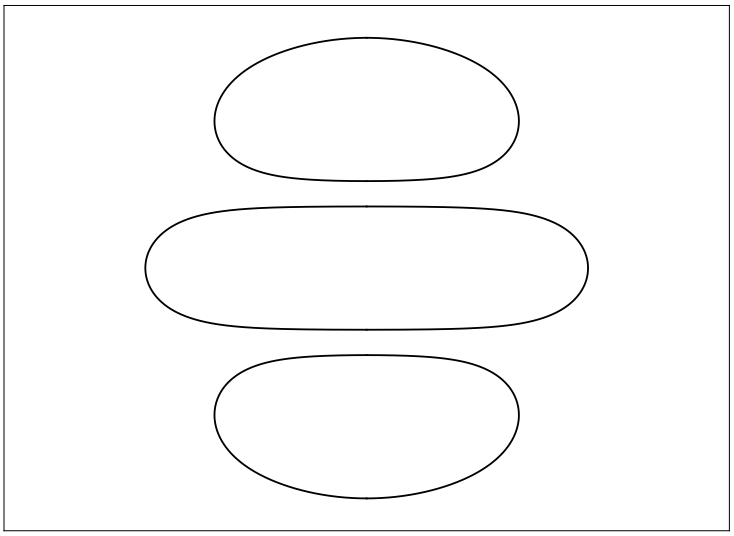

Figure C.2: Drop shapes are shown for a curvature profile that is quadratic in z (center) and for curvature profiles containing the same quadratic term plus additional cubic terms (top and bottom). The solution bulges upward with the addition of positive cubic terms (top) and downward with the addition of negative cubic terms (bottom).

References

[1] Abia B Afsar-Siddiqui, Paul F Luckham, and Omar K Matar. The spreading of surfactant solutions on thin liquid films. *Advances in Colloid and Interface Science*, 106(1-3):183–236, December 2003.

[2] G M Albers, R P Tomkiewicz, M K May, O E Ramirez, and B K Rubin. Ring distraction technique for measuring surface tension of sputum: Relationship to sputum clearability. *Journal of Applied Physiology*, 81(6):2690–2695, December 1996.

[3] O Albrecht, H Gruler, and E Sackmann. Polymorphism of phospholipid monolayers. *Journal de Physique*, 39(3):301–313, March 1978.

[4] D M Anderson and G B McFadden. Diffuse-interface methods in fluid mechanics. *Annual review of fluid Mechanics*, 30(1):139–165, 1998.

[5] Antonio Anzueto, Robert P Baughman, Kalpalatha K Guntupalli, John G Weg, Herbert P Wiedemann, Antoni Artigas Raventós, François Lemaire, Walker Long, David S Zaccardelli, and Edward N Pattishall. Aerosolized Surfactant in Adults with Sepsis-Induced Acute Respiratory Distress Syndrome. *dx.doi.org*, 334(22):1417–1422, August 2009.

[6] R Bansil, H E Stanley, and J T Lamont. Mucin Biophysics. *Annual Review of Physiology*, 57(1):635–657, 1995.

[7] Rama Bansil and Bradley S Turner. Mucin structure, aggregation, physiological functions and biomedical applications. *Current Opinion in Colloid & Interface Science*, 11(2-3):164–170, June 2006.

[8] John C Berg. *An Introduction to Interfaces & Colloids*. The Bridge to Nanoscience. World Scientific, 2010.

[9] Chris D Bertram and Donald P Gaver. Biofluid Mechanics of the Pulmonary System. *Annals of Biomedical Engineering*, 33(12):1681–1688, December 2005.

[10] Markus Bier. Nonequilibrium interfacial tension during relaxation. *Physical Review E*, 92(4):042128, October 2015.

[11] E S Brown, R P Johnson, and J A Clements. Pulmonary Surface Tension. *Journal of Applied Physiology*, 14(5):717–720, 1959.

[12] J S Brown, K L Zeman, and W D Bennett. Regional deposition of coarse particles and ventilation distribution in healthy subjects and patients with cystic fibrosis. *Journal of Aerosol Medicine*, 14(4):443–454, 2001.

[13] R A Brown and L E Scriven. The Shape and Stability of Rotating Liquid Drops. *Proceedings of the Royal Society of London A: Mathematical, Physical and Engineering Sciences*, 371(1746):331–357, June 1980.

[14] Jeffrey T Buboltz and Gerald W Feigenson. Phospholipid Solubility Determined by Equilibrium Distribution between Surface and Bulk Phases. *Langmuir*, 21(14):6296–6301, July 2005.

[15] J C Burton, F M Huisman, P Alison, D Rogerson, and P Taborek. Experimental and Numerical Investigation of the Equilibrium Geometry of Liquid Lenses. *Langmuir*, 26(19):15316–15324, October 2010.

[16] M Caffrey and J Hogan. LIPIDAT: a database of lipid phase transition temperatures and enthalpy changes. DMPC data subset analysis. *Chemistry and physics of lipids*, 61(1):1–109, March 1992.

[17] John W Cahn and John E Hilliard. Free Energy of a Nonuniform System. I. Interfacial Free Energy. *The Journal of Chemical Physics*, 28(2):258–267, February 1958.

[18] Derek Y C Chan, Evert Klaseboer, and Rogerio Manica. Film drainage and coalescence between deformable drops and bubbles. *Soft Matter*, 7(6):2235–2264, 2011.

[19] J R Charron and R D Tilton. A Scanning Angle Reflectometry Investigation of Block Copolymer Adsorption to Insoluble Lipid Monolayers at the Air Water Interface. *The Journal of Physical Chemistry*, 100(8):3179–3189, 1996.

[20] P Cicuta, A Vailati, and M Giglio. Capillary-to-Bulk Crossover of Nonequilibrium Fluctuations in the Free Diffusion of a Near-Critical Binary Liquid Mixture. *Applied optics*, 40(24):4140–4145, August 2001.

[21] John A Clements, Elwyn S Brown, and Rudolph P Johnson. Pulmonary Surface Tension and the Mucus Lining of the Lungs: Some Theoretical Considerations. *Journal of Applied Physiology*, 12(2):262–268, March 1958.

[22] Timothy E Corcoran, Kristina M Thomas, Stephen Garoff, Robert D Tilton, Todd M Przybycien, and Joseph M Pilewski. Imaging the Postdeposition Dispersion of an Inhaled Surfactant Aerosol. *Journal of Aerosol Medicine and Pulmonary Drug Delivery*, 25(5):290–296, October 2012.

[23] P G De Gennes. Wetting: statics and dynamics. *Reviews of modern physics*, 1985.

[24] Junqi Ding, Dawn Y Takamoto, Anja von Nahmen, Michael M Lipp, Ka Yee C Lee, Alan J Waring, and Joseph A Zasadzinski. Effects of Lung Surfactant Proteins, SP-B

and SP-C, and Palmitic Acid on Monolayer Stability. *Biophysical Journal*, 80(5):2262–2272, May 2001.

[25] Susan L Duncan and Ronald G Larson. Comparing Experimental and Simulated Pressure-Area Isotherms for DPPC. *Biophysical Journal*, 94(8):2965–2986, April 2008.

[26] D A Edwards, H Brenner, and D T Wasan. *Interfacial transport processes and rheology*. Bufferworth-Heinemann, 1991.

[27] F F Espinosa and A H Shapiro. Spreading of exogenous surfactant in an airway. *Journal of Applied Physiology*, 1993.

[28] Dotchi Exerowa and Dimo Platikanov. Thin liquid films from aqueous solutions of non-ionic polymeric surfactants. *Advances in Colloid and Interface Science*, 147-148(C):74–87, March 2009.

[29] Stanley B Fiel. Aerosolized antibiotics in cystic fibrosis: an update. *Expert Review of Respiratory Medicine*, 8(3):000–000, 2014.

[30] F Gaboriaud, R Golan, R Volinsky, A Berman, and R Jelinek. Organization and Structural Properties of Langmuir Films Composed of Conjugated Polydiacetylene and Phospholipids. *Langmuir*, 17(12):3651–3657, June 2001.

[31] F Gaboriaud, R Volinsky, A Berman, and R Jelinek. Temperature dependence of the organization and molecular interactions within phospholipid/diacetylene Langmuir films. *Journal of Colloid and Interface Science*, 287(1):191–197, July 2005.

[32] P Garik, J Hetrick, B Orr, D Barkey, and E Ben-Jacob. Interfacial cellular mixing and a conjecture on global deposit morphology. *Physical Review Letters*, 66(12):1606–1609, March 1991.

[33] D P Gaver and J B Grotberg. The dynamics of a localized surfactant on a thin film. *Journal of Fluid Mechanics*, 1990.

[34] D P Gaver and J B Grotberg. Droplet Spreading on a Thin Viscous Film. *Journal of Fluid Mechanics*, 235(1):399–414, February 1992.

[35] B E Gilbert, H R Six, S Z Wilson, P R Wyde, and V Knight. Small particle aerosols of enviroxime-containing liposomes. *Antiviral research*, 9(6):355–365, September 1988.

[36] Ajaykumar Gopal and Ka Yee C Lee. Morphology and Collapse Transitions in Binary Phospholipid Monolayers. *The Journal of Physical Chemistry B*, 105(42):10348–10354, October 2001.

[37] Ajaykumar Gopal and Ka Yee C Lee. Headgroup Percolation and Collapse of Condensed Langmuir Monolayers †. *The Journal of Physical Chemistry B*, 110(44):22079–22087, November 2006.

[38] F L Grohmann, F Csempesz, and M Szogyi. Stabilization of small unilamellar DMPC-liposomes by uncharged polymers. *Colloid and Polymer Science*, 276(1):66–71, January 1998.

[39] J B Grotberg. Respiratory fluid mechanics and transport processes. *Annual Review of Biomedical Engineering*, 3(1):421–457, 2001.

[40] J B Grotberg and D P Gaver. A synopsis of surfactant spreading research. *Journal of Colloid and Interface Science*, 178(1):377–378, 1996.

[41] J B Grotberg, D Halpern, and O E Jensen. Interaction of Exogenous and Endogenous Surfactant: Spreading-Rate Effects. *Journal of Applied Physiology*, 78(2):750–756, February 1995.

[42] S M Gruner, R P Lenk, A S Janoff, and M J Ostro. Novel Multilayered Lipid Vesicles - Comparison of Physical Characteristics of Multilamellar Liposomes and Stable Plurilamellar Vesicles. *Biochemistry*, 24(12):2833–2842, 1985.

[43] M Gudmand, Matthias Fidorra, T Bjoslashrnholm, and T Heimburg. Diffusion and Partitioning of Fluorescent Lipid Probes in Phospholipid Monolayers. *Biophysical Journal*, 96(11):4598–4609, June 2009.

[44] D Halpern, O E Jensen, and J B Grotberg. A theoretical study of surfactant and liquid delivery into the lung. *Journal of Applied Physiology*, 85(1):333–352, July 1998.

[45] Christine L Hattrup and Sandra J Gendler. Structure and Function of the Cell Surface (Tethered) Mucins. *Annual Review of Physiology*, 70(1):431–457, March 2008.

[46] W Helfrich. Blocked lipid exchange in bilayers and its possible influence on the shape of vesicles. *Zeitschrift fur Naturforschung. Section C, Biosciences*, 29C(9-10):510–515, 1974.

[47] D R Henderson, S B Friedman, J D Harris, W B Manning, and M A Zoccoli. CEDIA, a New Homogeneous Immunoassay System. *Clinical Chemistry*, 32(9):1637–1641, September 1986.

[48] Henri Gouin. Liquid nanofilms. A mechanical model for the disjoining pressure. *International Journal of Engineering Science*, 47(5-6):691–699, June 2009.

[49] B A Hills. Alveolar Liquid Lining - Langmuir Method Used to Measure Surface -Tension in Bovine and Canine Lung Extracts. *Journal of Physiology-London*, 359(FEB):65–79, 1985.

[50] S R Hodges, O E Jensen, and J M Rallison. Sliding, slipping and rolling: the sedimentation of a viscous drop down a gently inclined plane. *Journal of Fluid Mechanics*, 512:1–37, July 2004.

[51] V I Hof, P Gehr, V Gerber, M M Lee, and S Schürch. In vivo determination of surface tension in the horse trachea and in vitro model studies. *Respiration Physiology*, 109(1):81–93, July 1997.

[52] Shilin Huang, Kornelia Gawlitza, Regine von Klitzing, Laurent Gilson, Johannes Nowak, Stefan Odenbach, Werner Steffen, and Günter K Auernhammer. Microgels at the Water/Oil Interface: In Situ Observation of Structural Aging and Two - Dimensional Magnetic Bead Microrheology. *Langmuir*, 32(3):712–722, January 2016.

[53] D D Joseph. Fluid dynamics of two miscible liquids with diffusion and gradient stresses. *European Journal of Mechanics B Fluids*, 1990.

[54] D D Joseph, A Huang, and H Hu. Non-solenoidal velocity effects and Korteweg stresses in simple mixtures of incompressible liquids. *Physica D*, 97(1-3):104–125, 1996.

[55] Daniel D Joseph and Howard H Hu. Interfacial tension between miscible liquids. Technical report, University of Minnesota, July 1991.

[56] George Karapetsas, Richard V Craster, and Omar K Matar. Surfactant driven dynamics of liquid lenses. *Physics of Fluids*, 23(12):122106, 2011.

[57] R F Kayser, M R Moldover, and J W Schmidt. What controls the thicknesses of wetting layers? *Journal of the Chemical Society, Faraday Transactions 2*, 82(10):1701–19, 1986.

[58] Amsul Khanal, Ramankur Sharma, Timothy E Corcoran, Stephen Garoff, Todd M Przybycien, and Robert D Tilton. Surfactant Driven Post-Deposition Spreading of

Aerosols on Complex Aqueous Subphases. 1: High Deposition Flux Representative of Aerosol Delivery to Large Airways. *Journal of Aerosol Medicine and Pulmonary Drug Delivery*, 28(5):382–393, October 2015.

[59] Junseok Kim. A continuous surface tension force formulation for diffuse-interface models. *Journal of Computational Physics*, 204(2):784–804, April 2005.

[60] Sook Heun Kim and Elias I Franses. New protocols for preparing dipalmitoylphosphatidylcholine dispersions and controlling surface tension and competitive adsorption with albumin at the air/aqueous interface. *Colloids and Surfaces B: Biointerfaces*, 43(3-4):256–266, July 2005.

[61] Sook Heun Kim, Lilac Haimovich-Caspi, Liora Omer, Yeshayahu Talmon, and Elias I Franses. Effect of sonication and freezing-thawing on the aggregate size and dynamic surface tension of aqueous DPPC dispersions. *Journal of Colloid and Interface Science*, 311(1):217–227, July 2007.

[62] Sook Heun Kim, Yoonjee Park, Sadis Matalon, and Elias I Franses. Effect of buffer composition and preparation protocol on the dispersion stability and interfacial behavior of aqueous DPPC dispersions. *Colloids and Surfaces B: Biointerfaces*, 67(2):253–260, December 2008.

[63] Jason P Kirkness, Peter R Eastwood, Irene Szollosi, Peter R Platt, John R Wheatley, Terence C Amis, and David R Hillman. Effect of surface tension of mucosal lining liquid on upper airway mechanics in anesthetized humans. *Journal of Applied Physiology*, 95(1):357–363, July 2003.

[64] Felix Kleinschmidt, Cosima Stubenrauch, Je rome Delacotte, Regine von Klitzing, and Dominique Langevin. Stratification of Foam Films Containing Polyelectrolytes.

Influence of the Polymer Backbone's Rigidity. *The Journal of Physical Chemistry B*, 113(12):3972–3980, March 2009.

[65] Kevin Koch, Beautia Dew, Timothy E Corcoran, Todd M Przybycien, Robert D Tilton, and Stephen Garoff. Surface Tension Gradient Driven Spreading on Aqueous Mucin Solutions: A Possible Route to Enhanced Pulmonary Drug Delivery. *Molecular Pharmaceutics*, 8(2):387–394, April 2011.

[66] Masami Kojima, E J Hinch, and Andreas Acrivos. The formation and expansion of a toroidal drop moving in a viscous fluid. *Physics of Fluids*, 27(1):19–15, 1984.

[67] D J Korteweg. *Sur la forme que prennent les équations du mouvement des fluides si l'on tient compte des forces capillaires causées par des variations de densité ...*. Archives Néerlandaises des Sciences exactes et ..., 1901.

[68] E Kreyszig. Introduction to differential geometry and Riemannian geometry, 1968.

[69] I Kubo, S Adachi, H Maeda, and A Seki. Phosphatidylcholine monolayers observed with Brewster angle microscopy and π-A isotherms. *Thin Solid Films*, 393(1-2):80–85, 2001.

[70] M A Launois-Surpas, T Ivanova, and I Panaiotov. Behavior of pure and mixed DPPC liposomes spread or adsorbed at the air-water interface. *Colloid and Polymer Science*, 1992.

[71] K S Lee, N Ivanova, V M Starov, N Hilal, and V Dutschk. Kinetics of wetting and spreading by aqueous surfactant solutions. *Advances in Colloid and Interface Science*, 144(1-2):54–65, December 2008.

[72] K S Lee and V M Starov. Spreading of surfactant solutions over thin aqueous layers at low concentrations: Influence of solubility. *Journal of Colloid and Interface Science*, 329(2):361–365, January 2009.

[73] Ka Yee C Lee. Collapse mechanisms of Langmuir monolayers. *Annual review of physical chemistry*, 59:771–791, 2008.

[74] Michael M Lipp, Ka Yee C Lee, Joseph A Zasadzinski, and Alan J Waring. Design and performance of an integrated fluorescence, polarized fluorescence, and Brewster angle microscope/Langmuir trough assembly for the study of lung surfactant monolayers. *Review of Scientific Instruments*, 68(6):2574–10, 1997.

[75] J Lowengrub and L Truskinovsky. Quasi–incompressible Cahn–Hilliard fluids and topological transitions. *Proceedings of the Royal Society A: Mathematical, Physical and Engineering Sciences*, 1998.

[76] Rogerio Manica, Evert Klaseboer, and Derek Y C Chan. The impact and bounce of air bubbles at a flat fluid interface. *Soft Matter*, 12(13):3271–3282, April 2016.

[77] Amy L Marcinkowski, Stephen Garoff, Robert D Tilton, Joseph M Pilewski, and Timothy E Corcoran. Postdeposition Dispersion of Aerosol Medications Using Surfactant Carriers. *Journal of Aerosol Medicine and Pulmonary Drug Delivery*, 21(4):361–370, December 2008.

[78] O K Matar and R V Craster. Dynamics of surfactant assisted spreading. *Soft Matter*, 5(20):3801–3809, 2009.

[79] SE May and JV Maher. Capillary-wave relaxation for a meniscus between miscible liquids. *Physical Review Letters*, 67(15):2013–2016, October 1991.

[80] B A Miller-Chou and J L Koenig. A review of polymer dissolution. *Progress in Polymer Science*, 2003.

[81] Stefan Minocchieri, Stephan Knoch, W Michael Schoel, Matthias Ochs, and Mathias Nelle. Nebulizing poractant alfa versus conventional instillation: Ultrastructural appearance and preservation of surface activity. *Pediatric Pulmonology*, 49(4):348–356, April 2014.

[82] M R Moldover and J W Cahn. An interface phase transition: complete to partial wetting. *Science (New York, N.Y.)*, 207(4435):1073–1075, March 1980.

[83] J F Nagle and D A Wilkinson. Lecithin bilayers. Density measurement and molecular interactions. *Biophysical Journal*, 23(2):159–175, August 1978.

[84] Ramon Pericet-Camara, Günter K Auernhammer, Kaloian Koynov, Simone Lorenzoni, Roberto Raiteri, and Elmar Bonaccurso. Solid-supported thin elastomer films deformed by microdrops. *Soft Matter*, 5(19):3611–8, 2009.

[85] Luka Pocivavsek, Shelli L Frey, Kapilanjan Krishan, Kseniya Gavrilov, Piotr Ruchala, Alan J Waring, Frans J Walther, Michael Dennin, Thomas A Witten, and Ka Yee C Lee. Lateral stress relaxation and collapse in lipid monolayers. *Soft Matter*, 4(10):2019–11, 2008.

[86] John A Pojman, Colin Whitmore, Maria Liria Turco Liveri, Renato Lombardo, Jolanta Marszalek, Rosie Parker, and Brian Zoltowski. Evidence for the Existence of an Effective Interfacial Tension between Miscible Fluids: Isobutyric Acid-Water and 1-Butanol-Water in a Spinning-Drop Tensiometer. *Langmuir*, 22(6):2569–2577, March 2006.

[87] Francis R Poulain and John A Clements. Pulmonary Surfactant Therapy. *The Western Journal of Medicine*, pages 1–8, July 2014.

[88] P R Pujado and L E Scriven. Sessile lenticular configurations: translationally and rotationally symmetric lenses. *Journal of Colloid and Interface Science*, 40(1):82–98, 1972.

[89] E Reimhult, F Hook, and B Kasemo. Intact vesicle adsorption and supported biomembrane formation from vesicles in solution: Influence of surface chemistry, vesicle size, temperature, and osmotic pressure. *Langmuir*, 19(5):1681–1691, 2003.

[90] M I Restrepo, H Keyt, and L F Reyes. Aerosolized Antibiotics. *Respiratory Care*, 60(6):762–773, June 2015.

[91] D Ross, D Bonn, and J Meunier. Observation of short-range critical wetting. *Nature*, 400(6746):737–739, 1999.

[92] Y Rotenberg, L Boruvka, and A W Neumann. Determination of surface tension and contact angle from the shapes of axisymmetric fluid interfaces. *Journal of Colloid and Interface Science*, 93(1):169–183, 1983.

[93] Sameh M I Saad, Zdenka Policova, Edgar J Acosta, and A Wilhelm Neumann. Effect of surfactant concentration, compression ratio and compression rate on the surface activity and dynamic properties of a lung surfactant. *BBA - Biomembranes*, 1818(1):103–116, January 2012.

[94] J M Samet and P W Cheng. The Role ofAirway Mucus in Pulmonary Toxicology. *Environmental Health Perspectives*, 102(Suppl 2):89–103, June 1994.

[95] S Schürch, J Goerke, and J A Clements. Direct determination of surface tension in the lung. *Proceedings of the National Academy of Sciences of the United States of America*, 73(12):4698–4702, December 1976.

[96] S Schürch, J Goerke, and J A Clements. Direct determination of volume- and time-dependence of alveolar surface tension in excised lungs. *Proceedings of the National Academy of Sciences of the United States of America*, 75(7):3417–3421, July 1978.

[97] Ramankur Sharma, Timothy E Corcoran, Stephen Garoff, Todd M Przybycien, Ellen R Swanson, and Robert D Tilton. Quasi-Immiscible Spreading of Aqueous Surfactant Solutions on Entangled Aqueous Polymer Solution Subphases. *ACS Applied Materials & Interfaces*, 5(12):5542–5549, June 2013.

[98] Ramankur Sharma, Timothy E Corcoran, Stephen Garoff, Todd M Przybycien, and Robert D Tilton. Transport of a partially wetted particle at the liquid/vapor interface under the influence of an externally imposed surfactant generated Marangoni stress. *Colloids and Surfaces A: Physicochemical and Engineering Aspects*, 521:49–60, May 2017.

[99] Ramankur Sharma, Roomi Kalita, Ellen R Swanson, Timothy E Corcoran, Stephen Garoff, Todd M Przybycien, and Robert D Tilton. Autophobing on Liquid Subphases Driven by the Interfacial Transport of Amphiphilic Molecules. *Langmuir*, 28(43):15212–15221, October 2012.

[100] Ramankur Sharma, Amsul Khanal, Timothy E Corcoran, Stephen Garoff, Todd M Przybycien, and Robert D Tilton. Surfactant Driven Post-Deposition Spreading of Aerosols on Complex Aqueous Subphases. 2: Low Deposition Flux Representative of Aerosol Delivery to Small Airways. *Journal of Aerosol Medicine and Pulmonary Drug Delivery*, 28(5):394–405, October 2015.

[101] R M Shawar, D L MacLeod, R L Garber, J L Burns, J R Stapp, C R Clausen, and S K Tanaka. Activities of tobramycin and six other antibiotics against Pseudomonas aeruginosa isolates from patients with cystic fibrosis. *Antimicrobial Agents and Chemotherapy*, 43(12):2877–2880, December 1999.

[102] P G Smith and TGM Van De Ven. The transient interfacial tension between two miscible fluids. *Journal of Colloid and Interface Science*, 1981.

[103] G D Stetten and R Drezek. Active fourier contour applied to real time 3d ultrasound of the heart. *International Journal of Image and Graphics*, 01(04):647–658, 2001.

[104] M S P Stevar and A Vorobev. Shapes and dynamics of miscible liquid/liquid interfaces in horizontal capillary tubes. *Journal of Colloid and Interface Science*, 383(1):184–197, October 2012.

[105] Mihaela S P Stevar and Anatoliy Vorobev. Dissolution Dynamics of Liquid/Liquid Binary Mixtures Within a Micromodel. *Transport in Porous Media*, 100(3):407–424, 2013.

[106] T Strateva, G Petrova, and I Mitov. Antimicrobial activity of tobramycin against respiratory cystic fibrosis Pseudomonas aeruginosa isolates from Bulgaria. *Journal of chemotherapy (Florence, Italy)*, 22(6):378–383, December 2010.

[107] K Svartengren, P-Å Lindestad, M Svartengren, G Bylin, K Philipson, and P Camner. Deposition of inhaled particles in the mouth and throat of asthmatic subjects. *European Respiratory Journal*, 7(8):1467–1473, August 1994.

[108] K M G Taylor, G Taylor, I W Kellaway, and J Stevens. The stability of liposomes to nebulisation. *International Journal of Pharmaceutics*, 58(1):57–61, 1990.

[109] S Torza and S G Mason. Three-phase interactions in shear and electrical fields. *Journal of Colloid and Interface Science*, 33(1):67–83, 1970.

[110] B V Toshev. Thermodynamic theory of thin liquid films including line tension effects. *Current Opinion in Colloid & Interface Science*, 2008.

[111] S Tristram-Nagle, M C Wiener, C P Yang, and J F Nagle. Kinetics of the subtransition in dipalmitoylphosphatidylcholine. *Biochemistry*, 1987.

[112] Domenico Truzzolillo and Luca Cipelletti. Off-equilibrium surface tension in miscible fluids. *Soft Matter*, pages 1–9, June 2016.

[113] Domenico Truzzolillo, Serge Mora, Christelle Dupas, and Luca Cipelletti. Off-Equilibrium Surface Tension in Colloidal Suspensions. *Physical Review Letters*, 112(12):128303–5, March 2014.

[114] Domenico Truzzolillo, Serge Mora, Christelle Dupas, and Luca Cipelletti. Nonequilibrium Interfacial Tension in Simple and Complex Fluids. *Physical Review X*, 6(4):041057, December 2016.

[115] R Veldhuizen, K Nag, S Orgeig, and F Possmayer. The role of lipids in pulmonary surfactant. *Biochimica et Biophysica Acta*, 1408(2-3):90–108, 1998.

[116] E R Weibel and D M Gomez. Architecture of the human lung. Use of quantitative methods establishes fundamental relations between size and number of lung structures. *Science (New York, N.Y.)*, 137(3530):577–585, August 1962.

[117] X Wen and E I FRANSES. Role of subsurface particulates on the dynamic adsorption of dipalmitoylphosphatidylcholine at the air/water interface. *Langmuir*, 17(11):3194–3201, 2001.

[118] Qingfang Wu and Harris Wong. A slope-dependent disjoining pressure for non-zero contact angles. *Journal of Fluid Mechanics*, 506:157–185, 1999.

[119] Taeil Yi and Harris Wong. Theory of slope-dependent disjoining pressure with application to Lennard–Jones liquid films. *Journal of Colloid and Interface Science*, 313(2):579–591, September 2007.

[120] Brian Zoltowski, Yuri Chekanov, Jonathan Masere, John A Pojman, and Vitaly Volpert. Evidence for the Existence of an Effective Interfacial Tension between Miscible Fluids. 2. Dodecyl Acrylate-Poly(dodecyl acrylate) in a Spinning Drop Tensiometer. *Langmuir*, 23(10):5522–5531, May 2007.